Porous hydrogel nanocomposites with embedded bacteria for biotechnological applications

Vom Fachbereich Produktionstechnik

der

UNIVERSITÄT BREMEN

zur Erlangung des Grades

Doktor-Ingenieur

genehmigte

Dissertation

von

Jéssica Condi Mainardi

Gutachter:

Prof. Dr.-Ing. Kurosch Rezwan
Prof. Dr.-Ing. Lucio Colombi Ciacchi

Tag der mündlichen Prüfung: 26.09.2022

Acknowledgement

I would like to thank Prof. Dr.-Ing. Kurosch Rezwan for giving me the opportunity to do my PhD studies at the Advanced Ceramics institute under his guidance and thanks to my supervisors PD Dr. Michael Maas and Dr. Stephen Kroll for their invested time, scientific input and advice. I would also like to thank Prof. Dr.-Ing. Lucio Colombi Ciacchi for supporting me as the second examiner of this work.

A thank you to all my colleagues, technical staff (especially Tina), and students (especially Catarina) at the institute for the support, scientific advice, and hot chocolate time with fruitful conversations. I would like to especially thank Marieke, Renato, Bárbara, Natália, and Pedro for their moral support, patience, friendship and help during these years at the institute.

A thank you to my colleagues from MIMENIMA, especially Mojtaba and Karin for the enjoyable and successful collaboration.

A thank you to my friends in Brazil Ísis, Stephanie, Mariana, Natacha, and Laura for their friendship and for supporting me even with the distance.

Finally, special thanks to my parents Doralice and Roberto, my sister Juliana and my husband Maximilian that supported me in all my decisions. I love you all.

Thank you!

Jéssica

Contents

Abstract

Technological processes based on microorganisms such as bacteria offer great potential for an environmentally friendly as well as resource-efficient production and purification of, for example, pharmaceuticals and water. Immobilizing microorganism inside semi-permeable substrates such as hydrogels is a suitable strategy to simplify the process of separation and purification in bioreactors, reducing costs and processing time of biotechnological processes. To meet the mechanical requirements, nanoparticles can be integrated into the hydrogel matrix to form a nanocomposite. However, the integration of particles can be detrimental to cells due to toxicity. Furthermore, the processing of hydrogel nanocomposites can be harmful to the cell due to high shear forces in the feedstock. Moreover, nutrient accessibility might be influenced by the particles and can hinder nutrient diffusion into the material and cells. Beyond that, high material porosity and a range of pore sizes are necessary to ensure proper nutrient diffusion. Thus, the processing of hydrogels with suitable rigidity to maintain the porosity and biocompatibility is still a challenge.

This work aims to develop new processing strategies for microorganism immobilization into rigid porous materials for bioprocessing applications using only biocompatible materials. Microorganism behavior and accessibility in the different immobilization strategies as well as the influence of porosity on the overall biotransformation performance were investigated.

In the first part of this work, a straightforward one-pot processing route based on the reinforcement of an alginate hydrogel with alumina nanoparticles, followed by the addition of bacteria *Escherichia coli* or *Bacillus subtilis* and subsequent internal/external ionotropic gelation steps was established. The developed bionanocomposite showed minimal shrinkage, increased structural and mechanical stability, as well as excellent biocompatibility. The immobilized bacteria maintained high viability and similar metabolic activity as non-immobilized cells and were able to consume glucose after several cycles as well as after 60 days of storage. The method could be adapted to each specific cell, such as bacteria, yeast, fungus, or even animal cells, by adding the proper nutrients into the suspension and it can be used with various shaping strategies to produce macroscopic materials like casting, extruding or 3D printing. Yet, this method showed some nutrient transport limitations as well as low material stability in specific solutions such as phosphate-buffered saline (PBS), which resulted in material dissolution after some days.

To overcome restricted nutrient diffusion/permeability, a feedstock for 3D bioprinting structures with hierarchical porosity was developed. The feedstock is based on a modified

highly particle-filled alumina/alginate nanocomposite gel with immobilized *E. coli* bacteria and the protein ovalbumin acting as a foaming agent. The foamed nanocomposite was shaped into a porous mesh structure by 3D printing. The influence of albumin on rheological properties, total porosity, water diffusion coefficient, and bacterial viability was characterized by bulk and interfacial rheology, X-ray microtomography (μCT), nuclear magnetic resonance (NMR) tomography, and resazurin assay respectively. The addition of albumin was an effective method to stabilize foams even after the printing procedure, resulting in enhanced material porosity. Albumin addition also increased the printability of the feedstocks as well as induced bacterial growth. The experimental results demonstrated a higher water content when porosity increases and consequently higher effective cell viability.

The third part of the work aimed to increase material stability and avoid its dissolution in specific solutions. Therefore, a strategy for synthesizing a feedstock suitable for 3D bioprinting and covalent crosslinking of mechanically robust materials with embedded living bacteria was developed. The processing route is based on a highly particle-filled alumina/chitosan nanocomposite gel which is crosslinked by electrostatic interactions and covalent bonding using alginate and genipin, respectively. Feedstock's properties and crosslinking time were analyzed by means of bulk rheology while crosslinked material stability in different solutions was analyzed by incubating crosslinked material in different solutions for 60 days. The addition of alginate was essential for printability and effective bacterial viability since samples without alginate showed no bacterial viability. The covalently crosslinked material successfully did not dissolve in phosphate-buffered saline (PBS), hydrochloric acid (HCl), sodium hydroxide (NaOH), or water.

The experimental results obtained within this work demonstrate the potential of the described approaches for producing porous macroscopic bioactive materials with complex 3D geometries using only natural materials as a platform for novel applications in bioprocessing.

Zusammenfassung

Technologische Verfahren basierend auf Mikroorganismen, wie Bakterien, bieten großes Potenzial für eine ressourceneffiziente sowie umweltfreundliche Herstellung und Aufbereitung von z.B. Arzneimitteln und Wasser. Die Immobilisierung von Mikroorganismen in semipermeablen Substraten, wie Hydrogelen, ist eine geeignete Strategie, um den Prozess der Trennung und Aufbereitung in Bioreaktoren zu vereinfachen und Kosten sowie Verarbeitungszeit biotechnologischer Prozesse zu reduzieren. Um die mechanischen Anforderungen zu erfüllen, können Nanopartikel in die Hydrogel-Matrix integriert werden, um ein Nanokomposit zu bilden. Darüber hinaus kann die Verarbeitung von Hydrogel-Nanokompositen aufgrund der verstärkten Scherung des Ausgangsmaterials schädlich für die Zelle sein. Weiterhin kann die Nährstoffverfügbarkeit durch die Partikel beeinflusst werden und die Nährstoffdiffusion in das Material und die Zellen behindern. Eine hohe Materialporosität und unterschiedliche Porengrößen sind erforderlich, um eine ordnungsgemäße Nährstoffdiffusion zu gewährleisten. Aus diesen Gründen ist die Verarbeitung von Hydrogelen mit geeigneter Steifigkeit zur Aufrechterhaltung der Porosität und Biokompatibilität weiterhin eine Herausforderung.
Das Ziel dieser Arbeit ist die Entwicklung neuer Verarbeitungsstrategien für die Immobilisierung von Mikroorganismen in starren porösen Materialien für Bioprocessing, bei denen ausschließlich biokompatibel Materialien verwendet werden. Untersucht wurden hierbei das Verhalten und die Zugänglichkeit von Mikroorganismen in den verschiedenen Immobilisierungsstrategien sowie der Einfluss der Porosität auf die Gesamtleistung der Biotransformation.

Im ersten Teil dieser Arbeit wurde eine unkomplizierte Verarbeitungsroute basierend auf der Verstärkung eines Alginat-Hydrogels mit Aluminiumoxid-Nanopartikeln, gefolgt von der Zugabe von *Escherichia coli* oder *Bacillus subtilis* Bakterien sowie anschließenden internen/externen ionotropen Gelierungsschritten etabliert. Das entwickelte Bionano-komposit zeigte eine minimale Schrumpfung, eine stark erhöhte strukturelle und mechanische Stabilität sowie eine hervorragende Biokompatibilität. Die immobilisierten Bakterien zeigten eine hohe Lebensfähigkeit und eine ähnliche Stoffwechselaktivität wie nicht eingebettete Zellen und waren in der Lage, Glucose nach mehreren Zyklen sowie nach 60 Tagen Lagerung zu verstoffwechseln. Das Verfahren kann an andere Zellen, wie Bakterien, Hefen, Pilze oder sogar tierische Zellen angepasst werden, indem der Suspension die richtigen Nährstoffe hinzugefügt werden und es kann mit verschiedenen Formgebungsstrategien angewendet werden, wie Gießen, Extrudieren oder 3D-Druck, um makroskopische Materialien herzustellen. Diese Methode zeigte jedoch einige Einschränkungen beim Nährstofftransport sowie eine geringe Materialstabilität in

bestimmten Lösungen, wie Phosphatgepufferter Salzlösung (PBS), die nach einigen Tagen zu einer Materialauflösung führte.

Um einen eingeschränkten Nährstofftransport zu überwinden, wurde ein Ausgangsmaterial für 3D-Biodruck-Strukturen mit hierarchischer Porosität entwickelt. Das Ausgangsmaterial basiert auf einem modifizierten hochpartikelgefüllten Aluminiumoxid/Alginat Nanokomposit-Gel mit immobilisierten *E. coli* Bakterien, wobei das Protein Ovalbumin als Schaummittel fungiert. Das aufgeschäumte Nanokomposit wird durch 3D-Druck zu einer porösen Netzstruktur in Form gebracht. Der Einfluss von Albumin auf die rheologischen Eigenschaften, die Gesamtporosität, den Wasserdiffusionskoeffizienten und die bakterielle Lebensfähigkeit wurde durch Bulk/Grenzflächenrheologie, Röntgenmikrotomographie (µCT) sowie Kernspinresonanztomographie (NMR) bzw. Resazurin-Assay charakterisiert. Die Zugabe von Albumin war eine effektive Methode, um Schäume auch nach dem Druckvorgang zu stabilisieren, was zu einer verbesserten Materialporosität führte. Albumin erhöhte auch die Druckbarkeit des Ausgangsmaterials sowie das induzierte Bakterienwachstum. Die experimentellen Ergebnisse zeigten einen höheren Wassergehalt bei zunehmender Porosität und folglich eine höhere effektive Zelllebensfähigkeit.

Um die Materialstabilität zu erhöhen und deren Auflösung in bestimmten Lösungen zu vermeiden, wurde eine Strategie zur Synthese eines Ausgangsmaterials entwickelt, die für den 3D-Biodruck und die kovalente Vernetzung mechanischer Materialien mit eingebetteten lebenden Bakterien geeignet ist. Die Verarbeitungsroute basiert auf einem hochpartikelgefüllten Aluminiumoxid/Chitosan Gel-Nanokomposit, das durch elektrostatische Wechselwirkungen und kovalente Bindung unter Verwendung von Alginat bzw. Genipin doppelt vernetzt ist. Die Eigenschaften des Ausgangsmaterials und die Vernetzungszeit wurden mittels Rheologie untersucht. Weiterhin wurden die Stabilität des vernetzten Materials in verschiedenen Lösungen und die Biokompatibilität analysiert. Die Zugabe von Alginat war für die Druckbarkeit und die effektive bakterielle Lebensfähigkeit unerlässlich, da Proben ohne Alginat keine bakterielle Lebensfähigkeit zeigten. Das kovalent vernetzte Material löste sich erfolgreich nicht in Phosphatgepufferter Salzlösung (PBS), Salzsäure (HCl), Natriumhydroxid (NaOH) oder Wasser.

Die im Rahmen dieser Arbeit erzielten experimentellen Ergebnisse zeigen das Potenzial der beschriebenen Ansätze zur Herstellung poröser makroskopischer bioaktiver Materialien mit komplexen 3D-Geometrien unter Verwendung ausschließlich natürlicher Materialien als Plattform für neuartige Anwendungen in der Bioprozesstechnik.

1

Introduction

Chapter 1 has been partially adapted from Bioprocess and Biosystems Engineering, 2019 - 42(7): p. 1215-1224 (DOI: 10.1007/s00449-019-02119-4) with permission from Springer Nature number 5265951472044 [1], from Journal of Materials Science, 2022 - 57, 3662–3677. (DOI: 10.1007/s10853-021-06829-7) with permission from Springer Nature [2], and from Bioprocess and Biosystems Engineering, 2022 - 45: p. 171-185. (DOI: 10.1007/s00449-021-02650-3) with permission from Springer Nature [3].

1.1 Introduction

Biotechnology is a growing field that supports our daily life from the food we eat, the water we drink, the clothes we wear, up to the control and treatment of diseases [4, 5]. Cell immobilization has revolutionized biotechnological applications in bioprocessing by turning this process simpler, more controlled and more affordable. For instance, the immobilization of microorganisms and bio-entities into semi-permeable hydrogels simplifies the bioreactor process of separation and purification, since the material can be easily separated from the solution, reducing costs and processing time [6-9]. Furthermore, the immobilization of microorganisms into hydrogels results in additional protection from toxic substances as well as adverse surroundings and microorganisms showed higher viability under certain circumstances [10, 11]. Additionally, higher cell densities and cell loads can be achieved by cell immobilization, which can increase productivity and efficiency of bioreactions [12, 13].

Immobilization of cells in hydrogels or hydrogel nanocomposites has quickly become an established strategy for designing materials for tissue engineering and for biotechnological processes [14, 15]. Yet, immobilizing living cells in artificial materials is not an easy task and necessitates the use of both biocompatible starting materials as well as fully biocompatible processing steps. Moreover, support materials for bioreactions require a certain range of porosity to permit the proper nutrient exchange. Small-sized pores (nm scale) are essential for nutrient adsorption/retention as well as for structural support. Middle-sized pores (µm scale) are desired for cell proliferation as well as nutrient diffusion while big-sized pores in the mm scale decrease diffusion pathways and therefore enhance the permeability of the material and accessibility of embedded cells [16, 17]. As a result, the processing of hydrogels with suitable rigidity to maintain the porosity is still a challenge.

Oxide ceramic particles, such as alumina, are interesting reinforcement materials to increase hydrogel mechanical properties due to high hardness, chemical stability, and biocompatibility. However, high shear forces in the feedstock due to the particles can be

detrimental to cells. Consequently, the search for new materials and processing strategies to assure long-term stability in biological environments, mechanical rigidity, porosity, and high cell viability is still very challenging, especially considering that the production of mechanically rigid and insoluble substrates usually requires non-biocompatible processes like chemical crosslinking or sintering [18-20].

This work aims to contribute to the process engineering field by developing new processing strategies for microorganism immobilization into rigid porous materials for bioprocessing applications using biocompatible materials. Here, microorganism behavior and accessibility in the different immobilization strategies as well as the influence of porosity on the overall biotransformation performance were investigated. This thesis is divided into eight chapters, starting with this general introduction. Chapter 2 gives a proper contextualization and review of previous works done on cell immobilization and processing routes for porous materials. Chapter 3 describes the materials, bacteria strains, and assays used to characterize cell viability as well as material characterization methods used to characterize the produced bionanocomposites.

The main results of this thesis are presented and discussed in Chapter 4, 5 and 6 along with the description of each respective suspension and feedstock preparation. In Chapter 4 bacteria *Escherichia coli* or *Bacillus subtilis* were immobilized via a one-pot processing route based on the reinforcement of an alginate hydrogel with alumina nanoparticles, followed by internal/external ionotropic gelation steps. The results showed promising outcomes for this strategy, yet the accessibility of the cells was hindered due to the size of the sample. Furthermore, samples started to dissolve after 7 days of usage due to the weak crosslinking bonding [1]. To overcome these two drawbacks separately, two strategies were developed using 3D bioprinting. In Chapter 5, a feedstock for 3D bioprinting with a hierarchical pore structure to minimize mass transport limitations in bioprocessing applications was developed. The bioink is a highly particle-filled feedstock based on alginate, alumina nanoparticles, embedded *E. coli* bacteria, and external ionotropic gelation for crosslinking [2]. Second, to overcome the material stability drawback, in Chapter 6 a feedstock based on chitosan hydrogel reinforced with alumina and embedded *E. coli* was developed and crosslinked by electrostatic interactions and covalent bonding using alginate and genipin, respectively [3]. Chapter 7 summarizes the knowledge gained from this thesis and states its significance to the field while Chapter 8 gives an outlook with scientific questions and further processing ideas which arose from this work.

1.2 References

1. Condi Mainardi, J., K. Rezwan, and M. Maas, *Embedding live bacteria in porous hydrogel/ceramic nanocomposites for bioprocessing applications.* Bioprocess and Biosystems Engineering, 2019. 42(7): p. 1215-1224.
2. Condi Mainardi, J., K. Rezwan, and M. Maas, *Genipin-crosslinked chitosan/alginate/alumina nanocomposite gels for 3D bioprinting.* Bioprocess and Biosystems Engineering, 2022. 45(1): p. 171-185.
3. Condi Mainardi, J., et al., *3D bioprinting of hydrogel/ceramic composites with hierarchical porosity.* Journal of Materials Science, 2022. 57(5): p. 3662-3677.
4. Rosa, S.S., et al., *mRNA vaccines manufacturing: Challenges and bottlenecks.* Vaccine, 2021. 39(16): p. 2190-2200.
5. Syldatk, C., et al., *Mikrobielle Prozesse*, in *Bioprozesstechnik*, H. Chmiel, Editor. 2011, Spektrum Akademischer Verlag: Heidelberg. p. 477-505.
6. Zhang, B.-B., et al., *Robust and Biocompatible Hybrid Matrix with Controllable Permeability for Microalgae Encapsulation.* ACS Applied Materials & Interfaces, 2016. 8(14): p. 8939-8946.
7. Kang, A., et al., *Cell encapsulation via microtechnologies.* Biomaterials, 2014. 35(9): p. 2651-2663.
8. Gombotz, W.R. and S. Wee, *Protein release from alginate matrices.* Advanced Drug Delivery Reviews, 1998. 31(3): p. 267-285.
9. Das, M. and A. Adholeya, *Potential Uses of Immobilized Bacteria, Fungi, Algae, and Their Aggregates for Treatment of Organic and Inorganic Pollutants in Wastewater*, in *Water Challenges and Solutions on a Global Scale*. 2015, American Chemical Society. p. 319-337.
10. Böttcher, H., et al., *Biocers: ceramics with incorporated microorganisms for biocatalytic, biosorptive and functional materials development.* Journal of Materials Chemistry, 2004. 14(14): p. 2176-2188.
11. Martín, M.J., et al., *Microencapsulation of bacteria: A review of different technologies and their impact on the probiotic effects.* Innovative Food Science & Emerging Technologies, 2015. 27: p. 15-25.
12. Nedovic, V., et al., An overview of encapsulation technologies for food applications. Procedia Food Science, 2011. 1: p. 1806-1815.
13. Kourkoutas, Y., et al., Lactobacillus casei cell immobilization on fruit pieces for probiotic additive, fermented milk and lactic acid production. Process Biochemistry, 2005. 40(1): p. 411-416.

14. Yasouri, F.N. and H.A. Foster, *Improved yield of antibiotics by immobilization of cells of myxobacteria.* Biotechnology Techniques, 1991. 5(2): p. 149-152.
15. Al-Jwaid, A.K., et al., *One-step formation of three-dimensional macroporous bacterial sponges as a novel approach for the preparation of bioreactors for bioremediation and green treatment of water.* RSC Advances, 2018. 8(54): p. 30813-30824.
16. Bao, G., et al., *Triggered micropore-forming bioprinting of porous viscoelastic hydrogels.* Materials Horizons, 2020. 7(9): p. 2336-2347.
17. Shao, L., et al., *Sacrificial microgel-laden bioink-enabled 3D bioprinting of mesoscale pore networks.* Bio-Design and Manufacturing, 2020. 3(1): p. 30-39.
18. Berillo, D., A. Al-Jwaid, and J. Caplin, *Polymeric Materials Used for Immobilisation of Bacteria for the Bioremediation of Contaminants in Water.* Polymers, 2021. 13(7): p. 1073.
19. Lapponi, M.J., et al., *Cell immobilization strategies for biotransformations.* Current Opinion in Green and Sustainable Chemistry, 2022. 33: p. 100565.
20. Ge, X., L. Yang, and J. Xu, *Cell Immobilization: Fundamentals, Technologies, and Applications*, in *Industrial Biotechnology*. 2017. p. 205-235.

2 State of the art

2.1 Bioprocessing

Bioprocessing can be defined as the use of enzymes, microorganisms, plant cells, and animal cells as biocatalysts in a bioreactor to produce pharmaceuticals, foods, flavors, fuels, and chemicals [1]. The use of bioprocesses is not a new science and has been used for years in the fermentation of beer, wine, and bread [2]. Still, in the past years, increasing technologies and studies on the improvement of processing strategies and genetic handling allowed new discoveries and fast improvements in the biotechnological field [3]. Nowadays, the main applications of industrial biotechnology besides food industry are in the metabolite production of organic solvents, antibiotics, enzymes, vitamins, insulin, and vaccine production [4-6] as well as in the production of biofuels, recovery of metals and minerals, and waste-water treatment [7-9].

Despite the many advantages of using cells for bioprocessing, bioprocesses are cost-intensive and at the same time complex. Some organisms require special parameters such as temperature, pH, aeration, special organic matter, and time for proliferation [10]. Cells can produce metabolites intracellularly or extracellularly. For intracellular products, a rupture of the cell membrane is necessary to extract the metabolite, causing cell death. Extracellular products are released into the suspension and therefore, downstream processing steps of separation of product-containing suspension and the microorganisms are necessary, which often involves solution filtration and centrifugation steps, which is time-consuming and results in an increase in costs. Furthermore, filtration and centrifugation steps can damage cells and the reuse of these cells is hampered [10-12].

Thus, the industrial application of biotechnological strategies is limited by two main factors: the lack of long-term operational stability and the difficult recovery and reuse of the cells. Furthermore, harsh environmental conditions such as pH, organic solvents, and cytotoxic ions and molecules restrict the use of cells in bioprocessing [7, 13]. To overcome these drawbacks, Thomas M. S. Chang developed in the early 1960s a new method for immobilizing biological material into semi-permeable substrates. The immobilization strategy enables a wider range of uses for living matter with minimal loss of properties and productivity, which further details are going to be discussed in chapter 2.2 [14, 15]. Nevertheless, cell immobilization strategy brings many challenges for both engineers and biologists.

2.2 Cell immobilization

Cell immobilization was a key innovation in biotechnology since it provides protection to the cell from unfavorable conditions, such as toxic media and harsh pH by avoiding direct contact between cells and media. Furthermore, cells can be reused, washout problems are reduced, and cells are protected from high shear stresses [16]. Cell immobilization localizes the cells into a defined region in a way that their catalytic activity can be maintained and used repeatedly and, if needed, continuously. This strategy has applications in the bioprocessing field not just in the production of biochemical and environmental engineering [17], but also in the food industry, tissue engineering, treatment of diseases, and vaccine production [18-21] (Figure 2.1). The variety of applications implicate the need to design a variety of bioreactor configurations suitable for the intended purpose. Thus, biologists and engineers have been working together in the development of suitable immobilization strategies and materials to achieve high cell density, as well as high cell viability and reaction rate.

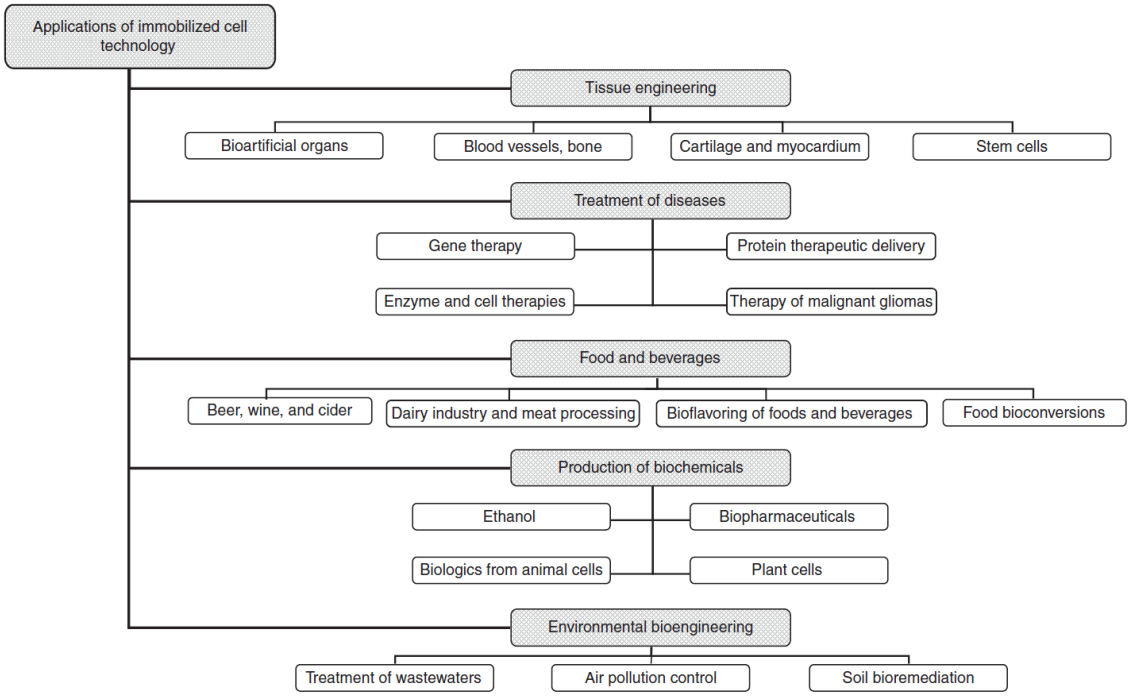

Figure 2.1 – Overview of applications for cell immobilization. Reproduced from [22] with permission from Elsevier number 5265320166301.

Immobilization methods are classified in basically two categories: carrier binding and entrapment (Figure 2.2) [22, 23]. Carrier binding methods attach cells onto the surface of a highly porous water-insoluble carrier by physical adsorption or by covalent bonds [24]. This immobilization technique can be either achieved naturally or induced artificially by using linking agents and results in direct contact between nutrients and cells. For instance,

physical adsorption is the simplest and longest known immobilization method and takes place though van der Waals interactions, ionic forces, or hydrogen bonds [23]. Since physical adsorption is based on weak binding forces, it results in a high washout of the adsorbed cells during use. To overcome this drawback, cells can be also attached by covalent binding onto the carrier surface. However, binding crosslinks are usually cytotoxic and reduce cell viability and therefore this method is more often applied just for enzyme immobilization rather than whole-cell immobilization [25].

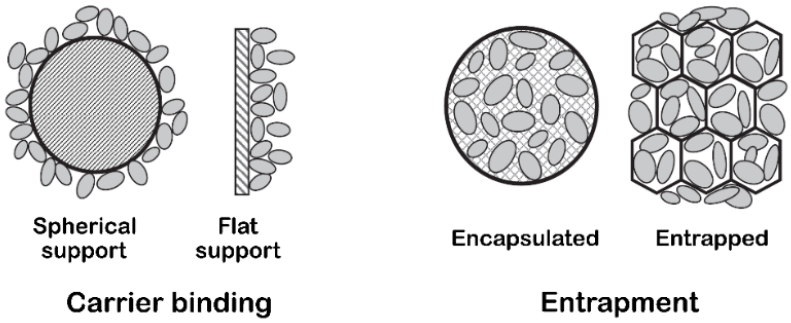

Figure 2.2 – Visualization of cell immobilization strategies of carrier binding or entrapment. Adapted from [22] with permission from Elsevier number 5265320166301.

The entrapment method implicates the envelopment of cells within a semi-permeable support matrix and it is the most used immobilization method for bioprocessing [26]. This method allows immobilization with high cell density and offers cell protection from external stresses and harsh environments, such as pH and toxic media. However, cell entrapment limits the influx of substrate and oxygen accessibility through the membrane into the cells and the efflux of metabolic waste. This will be discussed in more detail in chapter 2.3. The support matrix is usually a crosslinked polymer that can be either physically or covalently bonded [27]. Physical bonds are based on van der Waals interactions, ionic forces, or hydrogen bonds. This method entraps cells using mild crosslinking conditions and results in high cell viability. However, similar to carrier binding immobilization, these bond forces are weak, and the material can degrade and release cells into the reaction media [28, 29]. To avoid this drawback, the polymer matrix can also be covalently crosslinked but again chemical crosslinking is usually cytotoxic and reduces cell viability.

Many factors have to be considered when developing a stable and physiological environment for cell immobilization, such as chemical composition, surface morphology, surface charge, mechanical, and chemical stability and adequate pore size/porosity, which is essential for nutrients to reach the encapsulated cells within the material. Several strategies and materials have been developed in the past years to establish high cell viability, high reaction rate, and high material stability. Hydrogels are the most suitable

material for cell entrapment due to their high-water content and high biocompatibility [30, 31]. Therefore, most of the studies have been focusing on cell entrapment in hydrogels and some promising results have been achieved by immobilizing cells in hybrid matrices, such as hydrogel nanocomposites [13, 32, 33].

2.2.1 Cell immobilization in hydrogels

Hydrogels are a three-dimensional polymer network composed mainly of water. These polymers are highly hydrophilic and, when in an aqueous environment, water infiltrates the hydrogel network and causes swelling, while electrostatic or covalent bonds present in the network stop its dissolution [30, 31]. The high-water content of this class of materials assures high biocompatibility and therefore they have important applications in biomedicine and bioengineering. The biocompatibility of the hydrogel is governed by both material properties and crosslinking principle [34,35].

Hydrogels can be crosslinked by either physical or chemical bonds [34]. Crosslinking hydrogels by physical bonds can take be achieved by ionic interaction (ionotropic gelation) or polymer interactions (polyelectrolyte complexation). Ionotropic gelation describes the gel formation by the complexation of charged polymers with oppositely charged ions. Based on the same principle, polyelectrolyte complexation describes the gel formation by the complexation of two oppositely charged polymers [36]. Both strategies are widely used for cell immobilization due to their high biocompatibility. Physically crosslinked bonds are reversible and result in stiff gels and it is a simple and highly biocompatible strategy to crosslink hydrogels which, however, results in easily degradable gels. Chemically crosslinked hydrogels result in more stable and resistant hydrogels and are formed by a chemical reaction between the polymer and another polymer or molecule. Yet, biocompatibility and mechanical characteristics are going to depend on the crosslinking type and density [30, 31, 34, 37]. Two natural polymers stand out in cell immobilization due to their high biocompatibility and easy supply: alginate and chitosan. Both are gelling polysaccharides, but they have different properties which are going to be discussed here.

Alginate gels

Alginate is an anionic polymer naturally found in marine brown seaweed or certain species of bacteria that possess a natural tendency to form gels. It has low toxicity, low cost, high biocompatibility, and its gelation can take place at room temperature and physiological pH by ionotropic gelation. Alginate is a copolymer that consists of consecutive or alternating blocks of (1,4)-ß-D-Mannuronate (M) and (1,4)-α-L-Guluronate (G) (Figure 2.3) [38-41]. The carboxylic acid group of the alginate backbone gives this polymer an anionic charge

and therefore this polymer can be crosslinked by ionotropic gelation with multivalent cations such as calcium (Ca^{2+}), magnesium (Mg^{2+}) and iron (Fe^{2+} / Fe^{3+}). Both consecutive (MM or GG) or alternating (MG or GM) blocks are responsible for the crosslinking but the GG blocks play a more important role. GG blocks have a bucket shape and cations can be perfectly located exactly between two mirroring chains and this junction is referred to as the "egg-box" model (Figure 2.3). Thus, crosslinking GG blocks result in stiffer gels with more stable connections while crosslinking MM or MG/GM blocks result in easily degradable gels [39, 41, 42].

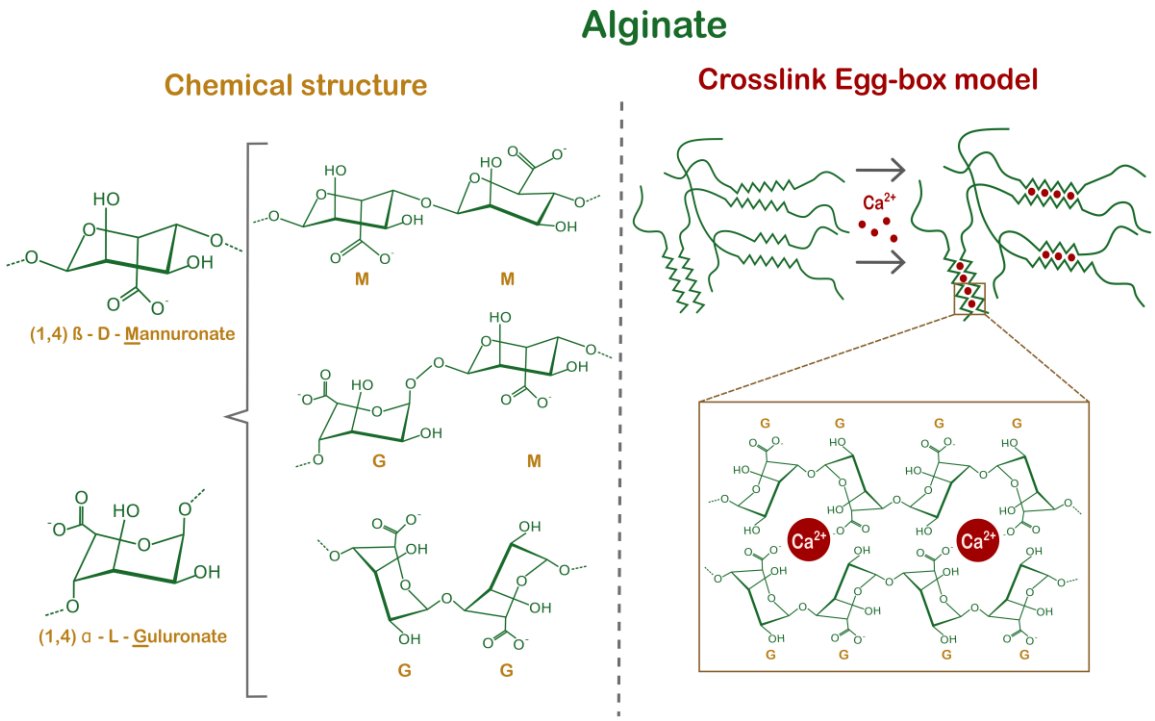

Figure 2.3 – Chemical structure of alginate, which consists of a combination of D-Mannuronate (M) or L-Guluronate (G) monomers. The monomers can form GG, MM or MG blocks whereas the GG blocks form a more stable crosslinking with calcium cations forming an "egg- box" structure.

The crosslinking of alginate with Ca^{2+} is formed almost instantaneously and this technique is used to encapsulate cells in microspheres. For that, cell-containing alginate solution is usually dropped into a calcium chloride solution and the sphere size will be defined by the drop size [42]. This external gelation takes place from the outside towards the inside of the droplet and, due to cation diffusion gradient established from the non-gelled center toward the boundaries, an inhomogeneous gelation takes place (Figure 2.4 – a-d) [26]. Since diffusion is the limiting factor, external gelation is typically used for small beads (< 5 mm) [38, 43]. More uniform gelation can be achieved by internally crosslinking the alginate droplet. Internal gelation describes a pH-controlled dissociation of an insoluble salt, such

as calcium carbonate, which is distributed inside the gel matrix, resulting in controlled and slow release of Ca^{2+} ions (Figure 2.4 – e-g). While external gelation results in stiffer gels with higher encapsulation efficiency, internal gelation results in a slower and more controlled gelation which allows better control of porosity, crosslinking density and, sample shape [26, 41, 44, 45].

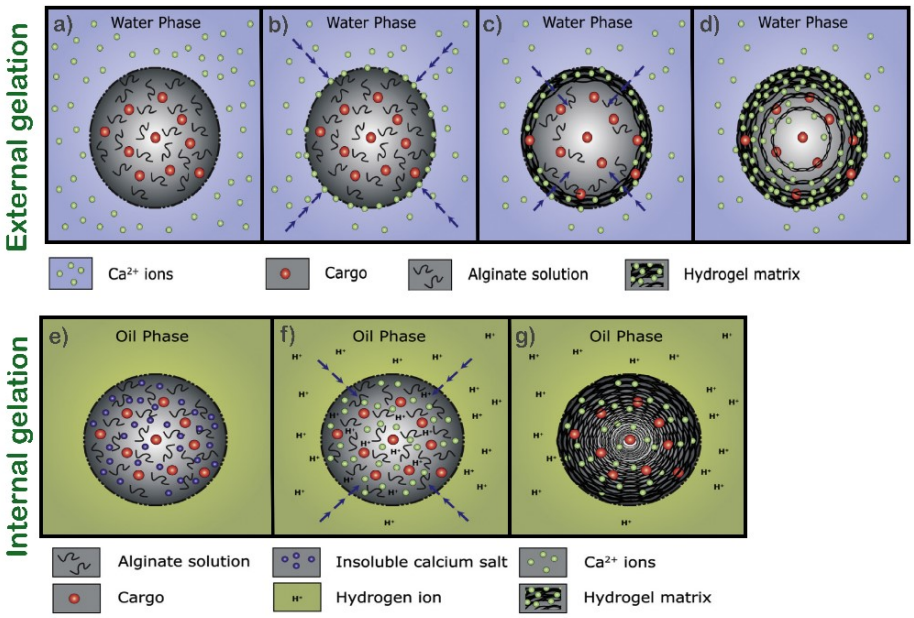

Figure 2.4 – Differences between external and internal gelation of alginate beads. Adapted from [44] with permission from Elsevier number 5265320541033.

Chitosan gels

Chitosan is a biocompatible product of the deacetylation of chitin, which is the most abundant natural polysaccharide on earth after cellulose and is found in crustacean shells [46]. The resulting polymer is based on a polysaccharide backbone with a primary amine group and is able to form a hydrogel. The amine groups on the chitosan backbone give a positive charge to this polymer. Chitosan can be dissolved in acidic pH (i.e. pH < 6.2) but not in neutral pH [47, 48]. Additionally, chitosan can show antimicrobial activity depending on its molecular weight and acetylation degree [49]. Chitosan microspheres can be produced by crosslinking chitosan with anionic ions (ionotropic gelation). The most used polyanion to crosslink chitosan by ionotropic gelation is sodium triphosphate, which dissociates in water into Na^{+} and PO_4^{-3} ions. In this case, a chitosan suspension is crosslinked with triphosphate solution under agitation to form microspheres, for example for drug encapsulation [48, 50]. The chitosan particles can be slowly dissolved and slowly release the encapsulated drug. For long-term applications chitosan can be covalently crosslinked by using glutaraldehyde molecules or, more recently, using genipin molecules

[47, 49, 51]. Glutaraldehyde can easily crosslink chitosan because of its active aldehyde groups. The reaction involves the formation of a Schiff's base via nucleophilic attack by nitrogen of the amine group from chitosan on the carbon on the glutaraldehyde, which displaces the oxygen of the aldehyde resulting in a C≡N bond [50]. However, glutaraldehyde shows high cell toxicity and, therefore, chitosan-glutaraldehyde crosslinked systems show low biocompatibility [53].

An innovative alternative for covalently crosslink chitosan is to use genipin as a crosslinking agent, which is a natural molecule extracted from the fruits of *Gardenia jasminoides* [54]. Genipin is a small molecule with very low toxicity, and it is able to crosslink proteins and polysaccharides containing amine groups [55-57]. This crosslinking proceeds in two separate reactions, first the formation of a heterocyclic compound of genipin linked to the glucosamine residue in chitosan and second a nucleophilic substitution of its ester group to form a secondary amide link with another chitosan molecule (Figure 2.5) [51, 58, 59]. Simultaneously, polymerization can take place between genipin molecules already linked to amino groups of chitosan which leads to the crosslinking of amino groups by short genipin copolymers.

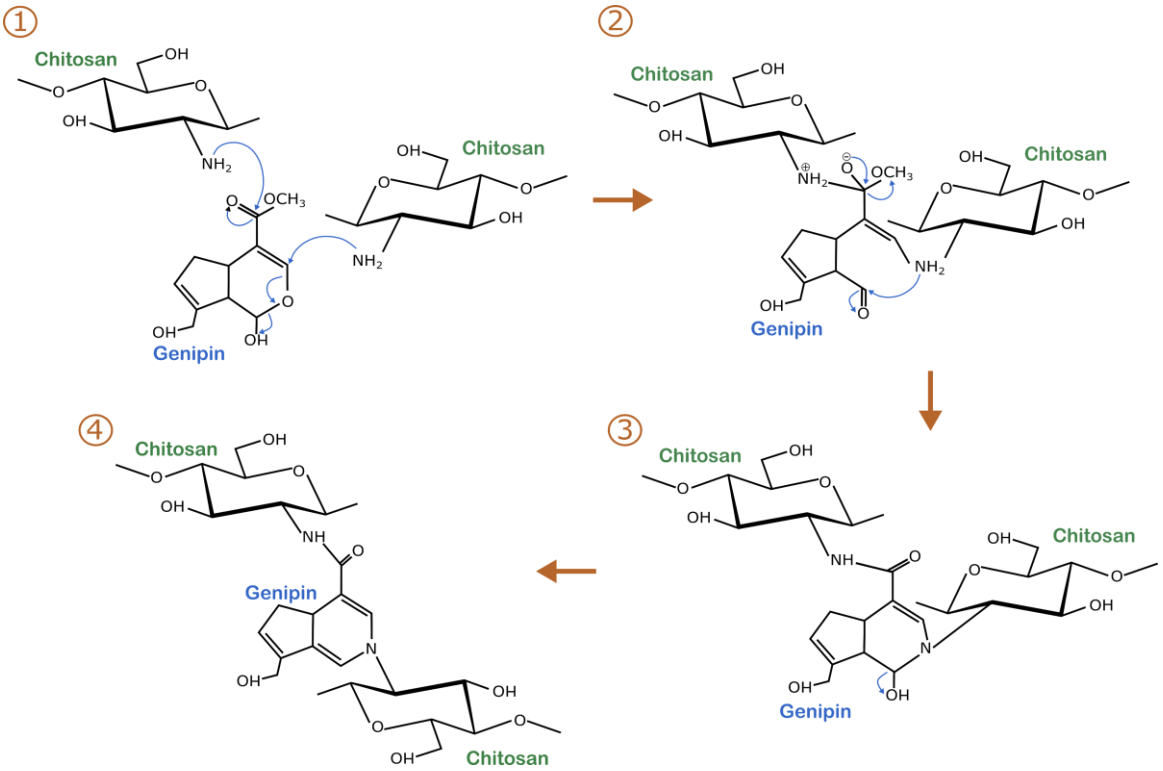

Figure 2.5 – Illustration of the crosslinking reaction between genipin and two chitosan molecules.

The properties of genipin-chitosan hydrogels can be adjusted to allow both mechanical properties and cell viability. Delmar et al. [60] investigated chitosan-genipin crosslinking at

different chitosan and genipin concentrations. They demonstrated an optimal genipin concentration for gel formation between 0.05 and 0.2% while genipin concentration above 0.2 % turned the gel into a brittle gel and resulted in phase separation of water/crosslinked gel at all tested chitosan concentrations (0.6 to 1.8 %). Moreover, Gao et al. [57] investigated the interactions of mouse fibroblast cells with genipin-crosslinked chitosan gels. Genipin-crosslinked chitosan hydrogels did not show any cytotoxic effect at 1-2 wt.% chitosan and 1.64 – 5.50 mM genipin. They observed that by increasing genipin concentration the stiffness of the gel increased in consequence a higher cell adhesion could be observed.

Alginate/chitosan gels

Alginate and chitosan are widely used together due to the complementary functional groups of both polymers and can either be chemically or physically crosslinked [61-64]. Chemical crosslinking between alginate and chitosan involves the carbodiimide conjugation reaction where amine groups of the chitosan backbone crosslink with carboxylic acid groups from alginate. This technique works via the activation of carboxyl groups for direct reaction with primary amines to achieve amide bond formation. The reaction is based on a chemical strategy that combines 1-ethyl-3-(3-dimethylaminopropyl) carbodiimide hydrochloride (EDC) and N-Hydroxysuccinimide (NHS) but is not biocompatible with cells [66].

A more biocompatible strategy is based on physically crosslinking chitosan and alginate. Chitosan, a positively charged polymer, and alginate, a negatively charged polymer, can be crosslinked by polyelectrolyte complexation [66, 67]. This technique has the same principles of ionotropic gelation but instead of using charged ions for crosslinking another polymer is used [66, 68, 69]. Chitosan-alginate polyelectrolyte complexation is a widely used encapsulation method, usually by first encapsulating cells in alginates microspheres via ionotropic gelation, followed by a coating with chitosan via polyelectrolyte complexation (PEC). Colosi et al. [70] used the same principle for 3D printing by first printing alginate suspensions (without cells) followed by a coating step with chitosan, and the coating was further reinforced by covalent crosslinking to assure the structural stability of the materials in culture media for a prolonged period.

2.2.2 Cell immobilization in hydrogel nanocomposites

Hydrogels are a three-dimensional polymer network composed mainly of water and have promising applications in biological-related fields due to their high-water content and tunable physical, chemical, and biological properties. Nevertheless, hydrogels usually

possess poor mechanical properties [71, 72], and there is a demand for multifunctional hydrogels for biosensors [73], drug delivery [74], regenerative medicine [75, 76] and wound dressing [77]. To meet requirements for bioprocessing and biomedical applications, nanoparticles can be integrated into the hydrogel to form a hydrogel nanocomposite with unique properties that can be engineered by adjusting the interactions between nanoparticles and polymer chains [78-80].

Nanoparticles are incorporated into the hydrogel to improve hydrogel performance and functionality such as conductivity [81, 82], magnetic properties [83], stimuli-responsiveness [84, 85], permit cell adhesion [86] or even add antibacterial properties [87]. Different types of particles can be incorporated into the hydrogel such as organic particles, metal/metal oxide particles, inorganic/ceramic particles, and carbon-based particles to achieve the desired functionality for the application [80]. Nonetheless, the integration of new materials/nanoparticles usually does not interfere with the hydrophilic properties of the polymer [88]. Consequently, hydrogel nanocomposite gives rise to new material's performance and function while the original hydrophilicity and high-water content of the material are maintained.

Alumina particles (Al_2O_3) are a very interesting material due to their high chemical stability and hardness as well as excellent biocompatibility since it is a bioinert material. Y. Rotbaum et al. [89] used alumina particles and nanowires as reinforcement material in methylcellulose hydrogels to tune, control and improve mechanical properties without influencing the thermo-gelation properties of the hydrogel. Alumina powder (< 10 µm and 63-200 µm) and nanowires (ø 2-6 nm, length 200-400 nm) were tested, and by decreasing particle size a 20% lower strain at twice higher stress could be achieved in comparison to the hydrogel without particles. Furthermore, no difference in mechanical properties could be observed using < 10 µm particles and nanowires. Still, the use of alumina as reinforcement material has not been widely investigated in combination with cells yet.

Hydrogel nanocomposites protect the immobilized cells from external stresses and harsh substances while mechanical properties and chemical stability are improved [13, 90]. The design of hydrogel nanocomposites contains many challenges for cell immobilization since the presence of cells requires e.g. mild pH values, moderate temperatures, low shrinkage, shear stresses during processing, and biocompatibility of each material while sufficient oxygen/nutrient diffusion is guaranteed [91, 92].

Park et al. [32] encapsulated *G. xylinus* bacteria in alginate/TEMPO-oxidized bacterial cellulose (TOBC) hydrogel nanocomposites. The incorporation of 20% of TOBC resulted

in 60% higher compressive modulus, in comparison with samples without TOBC. Furthermore, the addition of TOBC induced cell proliferation from approx. 50 x 10^4 cells/mL for samples without TOBC to 130 x 10^4 for samples with 20% TOBC after 7 days of incubation. He et al. [33] encapsulated *R. planticola* bacteria in bentonite clay and alginate composites to develop a slow release of the biofertilizer bacteria into the soil. The incorporation of 4 wt.% bentonite showed a 40% slower degradation than samples without bentonite after 30 days, resulting in a longer and more constant release of bacteria while no influence of bentonite on cell viability was observed.

2.3 Nutrient transport in hydrogels and the importance of porosity

Porosity is a key factor during the design and synthesis of materials. Tailoring porosity by adjusting material's pore size, shape, and interconnectivity, as well as total porosity and specific surface area influence not just mechanical properties but also the gas/fluid diffusion and permeability in the material. Porous materials are classified depending on their pore size into micro- (< 2 nm), meso- (2 – 50 nm), and macropores (> 50 nm), whereas each classification is associated with a different regime of fluid transport [93]. Fluid transport, or fluid flux, is usually described by Fick's Law (Equation 1), where J means fluid flux, D is the diffusion coefficient, and $\partial c/\partial x$ is the concentration (c) gradient in a length x [94, 95]. Diffusion is fundamental in fluid transport and describes the movement of one chemical specie (atom or molecule) through a fluid with a concentration gradient. Different diffusion mechanisms can take place in either isolated or in combined phenomena and highly depends on pore size/shape, temperature, intermolecular interactions, fluid concentration, and viscosity as well as tortuosity.

$$J = -D\frac{\partial c}{\partial x} \qquad \text{Equation 2.1}$$

In micropores, activated transport dominates mass transport, since all molecules interact with the atoms/molecules on the materials surface by adsorption/desorption. In mesopores, there is an adsorbate concentration gradient between fluid/solid interphase and the bulk of the fluid, along with mono and multilayered molecule adsorption. Consequently, a more complex transport process takes place in mesopores by different transport regimes such as surface diffusion, Knudsen diffusion and/or capillary condensation (Figure 2.6) [96]. In surface diffusion, molecule movement occurs by adsorbed molecules hopping from site to site on the pore surface and plays an important role in surface reactions [97, 98]. Knudsen diffusion takes place when the pore diameter is smaller than the mean-free path of the molecule. The molecules bounce back and forth between the pore wall whereas collisions of the molecules with the pore wall are more

likely to happen than collisions between the molecules [99, 100]. Capillary condensation takes place when a depression effect caused by the saturated vapor pressure of the confined vapor occurs, resulting in the formation of an adsorbed film after vapor molecules were adsorbed onto the pore walls. [101]. Furthermore, in macropores, the movement of molecules takes place by molecular diffusion and/or viscous flow. Molecular diffusion is the random movement of the molecules in a fluid without agitation and above 0 K. Molecular diffusion takes place when the molecular agitation overcomes the viscous forces that tend to keep fluid elements aligned in parallel paths [102, 103]. Viscous flow is the flow of a liquid whereas the flow behavior can be either laminar or turbulent and the flow pattern depends on the viscosity, flow rate, temperature, pore size, and morphology. Laminar flow follows a well-defined straight path and moves in parallel layers while turbulent flow moves in an unsteady and random three-dimensional macroscopic mixing motion (Figure 2.6) [104, 105].

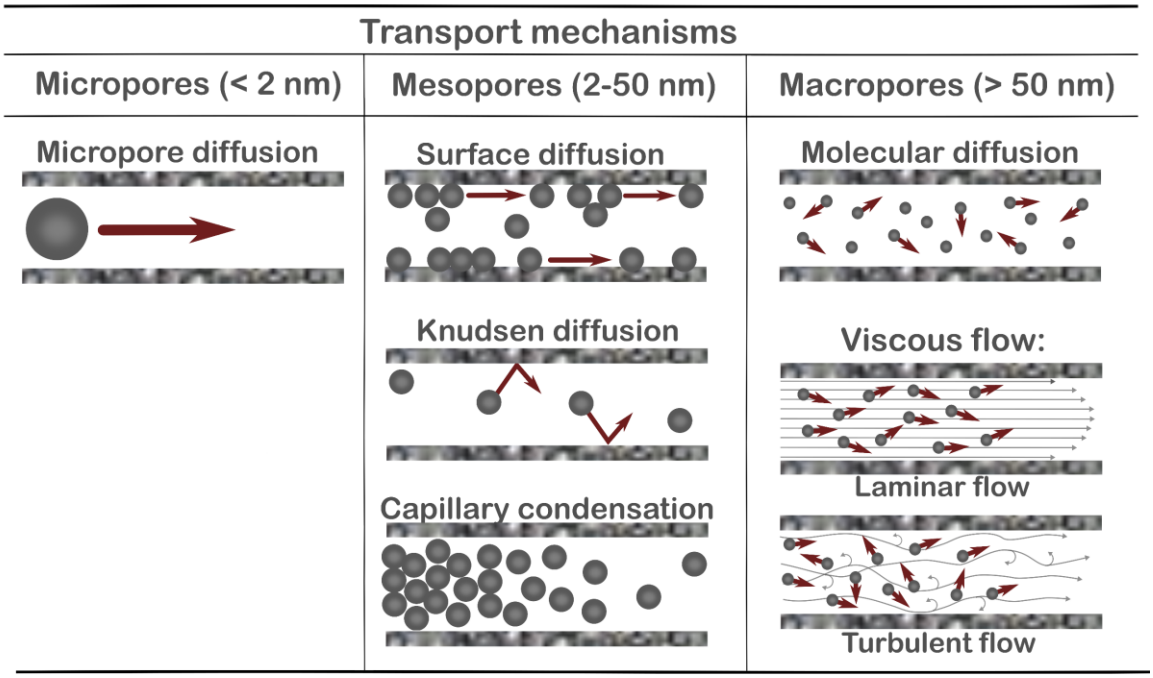

Figure 2.6 – Illustration of the different fluid transport mechanisms in micro-, meso- and macropores.

As stated before, hydrogels are a three-dimensional polymer network composed mainly of water. This polymer network is similar to a random spider web in 3D directions whereas the empty spaces (pores) are filled with water. These polymer networks from the hydrogels are usually in the mesoporous range and are composed of over 90% of water, resulting in an efficient system where molecules dispersed in water can easily diffuse inside the material [106]. Nevertheless, molecules and particles interact with the polymer network

and hinder the diffusion of substances inside the gel [107]. Thus, tailoring these interactions is a key factor for developing cell immobilization carriers.

Alginate gels, for example, usually exhibit a mesoporous structure [40, 108] and this semi-permeable material plays an important role in the oxygen/nutrient transport for encapsulated cells. Hussain et al. [109] analyzed in more detail the influence of the alginate bead size on the diffusion of glucose through calcium alginate gels by measuring the conversion rate of glucose into ethanol of encapsulated *S. cerevisiae* yeasts. By decreasing bead size from 4 to 0.8 mm, the glucose consumption time reduced 50% at a 4 mL/min flow rate, since decreasing bead size reduces the diffusion pathway and increases mass transport. Furthermore, Shuster et al. [110] analyzed the influence of internal and external gelation of alginate by measuring the diffusivity of different dextran molecules. The diffusion of 17 nm dextran molecules was three times higher for samples produced by external gelation than by internal gelation whereas a reduction of 65% in diffusivity of 120 nm molecules was observed for samples produced by external gelation, in comparison to 17 nm molecules.

Fluid transport and diffusion mechanisms depend on the pore size/shape as well as molecule/particle size while different mechanisms can act at the same time. Yet, fluid flux and permeability are higher and allow bigger molecule/particle diffusion in macropores in comparison with micro- and mesopores. In counterpart, molecule adsorption on micro- and mesopores is much higher than in macropores, facilitating catalytic reactions. Thus, each pore size/shape has its own benefits and, to optimize fluid transport and reaction processes, ideally a combination of different pore sizes in a hierarchical structure is desired [111-113].

2.4 Processing route of porous materials

Hydrogels are generally biocompatible materials, but cell entrapment can be detrimental for the cells due to diffusion limitations, which often hinder the supply of nutrients and oxygen to the cells [22, 24, 25], as well as hinder the proliferation of immobilized cells [114-116]. Consequently, there is a demand for hydrogel materials with hierarchical pore structures including larger interconnected pores to enable effective diffusion of nutrients/oxygen towards the material as well as cell proliferation and that also exhibit good structural fidelity and adequate mechanical properties. Ideally, structures containing cells require a broad range of pores from nm to mm scales (hierarchical porosity). Small pores (nm scale) are essential for nutrient adsorption/retention as well as for structural support. Middle-sized pores (μm scale) are desired for cell proliferation as well as nutrient

diffusion while pores in the mm scale decrease diffusion pathways and therefore enhance the permeability of the material and accessibility of embedded cells [117, 118].

The incorporation of inorganic particles to form a hydrogel nanocomposite can increase the mechanical stability of these materials and permit the manufacture of complex porosity. Nevertheless, the presence of microorganisms limits material processing due to the physiological processing temperature, pH, and solvent as well as low shear forces during processing [89, 90]. Consequently, to incorporate pores into the hydrogel structure material processing must be specially adapted to allow high cell viability. Thus, three techniques stand out for porous material processing with microorganisms such as gel-casting, foaming, and 3D printing.

2.4.1 Gel casting

Gel casting was established in Canada in the 1960s to prepare compact ceramics [119]. Since then, it evolved into an attractive forming process for manufacturing near-net-shape, large, and high-quality complex ceramic parts. Gel-casting is a shaping technique of a fluid suspension containing particles, solvent, and a monomer/polymer which is poured into a mold. Additional polymerization of the monomers, or polymer crosslinking, to form a 3D polymer network is used to maintain the sample's shape while particles are integrated into the polymer 3D network [120, 121]. Thereafter, samples can be dried to remove the solvent followed by a sintering step to increase material density and mechanical properties.

Gel-casting is a straightforward process that uses low concentrations of monomer/polymer and the material's composition depends on the desired application with adjustable starting materials. Furthermore, gel-casting results in homogeneous materials and the material's green bodies show good mechanical properties. Initially, gel-casting was developed as a consolidation method to maintain the shape of ceramic foams [122] and in the last years, a broad variety of ceramic gel-casting processes have been developed, still based on polymerization or cross-linking of polymers. To develop ceramic pieces by gel-casting two important factors must be analyzed: gelation time and rheological properties. Gelation time is going to depend on the type and speed of the polymerization/crosslink reaction of the network and determines the time window for shaping the material. Conversely, the rheological properties of the suspension are going to determine the existence of undesired bubbles or the complete filling of the mold [123].

The concept of using soluble polymer to form a 3D network has already been used since the 1960s for the encapsulation of drugs, cells, and proteins with, e.g., chitosan [124, 125],

collagen [126, 127] and alginate [32, 35, 76]. More recently, Brandes et. al. developed a processing route for ceramics based on the ionotropic gelation of alginate-alumina suspensions to produce highly stable ceramic parts [128, 129]. They studied different cations as alginate crosslinkers and their influence on the mechanical properties of monolithic (non-porous) ceramics [130]. A 25% higher flexural strength after sintering at 1500°C could be achieved by crosslinking alginate-alumina suspensions with aluminum acetate (Al^{3+} cations) instead of using calcium iodate (Ca^{2+} cations), with flexural strengths of 324 MPa and 259 MPa, respectively. The microstructure of samples crosslinked with aluminum acetate showed more homogeneous and less porous alumina materials after sintering while calcium iodate crosslinked samples induced larger pores, grain growth, and an inhomogeneous microstructure. Thus, selecting the appropriate ion for crosslinking affects both the polymer network and the final properties of the ceramic.

2.4.2 Foaming

Materials with a foam-like structure exhibit special properties and features that usually cannot be achieved by dense materials, such as a high quantity of pores and surface for, e.g., thermal insulation, support for catalytic reactions, scaffold material, and filtration. Ceramic materials, for instance, are very interesting materials for foam materials due to their characteristically high melting point, corrosion, and wear resistance [131, 132]. To produce ceramics with a foam-like structure processing routes such as the replica technique, sacrificial templating and direct foaming can be implemented (Figure 2.7).

Replica technique

The replica technique consists of the impregnation of a porous template from synthetic or natural materials, such as polymer and coral materials, respectively, with a ceramic suspension or precursor. Thereafter, the impregnated porous structure is dried, followed by a sintering step to burn the template material resulting in a microporous ceramic with the same porous morphology as the original impregnated template [132, 133].

Sacrificial template

The sacrificial template technique consists of the preparation of biphasic suspensions containing a continuous matrix of ceramic particles and a homogenously dispersed sacrificial phase from natural or synthetic material, such as polymer spheres, nanorods, platelets, or oil droplets. Thereafter, the biphasic suspension is shaped into the desired geometry and sintered to eliminate the sacrificial phase, which leaves behind empty spaces in the material resulting in the porous structure [132, 133].

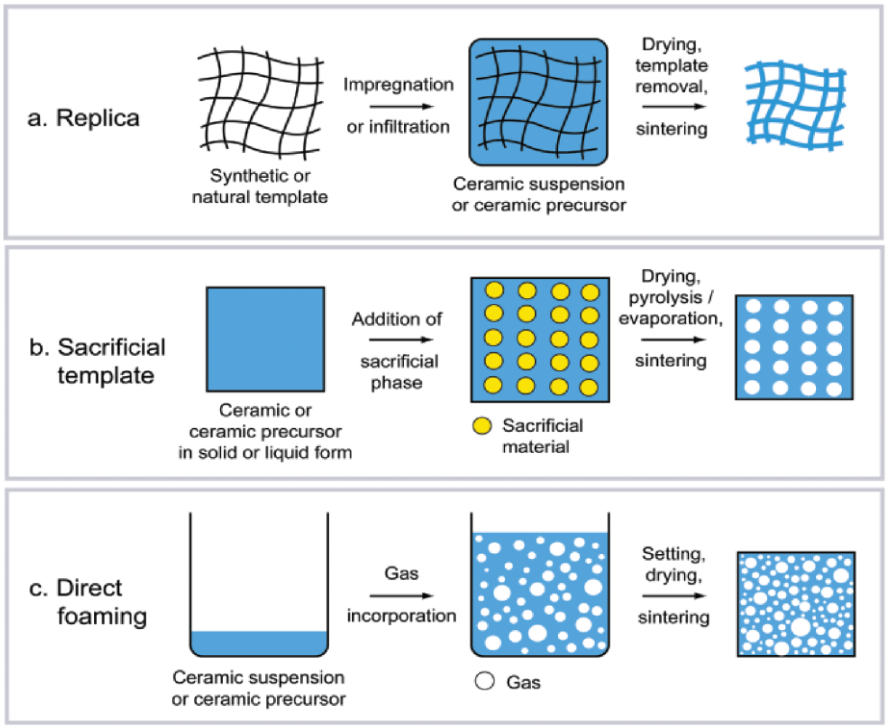

Figure 2.7 - Scheme of processing routes for producing porous ceramics: a) replica technique, b) sacrificial template, and c) direct foaming method. Reproduced from [132] with permission from John Wiley and Sons number 5265321085952.

Direct foaming

The direct foaming method is based on air incorporation (mechanical frothing, injection of gas, gas-releasing chemical reaction or solvent evaporation) into a ceramic suspension or liquid media to generate a foam. The material can be further sintered or used in the wet state, which is normally not very stable. The final porosity is determined by the amount of gas incorporated during the process, while the pore size is determined by the stability of the wet foam before setting [132, 134].

Wet foams are thermodynamically unstable systems due to their high gas-liquid interfacial area. To reduce the overall free energy of the system, physical processes of drainage (creaming), coalescence (film rupture), and Ostwald ripening continuously take place, which leads to foam destabilization [135]. Drainage corresponds to the physical separation between the liquid and gaseous phase due to gravity, forming a foam layer on the top while the heavier liquid phase is concentrated at the bottom. The reduction of the liquid phase results in a dense air bubble layer separated by thin films (foam lamella). These films' stability is determined by attractive/repulsive forces, in which van der Waals forces push the bubble against each other, resulting in a film rupture and coalescence of the bubbles. Bubble coalescence can be hindered by providing sufficiently strong electrostatic and/or steric repulsive forces to overcome the attractive van der Waals forces, which can

be provided by particles or surfactant molecules attached to the air/water interface [132, 135-137].

Furthermore, Ostwald ripening can take place between bubbles of different sizes due to differences in Laplace pressure between them, resulting in steady diffusion of gas molecules from smaller to larger bubbles over time [132, 135, 136]. Thus, the key aspects of the direct foaming technique are the stabilization and consolidation mechanisms of the bubbles, which determine if the bubbles are going to collapse within seconds, hours, days, or weeks. Particles and surfactants adsorbed on the air/water interface can significantly increase bubble stability and slow down coarsening processes.

Bubble stabilization with particles

Solid particles, such as silica [138-140], calcium carbonate [141], chitin [142], and cellulose [143, 144] microparticles with tailored surface chemistry can adsorb on the air/water interface and act on bubble stabilization [138]. This stabilization method is based on particle-stabilized Pickering-emulsions, where colloidal particles are used to stabilize high-energy interfaces. The adsorption of small particles at the air/water interface occurs when particles are not completely wetted by the water phase – partially hydrophobic particles. Reducing particle size results in a reduction in adsorption energy at the air/water interface, reducing bubble stability. Thus, particle adsorption on the air/water interface is ruled by particle size, the surface properties of the particle (hydrophobicity/hydrophilicity), which can be tuned by chemical treatments, and the position of the particles at the interface, which is described by the contact angle θ at equilibrium (Figure 2.8) [132, 135, 145, 146]. Best foam stabilization can be achieved with a contact angle > 90° (partially wetted particles) and no foams are achieved with contact angles near to zero (completely wetted particles) [147].

Bubble stabilization with particles showed to be a promising technique to impede bubble coalescence and disruption for several days, even if initial drainage is observed. Gonzenbach et al. [148] tuned the surface properties of initially hydrophilic alumina (30-1800 nm) and silica (80 nm) particles by the adsorption of short-chain amphiphiles, such as butyric acid, propyl gallate, and hexyl amine, to partially hydrophobized the particle surface. With this straightforward approach, bubbles ranging from 20-80 μm could be achieved via mechanical frothing and the foams were stable over days because of the irreversible adsorption of the partially hydrophobized particles at the air/water interface.

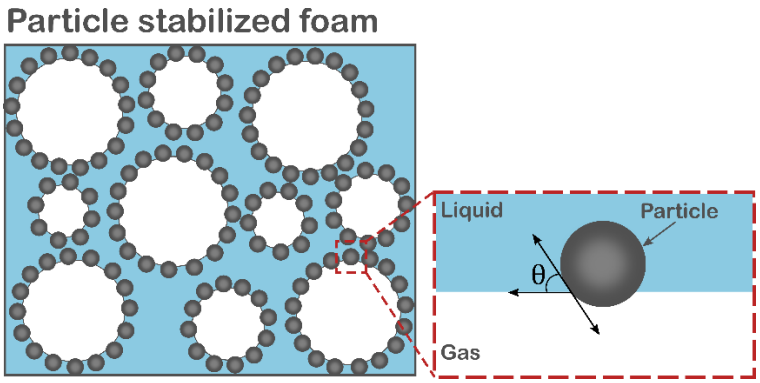

Figure 2.8 – Illustration of particle stabilized bubble.

Bubble stabilization with surfactants

Direct foaming of aqueous suspensions based on surfactants requires the addition of amphiphilic molecules and biomolecules more suitable to the system, such as polymers, lipids, silanes, and proteins. Surfactants are classified as nonionic-, anionic-, cationic-, and protein-surfactant [132]. Surfactants are long-chain amphiphilic molecules with a hydrophobic and a hydrophilic site that behave as surface active agents and are used for wet foam stabilization. These molecules adsorb at the bubble surface with the hydrophilic site in contact with the aqueous phase while the hydrophobic site point to the air phase to reduce the interfacial free energy (Figure 2.9) [136].

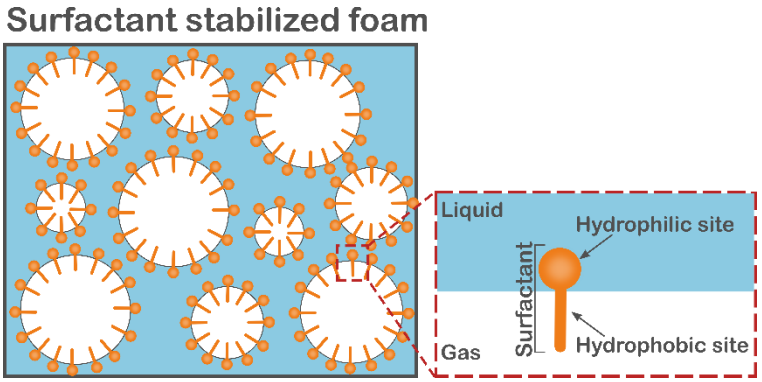

Figure 2.9 - Illustration of surfactant stabilized bubble.

Proteins are complex molecules that exhibit amphiphilic behavior, structural flexibility, and biocompatibility, and therefore are natural surfactants that can form thin films at air/water interfaces. Interfacial adsorption of proteins is often accompanied by the denaturation and unfolding of the adsorbed proteins, which adds to the stability of the interfacial film. By unfolding proteins, several hydrophobic regions result in multiple adsorption sites per molecule, which make spontaneous desorption of the whole molecule very unlikely [134, 149].

The properties of interfacial films, such as surface tension and elasticity, are altered by the surfactant molecule. Surfactants significantly decrease the interfacial energy of the surface tension, but the low adsorption energy of surfactants forms more unstable foams than particle-stabilized foams [132, 150]. Nonetheless, surfactants can significantly increase film elasticity at the air/water interface [151]. Maas et al. [152] analyzed the influence of lysozyme (LSZ), fibrinogen (FIB), and bovine serum albumin (BSA) proteins on bubble formation in hydroxyapatite (HAP) suspensions with a closer look at the rheological properties at the air/water interface. Interfacial shear rheology measurements showed that foams produced with BSA and FIB exhibited similar elastic moduli when dissolved in water or water/HAP suspensions. Conversely, suspensions produced with LSZ showed a decrease in elastic moduli when comparing proteins dissolved in water and water/HAP suspensions. Apparently, the strong Coulomb interaction between the positively charged LSZ molecules and the negatively charged HAP particles leads to a depletion of LSZ molecules at the air/water interface. LSZ are in this case adsorbed on the HAP particles and these proteins were no longer able to freely diffuse to the interface. This resulted in a dense material without bubble formation, since LSZ thin films were not sufficient to stabilize the interface of bubbles in the suspension, while FIB- and BSA-containing suspensions formed highly porous ceramic foams.

Wet foams are a metastable system and bubbles stabilized with long-chain surfactants collapse within a few minutes after air incorporation, while bubbles stabilized with proteins collapse within a few hours [153]. Thus, after the stabilization of direct foaming bubbles with surfactants or proteins, a further step of foam consolidation is required to prevent the foams from drainage or coarsening. Hence, foams can be consolidated e.g. via freeze casting, protein/polymer denaturation, or gel casting [133]. Freeze casting and protein/polymer denaturation are temperature-dependent consolidation methods based on cooling down the suspension to freezing temperatures (below zero degrees for water-based systems) or on heating the suspension over 60°C, respectively.

Furthermore, gel-casting can be used as a foam consolidation method which prevents the foamed body from collapsing [122]. Here, water-soluble polymers are added to the slurry and are crosslinked to consolidate the foam. Using gel-casting as a foam consolidation method enables the production of suspensions with lower viscosities and high solid content due to the small size of the polymer molecules, which results in a higher packing density and mechanical resistance of the foamed material even without sintering.

2.4.3 3D printing

Additive manufacturing or 3D Printing is the process of creating a three-dimensional object from computer-aided design (CAD) drawing data and depositing layer-by-layer of the material to create the final structure [154]. The first machine for rapid prototyping was developed in the 1980s and, since then, the research on this new technology has increased and the application fields have grown exponentially. The main applications of this process nowadays are in the aerospace, automotive, and biomedical industries [155]. It is a great advance in technology because it allows quick prototyping of parts, resulting in a reduction in manufacturing time, costs, and human interaction. Furthermore, 3D printing enables the manufacture of complex and customized geometries that are not possible using other manufacturing methods. Various printing methods have been developed in the past year and can be divided into four broad categories depending on the starting state of the material such as solid sheet, powder, liquid, filament, and paste (Table 2.1) [156].

Solid sheet-based systems

Laminated Object Manufacturing (LOM) is a 3D printing method developed by Helisys Inc. where layers of solid material are fused or laminated together using heat and pressure followed by cutting the attached layers into the desired shape with a computer-controlled laser. LOM technology is suitable for adhesive-coated paper, polymer, or laminated metal and its main advantage is the high fabrication speed. Nevertheless, printing precision depends on sheet thickness and thus it is not considered a very precise technique [154, 156].

Powder-based systems

Powder-based 3D printing produces parts by applying a localized heat source or binder to build each layer. Selective laser sintering (SLS), one of the first powder-based methods, involves the application of a high-power laser beam to partially melt a power-bed of thermoplastics, metals, and ceramic particles to build the 3D object layer by layer [157]. Furthermore, selective laser melting (SLM) fully melts metal particles using a laser beam to build the parts while electron beam melting (EBM) uses an electron beam to melt the metal powder. Additionally, laser metal deposition (LMD) uses a high-power laser beam but the powder material here is supplied by a feeding nozzle instead of in a powder bed as by SLS and SLM. Moreover, three-dimensional inkjet printing (3DP) uses an inkjet printing head to spray a liquid binder into a powder layer bed and the binder solidifies to form a solid layer. While SLS, SLM, EBM, and LMD focus on printing parts by partially or fully melting the powder material, 3D inkjet printing enables the customization of polymer, metal, and ceramic materials without heating [158, 159].

Table 2.1 – Overview of different additive manufacturing techniques and its applications sorted by the state of starting material. Adapted from [154] with permission from Elsevier number 5265321503225.

Starting material	Process	Material preparation	Layer creation technique	Phase change	Typical materials	Applications
Solid sheet	LOM	Laser cutting	Feeding and binding of sheets with adhesives	-	Paper, plastic, metal	Prototype, casting models
Powder	SLS	Powder in bed	Laser scanning	Partial melting	Thermoplastics, waxes, metal powder, ceramic powder	Prototypes, casting patterns, metal and ceramic preforms
	SLM	Powder bed	Laser scanning	Full melting	Metal	Tooling, functional parts
	EBM	Powder bed	Electron beam scanning	Full melting	Metal	Tooling, functional parts
	LMD	Powder injection through nozzle	On-demand powder injection and melted laser	Full melting	Metal	Tooling, metal part repair, functional parts
	3DP	Powder bed	Drop-on-demand binder printing	-	Polymer, metal, ceramic, and other powders	Prototypes, casting shells, tooling
Liquid	SLA	Liquid resin in a vat	Laser scanning/light projection	Photopolymerization	UV curable resin, ceramic suspension	Prototypes, casting patterns, soft tooling
	MJM	Liquid polymer in jet	Ink-jet printing	Cooling & photopolymerization	UV curable acrylic plastic, wax	Prototypes, casting patterns
	RFP	Liquid droplet in nozzle	On-demand droplet deposition	Solidification by freezing	Water	Prototypes, casting patterns
Filament/ Paste	FDM	Filament melted in nozzle	Continuous extrusion and deposition	Solidification by cooling	Thermoplastics, waxes	Prototypes, casting patterns
	Robo-casting	Paste in nozzle	Continuous extrusion	-	Ceramic paste	Functional parts
	FEF	Paste in nozzle	Continuous extrusion	Solidification by freezing	Ceramic paste	Functional parts

Liquid-based systems

Stereolithography (SLA), the first commercially available 3D printing technology, applies a focused ultraviolet (UV) light into a photosensitive liquid resin. The resin cures and solidifies by applying the UV light selectively for each cross-section. After a layer is built, the platform descends and another layer of fresh resin is added and cured, adhering to the previous layer. Here, ceramics and metals can be produced by incorporating ceramic or metal particles into the photo-curable suspension. Multi-jet modeling (MJM) uses an inkjet printer with multiple nozzles. Each nozzle dispenses individual jets of UV-curable

polymer or wax on demand, followed by UV light curing. Furthermore, rapid freeze prototyping (RFP) builds ice parts by selectively depositing and freezing water droplets layer-by-layer [154, 159].

Filament-based systems

Filament deposition modeling (FDM), the most common 3D printing method, utilizes a thermoplastic filament and creates a structure from the bottom up by using a printer head capable of heating the polymer to the melting point. The melted polymer is extruded through a nozzle and deposits the material layer-by-layer into the printed shape. FDM is also used to print composite materials when particles or fibers are incorporated into the filament. The development of fiber-reinforced polymer matrices overcomes the mechanical limitations of single polymers and extends the application range of FDM [159, 160].

Paste-based systems

Robocasting, also known as direct ink writing (DIW) or extrusion printing, extrudes a paste-like material through a small nozzle while the printing head moves to deposit the paste into the desired shape in a layer-by-layer pattern. The starting material here is typically a gel or ceramic suspension which exhibits liquid-like behavior when trespassing the nozzle but retains its shape immediately after extrusion [157, 161-163]. Therefore, robocasting relies on the extrusion of viscous suspensions with suitable rheological properties, which will be discussed in more detail in Chapter 2.5.5. Furthermore, pastes usually contain binders and organic solvents to support the structure in the desired shape after other layers are deposited on the top. Freeze-form extrusion fabrication (FEF) is similar to robocasting, but each layer solidifies by freezing the deposited layers to maintain the shape. The resolution of these techniques is ruled by the nozzle diameters, printing velocity, layer height, and the rheological properties of the feeding material [154].

3D printing can also combine different shaping techniques to generate even more complex structures [164]. Direct ink writing technologies have been recently combined with foaming techniques to produce a material with hierarchical porous structures. This results in a combination of porosities in the millimeter and micrometer range, given by the printing structure, and bubble size, respectively [165]. This allows for control of the pore sizes and density depending on the preparation process for polymer, metal, or ceramic materials for a variety of applications such as lightweight structural components, thermal insulation, tissue scaffolds, catalyst supports, and electrodes [166, 167]. Here, gas is incorporated into the suspension either by foaming agents, a chemical reaction, or solvent removal. Thereafter, the porous suspension is extruded through a nozzle into the desired geometry.

However, if the gas-liquid interface is not well stabilized, bubble collapse will occur because of drainage (creaming), coalescence (film rupture), and/or Ostwald ripening during or after printing. Minas et. al. [168] produced alumina samples with a hierarchical porous structure by combining DIW with emulsion/foam templating (Figure 2.10 - a), where η-octane bubbles were stabilized with surface active alumina particles in solution. They observed minimal loss of mechanical properties between printed samples with dense or porous filaments. Comparably, Muth et. al. [169] also printed alumina samples with a hierarchical porous structure, but they stabilized air bubbles with partially hydrophobized alumina particles (Figure 2.10 – b). They produced hexagonal and triangular honeycomb structures with low density (approx. 6%) after sintering and high elastic modulus of approx. 1 GPa.

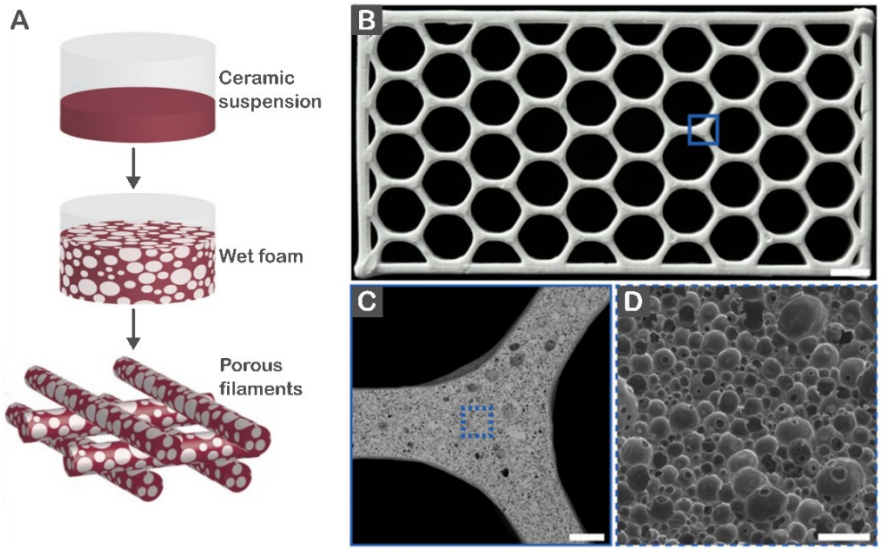

Figure 2.10 – “A” shows an illustration of a direct foaming process to produce cylindrical-shaped samples as well as customized 3D printed shapes. “B”, “C” and “D” shows printed alumina samples with hierarchical porous structure, whereas alumina particles were partially hydrophobized to stabilize bubbles in the foam (scale bar: B 5 mm; C 500 mm; D 100 μm). Adapted from [168, 169] with permission from John Wiley and Sons number 5265330165023 and from PNAS, respectively.

Another approach that has become interesting for 3D printing is the incorporation of cells into the ink to generate bioactive customized materials. This strategy is gaining importance in the fields of medical applications for organ implants, tissue engineering, bone replacement and more recently for bioprocessing [155, 170].

2.5 3D bioprinting

Increasing studies on the development of new hydrogel compositions and crosslinking strategies opened a new door for 3D printing processing methods [155, 171]. 3D bioprinting is an additive manufacturing process where biomaterials such as cells and growth factors are combined into the printing material to create a bioactive structure. This technique is mostly used to produce living functional tissues for medical applications [172, 173], such as bioactive porous material for tissue engineering [174, 175] and artificial organs [176, 177], but recently printing microorganisms into a porous structure is getting attention in the field of bioprocessing as well [178-180]. 3D bioprinting utilizes bioink as a starting material, which is a suspension composed of support material and living cells and builds 3D constructs in a layer-by-layer pattern. The challenges in developing bioinks include designing materials that can be processed with current printing techniques at desired resolutions, high biocompatibility to maintain cell viability during and after processing and providing the appropriate cellular environment to guide desired cell behavior and proliferation [170, 181-184]. Balancing printability with cell viability and function has been challenging as several methods are detrimental for cells. Based on this, bioprinting mostly uses liquid-based and paste-based printing systems such as inkjet printing, laser assisted printing, stereolithography printing, and robocasting (Figure 2.11) and a comparison of the different printing parameters of these techniques can be observed in Table 2.2. Moreover, these techniques had to be adapted for bioprinting.

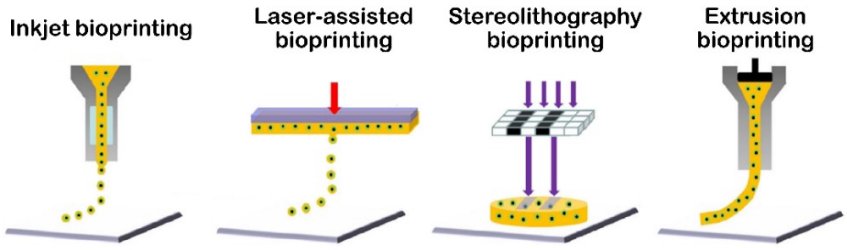

Figure 2.11 – Illustration of different 3D bioprinting techniques. Adapted from [174] with permission from Springer Nature number 5265331115397.

Inkjet bioprinting

Inkjet bioprinting is similar to conventional 2D inkjet printing and was one of the first bioprinting methods developed. The inkjet bioprinter generates small droplets of bioink suspension by continuous inkjet printing (CIJ) or drop-on-demand printing (DOD). CIJ uses electrostatic forces or thermal or piezoelectric actuators. Droplets are generated by breaking surface tensions instead of applied pressure and assure high cell viability as well as high printing resolution. Nevertheless, just low-viscosity inks can be printed with this technique and it has a long printing time [90, 176, 186-188].

Table 2.2 – Overview of the different parameters and requirements of the four 3D bioprinting approaches. Adapted from [185] with permission from WHIOCE publishing PTE. LTD.

Parameters	Bioprinting approaches			
	Inkjet	Laser-assisted	Stereolithography	Micro extrusion
Material viscosity	3.5 - 12 mPa/s	1 - 300 mPa/s	No limitation	30 to > 6 x 107 mPa/s
Crosslinking strategy	Photocuring, chemical	Photocuring, chemical	Photocuring, chemical	Photocuring, thermal, chemical
Cell viability	>85%	>95%	>85%	40-80%
Cell density	Low	Medium	Medium	High
Printing speed	Fast	Moderate	Fast	Slow
Printing resolution	High	High	High	Medium
Cost of printer	Low	High	Low	Medium

Laser-assisted bioprinting

Laser-assisted bioprinting uses focused laser pulses to generate localized heating. This heat locally vaporizes a region in the absorbing layer and creates a vapor that promotes a suspended bioink to fall onto the substrate. It is a nozzle-free approach that allows a precise deposition of the material with high cell viability. However, the generation of larger and clinically relevant 3D constructs is hindered by this technique due to the long fabrication time and the generated heat can be detrimental to living cells [174, 176, 182, 189].

Stereolithography bioprinting

Stereolithography (SLA) bioprinting uses light to selectively crosslink bioinks in a layer-by-layer process, similar to standard SLA methods. The difference for SLA bioprinting is that instead of using UV photo-curable resins as starting material it uses visible-light-crosslinkable hydrogels such as polyethylene glycol diacrylate (PEG-DA) and gelatin methacrylate (GelMA), since UV light can be detrimental for cells. This technique can print materials with high cell viability and resolution, and low fabrication time but there is still a lack of materials that are suitable for this technique in bioprinting [174, 176, 189].

Extrusion bioprinting

Extrusion-based printing, such as robocasting, is the most widespread and affordable bioprinting method [174, 182, 189]. This technique prints hydrogels with high cell density by pneumatically or mechanically dispersing the ink through a nozzle into hydrogel filaments [184]. Mechanical dispersing is a piston-driven system and provides, on the one hand, a better control over bioink flow but, on the other hand, it can be harmful to the suspended cells due to possible membrane disruption caused by large pressure drops generated by this method. Thus, pneumatical-based systems are more suitable for bioprinting, where pressure is controlled by adjusting air pressure [190]. Even if extrusion bioprinting shows low resolution (> 100 µm), this technique has the advantage of short fabrication time, high cell density, and the possibility of printing a wide range of hydrogel as well as composite materials and even cell spheroids [171]. Bioinks for extrusion-based bioprinters usually require high viscosity to assure shape fidelity, which potentially causes nozzle clogging and the decrease of cell viability due to shear stress. In this technique, cell viability is influenced mainly by the printing pressure, which is dependent on ink viscosity as well as on nozzle size and shape [191].

To print living cells, both the support material and the crosslinking method must be compatible with cells. Bioinks are a formulation of cells suitable for processing by an automated biofabrication technology where both support material and crosslinking method must be compatible with cells [181, 192]. Besides biocompatibility, bioinks must demonstrate high printability to form 3D structures with good shape fidelity and integrity [171]. Ideally, printable materials should exhibit a solid-like behavior of the printed filaments, which should be strong enough to support the deposition of further layers. Furthermore, printed filaments should stack with each other without merging and gelation should occur after filament extrusion to avoid nozzle blocking [193]. Hence, to achieve a successful 3D bioprinting process, physical and physiological properties need to be carefully tuned to ensure both good printability and high cell viability [194].

2.5.1 Rheology of suspensions for extrusion 3D bioprinting

Rheology is the science of deformation and flow of materials and is a key factor in controlling the printability and shape fidelity of the suspensions and gels during 3D printing. Rheology is used to characterize particle-liquid systems and how their interaction with each other affects the suspensions' flow and deformation behavior. The flow of a suspension is influenced by particle/polymer concentration, shape, and size as well as by the nature and strength of interparticle/polymer forces [195]. For all flowing fluids, internal friction forces are generated by the constant movement of the molecules. Thus, by applying shear rate ($\dot{\gamma}$), a certain shear stress (τ) will be necessary to move the fluid. The

relationship between shear rate and shear stress is the viscosity (η) and it is defined as the quotient between shear stress and shear rate (Equation 2.2). Furthermore, the viscosity of a fluid depends on the intermolecular interactions and can be either constant with the increase of shear rate/shear stress (Newtonian fluid) or change with the increase of shear rate/shear stress (non-Newtonian fluid) [196].

$$\eta = \frac{\tau}{\dot{\gamma}} \qquad \text{Equation 2.2}$$

The term Newtonian fluid describes an ideal fluid behavior, such as water. The incorporation of molecules/particles into water results in interactions between the molecules/particles and these interactions can be altered by increasing or decreasing shear rate/stress describing a non-Newtonian fluid. Bioinks should behave as a shear thinning fluid, where a reduction of viscosity by increasing shear rate takes place due to the disintegration of agglomerates and molecule/particle orientation with the flow direction. Bioinks should also exhibit a Bingham behavior with a clear yield stress in which flow is only initiated above a certain level of stress. This behavior also describes a transition from an elastic-plastic deformation region. If a shear stress is applied below the yield stress, it does not irreversibly disturb the structure of the fluid, the fluid does not flow and describes the elastic region (viscoelastic properties). When the applied stress overcomes the yield stress, an irreversible distortion of the system takes place which results in flow initiation, describing the onset of the plastic deformation [181, 197-199].

In addition to the shear rate dependence, the flow behavior of suspensions is usually time-dependent as well. In this case, the viscosity changes with shearing time because particles and molecules require time to arrange [181, 200]. For the extrusion of bioinks, an instantaneous viscosity recovery after printing is desired to avoid deformation of the printed constructs. Moreover, understanding the material behavior after printing and crosslinking is essential to carry out the desired application. Suspensions usually have viscoelastic properties, where a part of the mixture has a solid-like behavior (G') and another part shows a liquid-like behavior (G''). The solid-like properties are described by the elastic modulus (G') and the liquid part by the viscous modulus (G') via oscillatory rheological tests. For instance, gel materials act as solid materials and show higher G' than G''. For 3D printing, the feedstock materials should have a solid-like behavior already previous to the crosslinking process to assure structural integrity of the printed filaments during and after the printing process. Furthermore, the G' of crosslinked materials should be significantly higher than the G' of not crosslinked systems [198, 201, 202].

2.5.2 Influence of extrusion bioprinting on cell viability

3D bioprinting materials consist of a pre-processing stage, where the geometry is generated in a computer-aided design program (CAD), a processing stage where the bioink is deposited to build the 3D construct, and a post-processing stage, where the crosslinking takes place. Both processing and post-processing stages can be detrimental to the cells due to shear stresses or crosslinking. Nevertheless, the crosslinking method can be adapted to assure a low cell death while shear stress is, to some extent, an unavoidable mechanical stress that cells undergo in all dispensing bioprinting techniques [203]. The processing stage in extrusion-based bioprinting involves the application of a pressure in a cartridge, which is connected to a nozzle with a smaller diameter. The necessary pressure to be applied depends on suspension viscosity and nozzle size, as well as on printing velocity. Nevertheless, movement of the suspension inside the cartridge and through the nozzle results in internal shear stresses and can cause shear-induced cell disruption and death. During the printing process, a velocity gradient profile (u) is formed with lower velocities on the nozzle walls due to friction (Figure 2.12). Hence, a shear stress contrary to the flow movement takes place as a consequence of friction of the suspension with the nozzle wall and a shear stress (τ) gradient decreasing from the nozzle wall into the middle of the nozzle can be observed. The cells which are near to the wall are going to suffer a higher shearing than those in the middle of the nozzle and this can result in cell death. By decreasing nozzle diameter, a higher number of cells are influenced by the shearing with the nozzle wall and hence a decreasing nozzle diameter can be detrimental for the cells. Furthermore, the presence of nanoparticles in hydrogel nanocomposites results in higher viscosity and consequently higher printing pressures combined with internal friction between cells and nanoparticles in hydrogels nanocomposites, which can also be detrimental for the cells [203-205].

Nair et al. [206] analyzed the influence of nozzle diameter (150, 250, and 400 μm) and printing pressure (35, 70, 135, and 275 kPa) on eukaryotic cell viability. For that, they prepared 1.5 wt. % suspensions with rat adrenal medulla endothelial (RAMEC) cells and measured cell viability as well as a percentage of injured cells. They observed a minimal decrease in cell viability by decreasing nozzle diameter although an increment in injured cells was observed. Nevertheless, increasing pressure from 35 to 135 and 275 kPa reduced cell viability from 80% to 60% and 50%, respectively, while no influence was observed between 35 and 70 kPa for all nozzle sizes. Li et al. [207] analyzed the effect of conical and cylindrical nozzles on flow rate and Schwann and 3T3 fibroblast cell damage. They concluded that the flow rate in conical nozzles is higher than in cylindrical nozzles and that lower printing pressures are necessary using conical nozzles to achieve the same

flow rate as cylindrical nozzles. Consequently, lower cell damage is observed using conical nozzles.

Likewise, Billiet et al. [208] analyzed the influence of cylindrical and conical nozzles on the viability of hepatocarcinoma cells (HepG2) immobilized in gelatin methacrylamide during bioprinting with nozzle diameters of 300 µm. With pressures up to 2 bar, a 15% higher cell viability was observed using conical nozzles in comparison to cylindrical ones. However, for pressures of 3 – 5 bar no difference in cell viability could be observed between both nozzles' geometries. Thus, they performed a finite element simulation to understand the shear stress profile in both nozzles. Higher shear stresses were measured in the conical nozzle although the shear stress built-up was only observed close to the fluid outlet (<1 mm), limiting the passage time for this region. Conversely, cylindrical nozzles resulted in lower peak shear stresses but for a longer passage length (>16 mm). Consequently, the magnitude of stress and the stress exposure time affect cell viability.

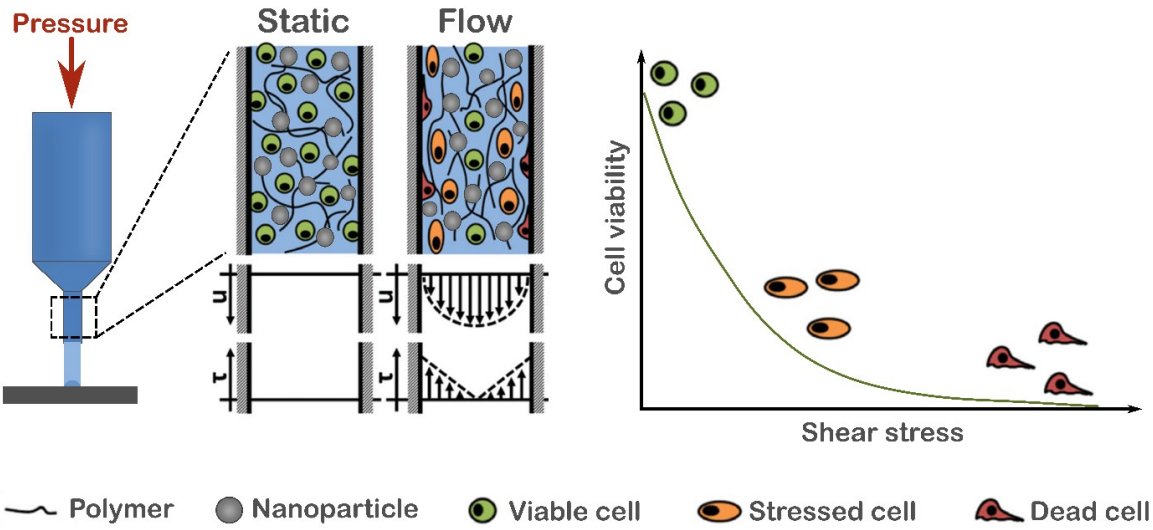

Figure 2.12 – Feedstock velocity profile (μ) and resultant shear stress (τ) inside the nozzle during printing and the influence of the shear stress on cell viability. Adapted from [203, 204] with permission from John Wiley and Sons number 5265340684051 and from Elsevier number 5265340512370, respectively.

Nevertheless, distinct cell types may differ in their sensitivity and response toward shear stress, and consequently cell viability values differ as well [209, 210]. Yet, the exact effects of shearing during 3D printing have not been studied in detail for microorganisms. Incorporating microorganisms into bioprinting is a field that just recently has got attention and the widely used microbeads started now to be customized into complex porous structures in order to increase the biotransformation rate. Experiments correlating shear

stress and bacterial or yeast viability have been performed in 2D environments or for microfluidic devices but the translation of these experiments into the context of 3D printing is controversial [211].

Alginate hydrogels got attention as support materials for 3D bioprinting with microorganisms due to the straightforward and biocompatible crosslinking. Lehner et al. [179] printed a mixture of alginate and red fluorescent protein (RFP) producing bacteria *E. coli*, in specific three-dimensional patterns and crosslinked the structure with calcium chloride. They observed a reduction of approx. 50% on bacterial viability after printing but a change of color stemming from the red fluorescent protein RFP could be observed on the printed material, indicating cells were viable and metabolically active to produce RFP protein. Two years later, Trampe et al. [180] published a study on the development of an alginate/methylcellulose bioink with luminescent O_2-sensing styrene maleic anhydride copolymer (PSMA) nanoparticles. This study aimed for ratiometric imaging of O_2 distribution on 3D-printed hydrogel scaffolds and to improve understanding of embedded microalgae metabolic activity. Furthermore, Freyman et al. [212] have studied the influence of carbon black on an alginate/cellulose bioink containing living bacteria *S. oneidensis*. By the addition of carbon black, they created a living conductive anode for microbial fuel cells (MFC) and the 3D-printed anode showed a charge transfer of approx. 2.5 times higher than the solid anode due to easier diffusion. Additionally, they observed that bacteria could grow in the hydrogel structure and higher current could be achieved after five cycles of amperometric current-time measurements. However, all these strategies using alginate as support material have not shown high printability and shape fidelity. Later on, Wei et al. [213] showed a nanocomposite printing ink based on 2,2,6,6-tetramethylpiperidinyl-1-oxyl (TEMPO)-oxidized bacterial cellulose (TOBC), sodium alginate (SA) and laponite nanoclay (Xls) with the embedded protein BSA. By incorporating the nanoclay, they could increase printability while structural stability also increased, reducing sample swelling and dissolution in physiological media, as well.

2.6 References

1. Singh, R., *Chapter 3 - Hybrid Membrane Systems – Applications and Case Studies*, in *Membrane Technology and Engineering for Water Purification (Second Edition)*, R. Singh, Editor. 2015, Butterworth-Heinemann: Oxford. p. 179-281.
2. Bhatia, S., *History, scope and development of biotechnology*, in *Introduction to Pharmaceutical Biotechnology, Volume 1*. 2018, IOP Publishing. p. 1-1-1-61.
3. Nixdorff, K., J. Brauburger, and D. Hahlbohm, *The Biotechnology Revolution: The Science and Applications*, in *Verification of the Biological and Toxin Weapons*

Convention, M.R. Dando, G.S. Pearson, and T. Toth, Editors. 2000, Springer Netherlands: Dordrecht. p. 77-124.

4. Rosa, S.S., et al., *mRNA vaccines manufacturing: Challenges and bottlenecks.* Vaccine, 2021. 39(16): p. 2190-2200.
5. Syldatk, C., et al., *Mikrobielle Prozesse*, in *Bioprozesstechnik*, H. Chmiel, Editor. 2011, Spektrum Akademischer Verlag: Heidelberg. p. 477-505.
6. Baeshen, N.A., et al., *Cell factories for insulin production.* Microbial Cell Factories, 2014. 13(1): p. 141.
7. Dixit, R., et al., *Bioremediation of Heavy Metals from Soil and Aquatic Environment: An Overview of Principles and Criteria of Fundamental Processes.* Sustainability, 2015. 7(2): p. 2189-2212.
8. Sanz, J.L. and T. Köchling, *Molecular biology techniques used in wastewater treatment: An overview.* Process Biochemistry, 2007. 42(2): p. 119-133.
9. Majidian, P., et al., *Metabolic engineering of microorganisms for biofuel production.* Renewable and Sustainable Energy Reviews, 2018. 82: p. 3863-3885.
10. Chmiel, H., *Bioreaktoren*, in *Bioprozesstechnik*, H. Chmiel, Editor. 2011, Spektrum Akademischer Verlag: Heidelberg. p. 197-236.
11. Hubbuch, J. and M.-R. Kula, *Isolation and Purification of Biotechnological Products.* 2007. 32(2): p. 99-127.
12. Antecka, A., et al., *Comparison of downstream processing methods in purification of highly active laccase.* Bioprocess and Biosystems Engineering, 2019. 42(10): p. 1635-1645.
13. Böttcher, H., et al., *Biocers: ceramics with incorporated microorganisms for biocatalytic, biosorptive and functional materials development.* Journal of Materials Chemistry, 2004. 14(14): p. 2176-2188.
14. Park, J.K. and H.N. Chang, *Microencapsulation of microbial cells.* Biotechnology Advances, 2000. 18(4): p. 303-319.
15. Chang, T.M.S., F.C. MacIntosh, and S.G. Mason, *SEMIPERMEABLE AQUEOUS MICROCAPSULES: I. PREPARATION AND PROPERTIES.* Canadian Journal of Physiology and Pharmacology, 1966. 44(1): p. 115-128.
16. Ge, X., L. Yang, and J. Xu, *Cell Immobilization: Fundamentals, Technologies, and Applications*, in *Industrial Biotechnology*. 2017. p. 205-235.
17. Gungormusler-Yilmaz, M., et al., *Cell immobilization for microbial production of 1,3-propanediol.* Critical Reviews in Biotechnology, 2016. 36(3): p. 482-494.
18. Silva, A.C., et al., *Cell Immobilization for the Production of Viral Vaccines*, in *Animal Cell Culture*, M. Al-Rubeai, Editor. 2015, Springer International Publishing: Cham. p. 541-563.

19. Wu, S.-C., et al., *The feasibility of a novel bioreactor for vaccine production of classical swine fever virus.* Vaccine, 2013. 31(6): p. 867-872.
20. Nedovic, V., et al., *An overview of encapsulation technologies for food applications.* Procedia Food Science, 2011. 1: p. 1806-1815.
21. Kulkarni, P., et al., *Cell Immobilization Strategies for Tissue Engineering: Recent Trends and Future Perspectives*, in *Immobilization Strategies : Biomedical, Bioengineering and Environmental Applications*, A. Tripathi and J.S. Melo, Editors. 2021, Springer Singapore: Singapore. p. 85-139.
22. Nemati, M. and C. Webb, *2.24 - Immobilized Cell Bioreactors*, in *Comprehensive Biotechnology (Second Edition)*, M. Moo-Young, Editor. 2011, Academic Press: Burlington. p. 331-346.
23. Bouabidi, Z.B., M.H. El-Naas, and Z. Zhang, *Immobilization of microbial cells for the biotreatment of wastewater: A review.* Environmental Chemistry Letters, 2019. 17(1): p. 241-257.
24. Zhu, Y., *Chapter 14 - Immobilized Cell Fermentation for Production of Chemicals and Fuels*, in *Bioprocessing for Value-Added Products from Renewable Resources*, S.-T. Yang, Editor. 2007, Elsevier: Amsterdam. p. 373-396.
25. Willaert, R., *Cell immobilization and its applications in biotechnology: Current trends and future prospects*. 2007. p. 289-362.
26. Vemmer, M. and A.V. Patel, *Review of encapsulation methods suitable for microbial biological control agents.* Biological Control, 2013. 67(3): p. 380-389.
27. Kumar, G., et al., *Recent insights into the cell immobilization technology applied for dark fermentative hydrogen production.* Bioresource Technology, 2016. 219: p. 725-737.
28. Jahnz, U., et al., *New Matrices and Bioencapsulation Processes*, in *Engineering and Manufacturing for Biotechnology*, M. Hofman and P. Thonart, Editors. 2002, Springer Netherlands: Dordrecht. p. 293-307.
29. Dias, D.R., et al., *Encapsulation as a tool for bioprocessing of functional foods.* Current Opinion in Food Science, 2017. 13: p. 31-37.
30. Mahinroosta, M., et al., *Hydrogels as intelligent materials: A brief review of synthesis, properties and applications.* Materials Today Chemistry, 2018. 8: p. 42-55.
31. Ahmed, E.M., *Hydrogel: Preparation, characterization, and applications: A review.* Journal of Advanced Research, 2015. 6(2): p. 105-121.
32. Park, M., D. Lee, and J. Hyun, *Nanocellulose-alginate hydrogel for cell encapsulation.* Carbohydrate Polymers, 2015. 116: p. 223-228.

33. He, Y., et al., *Encapsulation and characterization of slow-release microbial fertilizer from the composites of bentonite and alginate.* Applied Clay Science, 2015. 109-110: p. 68-75.
34. Mondal, S., S. Das, and A.K. Nandi, *A review on recent advances in polymer and peptide hydrogels.* Soft Matter, 2020. 16(6): p. 1404-1454.
35. Erol, O., et al., *Transformer Hydrogels: A Review.* Advanced Materials Technologies, 2019. 4(4): p. 1900043.
36. Henao, E., et al., *Polyelectrolyte Complexation versus Ionotropic Gelation for Chitosan-Based Hydrogels with Carboxymethylcellulose, Carboxymethyl Starch, and Alginic Acid.* International Journal of Chemical Engineering, 2018. 2018: p. 3137167.
37. Jen, A.C., M.C. Wake, and A.G. Mikos, *Review: Hydrogels for cell immobilization.* Biotechnology and Bioengineering, 1996. 50(4): p. 357-364.
38. Ching, S.H., N. Bansal, and B. Bhandari, *Alginate gel particles–A review of production techniques and physical properties.* Critical Reviews in Food Science and Nutrition, 2017. 57(6): p. 1133-1152.
39. Pawar, S.N. and K.J. Edgar, *Alginate derivatization: A review of chemistry, properties and applications.* Biomaterials, 2012. 33(11): p. 3279-3305.
40. Szekalska, M., et al., *Alginate: Current Use and Future Perspectives in Pharmaceutical and Biomedical Applications.* International Journal of Polymer Science, 2016. 2016: p. 7697031.
41. Andersen, T., P. Auk-Emblem, and M. Dornish, *3D Cell Culture in Alginate Hydrogels.* Microarrays, 2015. 4(2): p. 133-161.
42. Lee, K.Y. and D.J. Mooney, *Alginate: Properties and biomedical applications.* Progress in Polymer Science, 2012. 37(1): p. 106-126.
43. Kong, H.J., M.K. Smith, and D.J. Mooney, *Designing alginate hydrogels to maintain viability of immobilized cells.* Biomaterials, 2003. 24(22): p. 4023-4029.
44. Leong, J.-Y., et al., *Advances in fabricating spherical alginate hydrogels with controlled particle designs by ionotropic gelation as encapsulation systems.* Particuology, 2016. 24: p. 44-60.
45. Growney Kalaf, E.A., et al., *Characterization of slow-gelling alginate hydrogels for intervertebral disc tissue-engineering applications.* Materials Science and Engineering: C, 2016. 63: p. 198-210.
46. Teli, M.D. and J. Sheikh, *Extraction of chitosan from shrimp shells waste and application in antibacterial finishing of bamboo rayon.* International Journal of Biological Macromolecules, 2012. 50(5): p. 1195-1200.

47. Croisier, F. and C. Jérôme, *Chitosan-based biomaterials for tissue engineering.* European Polymer Journal, 2013. 49(4): p. 780-792.
48. Ahmadi, F., et al., *Chitosan based hydrogels: characteristics and pharmaceutical applications.* Research in pharmaceutical sciences, 2015. 10(1): p. 1-16.
49. Bellich, B., et al., *"The Good, the Bad and the Ugly" of Chitosans.* Marine Drugs, 2016. 14(5): p. 99.
50. Pati, F., B. Adhikari, and S. Dhara, *Development of chitosan–tripolyphosphate fibers through pH dependent ionotropic gelation.* Carbohydrate Research, 2011. 346(16): p. 2582-2588.
51. Muzzarelli, R.A.A., *Genipin-crosslinked chitosan hydrogels as biomedical and pharmaceutical aids.* Carbohydrate Polymers, 2009. 77(1): p. 1-9.
52. Kil'deeva, N.R., et al., *Mechanism of the reaction of glutaraldehyde with chitosan.* Bioorg Khim, 2009. 35(3): p. 397-407.
53. Elgadir, M.A., et al., *Impact of chitosan composites and chitosan nanoparticle composites on various drug delivery systems: A review.* Journal of Food and Drug Analysis, 2015. 23(4): p. 619-629.
54. Balamurugan, M., S. Rajesh, and E. Manogaran, *'Genipin' – The Natural Water Soluble Cross-linking Agent and Its Importance in the Modified Drug Delivery Systems: An Overview.* Current Drug Delivery, 2014. 11(1): p. 139-145.
55. Liu, B.-S. and T.-B. Huang, *Nanocomposites of Genipin-Crosslinked Chitosan/Silver Nanoparticles - Structural Reinforcement and Antimicrobial Properties.* Macromolecular Bioscience, 2008. 8(10): p. 932-941.
56. Vukajlovic, D., et al., *Chitosan based polymer/bioglass composites for tissue engineering applications.* Materials Science and Engineering: C, 2019. 96: p. 955-967.
57. Gao, L., et al., *Effects of genipin cross-linking of chitosan hydrogels on cellular adhesion and viability.* Colloids and Surfaces B: Biointerfaces, 2014. 117: p. 398-405.
58. Dimida, S., et al., *Genipin-cross-linked chitosan-based hydrogels: Reaction kinetics and structure-related characteristics.* Journal of Applied Polymer Science, 2015. 132(28).
59. Butler, M.F., Y.-F. Ng, and P.D.A. Pudney, *Mechanism and kinetics of the crosslinking reaction between biopolymers containing primary amine groups and genipin.* Journal of Polymer Science Part A: Polymer Chemistry, 2003. 41(24): p. 3941-3953.

60. Delmar, K. and H. Bianco-Peled, *The dramatic effect of small pH changes on the properties of chitosan hydrogels crosslinked with genipin.* Carbohydrate Polymers, 2015. 127: p. 28-37.
61. Banerjee, A. and S. Ganguly, *Alginate–chitosan composite hydrogel film with macrovoids in the inner layer for biomedical applications.* Journal of Applied Polymer Science, 2019. 136(22): p. 47599.
62. Baysal, K., et al., *Chitosan/alginate crosslinked hydrogels: Preparation, characterization and application for cell growth purposes.* International Journal of Biological Macromolecules, 2013. 59: p. 342-348.
63. Wang, G., X. Wang, and L. Huang, *Feasibility of chitosan-alginate (Chi-Alg) hydrogel used as scaffold for neural tissue engineering: a pilot study in vitro.* Biotechnology & Biotechnological Equipment, 2017. 31(4): p. 766-773.
64. Khong, T.T., et al., *Gelling Concept Combining Chitosan and Alginate—Proof of Principle.* Biomacromolecules, 2013. 14(8): p. 2765-2771.
65. Apte, G., et al., *Effect of Different Crosslinking Strategies on Physical Properties and Biocompatibility of Freestanding Multilayer Films Made of Alginate and Chitosan.* Macromolecular Bioscience, 2019. 19(11): p. 1900181.
66. Xu, Y., et al., *Preparation of dual crosslinked alginate–chitosan blend gel beads and in vitro controlled release in oral site-specific drug delivery system.* International Journal of Pharmaceutics, 2007. 336(2): p. 329-337.
67. Meka, V.S., et al., *A comprehensive review on polyelectrolyte complexes.* Drug Discovery Today, 2017. 22(11): p. 1697-1706.
68. Lawrie, G., et al., *Interactions between Alginate and Chitosan Biopolymers Characterized Using FTIR and XPS.* Biomacromolecules, 2007. 8(8): p. 2533-2541.
69. Sæther, H.V., et al., *Polyelectrolyte complex formation using alginate and chitosan.* Carbohydrate Polymers, 2008. 74(4): p. 813-821.
70. Colosi, C., et al., *Rapid prototyping of chitosan-coated alginate scaffolds through the use of a 3D fiber deposition technique.* Journal of Materials Chemistry B, 2014. 2(39): p. 6779-6791.
71. Sharma, G., et al., *Applications of nanocomposite hydrogels for biomedical engineering and environmental protection.* Environmental Chemistry Letters, 2018. 16(1): p. 113-146.
72. Zhao, Z., et al., *Bioinspired Nanocomposite Hydrogels with Highly Ordered Structures.* Advanced Materials, 2017. 29(45): p. 1703045.
73. Li, L., et al., *A Nanostructured Conductive Hydrogels-Based Biosensor Platform for Human Metabolite Detection.* Nano Letters, 2015. 15(2): p. 1146-1151.

74. Das, R. and C. Bhattacharjee, *Hydrogel nanocomposite for controlled drug release*, in *Applications of Nanocomposite Materials in Drug Delivery*, Inamuddin, A.M. Asiri, and A. Mohammad, Editors. 2018, Woodhead Publishing. p. 575-588.
75. Zhao, H., et al., *Nanocomposite hydrogels for tissue engineering applications.* Nanoscale, 2020. 12(28): p. 14976-14995.
76. Carrow, J.K. and A.K. Gaharwar, *Bioinspired Polymeric Nanocomposites for Regenerative Medicine.* Macromolecular Chemistry and Physics, 2015. 216(3): p. 248-264.
77. Kokabi, M., M. Sirousazar, and Z.M. Hassan, *PVA–clay nanocomposite hydrogels for wound dressing.* European Polymer Journal, 2007. 43(3): p. 773-781.
78. Rafieian, S., et al., *A review on nanocomposite hydrogels and their biomedical applications.* Science and Engineering of Composite Materials, 2019. 26(1): p. 154.
79. Zhao, F., et al., *Composites of Polymer Hydrogels and Nanoparticulate Systems for Biomedical and Pharmaceutical Applications.* Nanomaterials (Basel, Switzerland), 2015. 5(4): p. 2054-2130.
80. Wahid, F., et al., *Nanocomposite hydrogels as multifunctional systems for biomedical applications: Current state and perspectives.* Composites Part B: Engineering, 2020. 200: p. 108208.
81. Wei, P., et al., *Conductive Self-Healing Nanocomposite Hydrogel Skin Sensors with Antifreezing and Thermoresponsive Properties.* ACS Applied Materials & Interfaces, 2020. 12(2): p. 3068-3079.
82. Li, Y., et al., *Tough and conductive nanocomposite hydrogels for human motion monitoring.* Polymer Testing, 2019. 75: p. 38-47.
83. Filippi, M., et al., *Magnetic nanocomposite hydrogels and static magnetic field stimulate the osteoblastic and vasculogenic profile of adipose-derived cells.* Biomaterials, 2019. 223: p. 119468.
84. Bardajee, G.R., et al., *Multi-stimuli responsive nanogel/hydrogel nanocomposites based on κ-carrageenan for prolonged release of levodopa as model drug.* International Journal of Biological Macromolecules, 2020. 153: p. 180-189.
85. Deen, G.R. and V. Chua, *Synthesis and Properties of New "Stimuli" Responsive Nanocomposite Hydrogels Containing Silver Nanoparticles.* Gels (Basel, Switzerland), 2015. 1(1): p. 117-134.
86. Motealleh, A., et al., *3D bioprinting of triphasic nanocomposite hydrogels and scaffolds for cell adhesion and migration.* Biofabrication, 2019. 11(3): p. 035022.
87. Kumar-Krishnan, S., et al., *Chitosan/silver nanocomposites: Synergistic antibacterial action of silver nanoparticles and silver ions.* European Polymer Journal, 2015. 67: p. 242-251.

88. Cha, G.D., et al., *Materials engineering, processing, and device application of hydrogel nanocomposites.* Nanoscale, 2020. 12(19): p. 10456-10473.
89. Rotbaum, Y., et al., *Mechanical reinforcement of methylcellulose hydrogels by rigid particle additives.* Mechanics of Materials, 2019. 132: p. 57-65.
90. Martín, M.J., et al., *Microencapsulation of bacteria: A review of different technologies and their impact on the probiotic effects.* Innovative Food Science & Emerging Technologies, 2015. 27: p. 15-25.
91. Blondeau, M. and T. Coradin, *Living materials from sol–gel chemistry: current challenges and perspectives.* Journal of Materials Chemistry, 2012. 22(42): p. 22335-22343.
92. Iwanaga, S., K. Arai, and M. Nakamura, *Chapter 4 - Inkjet Bioprinting*, in *Essentials of 3D Biofabrication and Translation*, A. Atala and J.J. Yoo, Editors. 2015, Academic Press: Boston. p. 61-79.
93. Ghasemzadeh, K., A. Basile, and A. Iulianelli, *Progress in Modeling of Silica-Based Membranes and Membrane Reactors for Hydrogen Production and Purification.* ChemEngineering, 2019. 3(1): p. 2.
94. Zalevsky, Z. and I. Abdulhalim, *Physical Background*, in *Integrated Nanophotonic Devices*, Z. Zalevsky and I. Abdulhalim, Editors. 2010, William Andrew Publishing: Oxford. p. 1-57.
95. Thompson, M.T., *Review of Diode Physics and the Ideal (and Later, Nonideal) Diode*, in *Intuitive Analog Circuit Design (Second Edition)*, M.T. Thompson, Editor. 2014, Newnes: Boston. p. 53-86.
96. Kärger, J. and R. Valiullin, *Mass transfer in mesoporous materials: the benefit of microscopic diffusion measurement.* Chemical Society Reviews, 2013. 42(9): p. 4172-4197.
97. Burganos, V.N., *Modeling and Simulation of Membrane Structure and Transport Properties*, in *Comprehensive Membrane Science and Engineering*, E. Drioli and L. Giorno, Editors. 2010, Elsevier: Oxford. p. 29-74.
98. Myshlyavtsev, A.V., *Surface Diffusion Modelling: Transfer Matrix Approach*, in *Studies in Surface Science and Catalysis*, A. Guerrero-Ruiz and I. Rodríguez-Ramos, Editors. 2001, Elsevier. p. 173-180.
99. Singh, R., *Introduction to Membrane Technology*, in *Membrane Technology and Engineering for Water Purification (Second Edition)*, R. Singh, Editor. 2015, Butterworth-Heinemann: Oxford. p. 1-80.
100. Reinecke, S.A. and B.E. Sleep, Knudsen diffusion, gas permeability, and water content in an unconsolidated porous medium. Water Resources Research, 2002. 38(12): p. 16-1-16-15.

101. Hattori, Y., K. Kaneko, and T. Ohba, 5.02 - Adsorption Properties, in Comprehensive Inorganic Chemistry II (Second Edition), J. Reedijk and K. Poeppelmeier, Editors. 2013, Elsevier: Amsterdam. p. 25-44.
102. Marion, A., *Physical Transport Processes in Ecology: Advection, Diffusion, and Dispersion*, in *Encyclopedia of Ecology*, S.E. Jørgensen and B.D. Fath, Editors. 2008, Academic Press: Oxford. p. 2739-2744.
103. Murphy, B.L., *Chemical Partitioning and Transport in the Environment*, in *Introduction to Environmental Forensics (Third Edition)*, B.L. Murphy and R.D. Morrison, Editors. 2015, Academic Press: San Diego. p. 165-197.
104. Cebeci, T., *Introduction*, in *Analysis of Turbulent Flows with Computer Programs (Third Edition)*, T. Cebeci, Editor. 2013, Butterworth-Heinemann: Oxford. p. 1-32.
105. Kundu, P.K., I.M. Cohen, and D.R. Dowling, *Laminar Flow*, in *Fluid Mechanics*, P.K. Kundu, I.M. Cohen, and D.R. Dowling, Editors. 2016, Academic Press: Boston. p. 409-467.
106. Lee, S.J., H. Kim, and S. Ahn, *Water transport in porous hydrogel structures analogous to leaf mesophyll cells.* Microfluidics and Nanofluidics, 2015. 18(5): p. 775-784.
107. Li, X.a.S., T., *Mass Transport in Polymer Gels*, in *Physics of Polymer Gels*. 2020. p. 137-150.
108. Simpliciano, C., Clark, L. , Asi, B. , Chu, N. , Mercado, M. , Diaz, S. , Goedert, M. and Mobed-Miremadi, M., *Cross-Linked Alginate Film Pore Size Determination Using Atomic Force Microscopy and Validation Using Diffusivity Determinations.* Journal of Surface Engineered Materials and Advanced Technology, 2013. 3: p. 1-12.
109. Hussain, A., et al., *Operational parameters and their influence on particle-side mass transfer resistance in a packed bed bioreactor.* AMB Express, 2015. 5(1): p. 51.
110. Schuster, E., et al., *Microstructural, mechanical and mass transport properties of isotropic and capillary alginate gels.* Soft Matter, 2014. 10(2): p. 357-366.
111. Xing, R., et al., *Creation of Triple Hierarchical Micro-Meso-Macroporous N-doped Carbon Shells with Hollow Cores Toward the Electrocatalytic Oxygen Reduction Reaction.* Nano-Micro Letters, 2017. 10(1): p. 3.
112. Schneider, D., et al., *Transport properties of hierarchical micro–mesoporous materials.* Chemical Society Reviews, 2016. 45(12): p. 3439-3467.
113. Isaacs, M.A., et al., *Unravelling mass transport in hierarchically porous catalysts.* Journal of Materials Chemistry A, 2019. 7(19): p. 11814-11825.

114. Armstrong, J.P.K., et al., *3D Bioprinting Using a Templated Porous Bioink.* Advanced Healthcare Materials, 2016. 5(14): p. 1724-1730.
115. Kessel, B., et al., *3D Bioprinting of Architected Hydrogels from Entangled Microstrands.* bioRxiv, 2019: p. 2019.12.13.870220.
116. Ruiz-Cantu, L., et al., *Multi-material 3D bioprinting of porous constructs for cartilage regeneration.* Materials Science and Engineering: C, 2020. 109: p.
117. Bao, G., et al., *Triggered micropore-forming bioprinting of porous viscoelastic hydrogels.* Materials Horizons, 2020. 7(9): p. 2336-2347.
118. Shao, L., et al., *bioink-enabled 3D bioprinting of mesoscale pore networks.* Bio-Design and Manufacturing, 2020. 3(1): p. 30-39.
119. Omatete, O.O., M.A. Janney, and S.D. Nunn, *Gelcasting: From laboratory development toward industrial production.* Journal of the European Ceramic Society, 1997. 17(2): p. 407-413.
120. Pollinger, J.P., Y.E. Khalfalla, and K.Y. Benyounis, *Gel Casting*, in *Reference Module in Materials Science and Materials Engineering*. 2016, Elsevier.
121. Young, A.C., et al., *Gelcasting of Alumina.* Journal of the American Ceramic Society, 1991. 74(3): p. 612-618.
122. Liu, P.S. and G.F. Chen, *Chapter Five - Fabricating Porous Ceramics*, in *Porous Materials*, P.S. Liu and G.F. Chen, Editors. 2014, Butterworth-Heinemann: Boston. p. 221-302.
123. Mallick, K.K. and J. Winnett, *6 - 3D bioceramic foams for bone tissue engineering*, in *Bone Substitute Biomaterials*, K. Mallick, Editor. 2014, Woodhead Publishing. p. 118-141.
124. Koppolu, B.p., et al., *Controlling chitosan-based encapsulation for protein and vaccine delivery.* Biomaterials, 2014. 35(14): p. 4382-4389.
125. Grenha, A., *Chitosan nanoparticles: a survey of preparation methods.* Journal of Drug Targeting, 2012. 20(4): p. 291-300.
126. Lam, D., et al., *Optimizing cell encapsulation condition in ECM-Collagen I hydrogels to support 3D neuronal cultures.* Journal of Neuroscience Methods, 2020. 329: p. 108460.
127. Thapa, R.K., K.L. Kiick, and M.O. Sullivan, *Encapsulation of collagen mimetic peptide-tethered vancomycin liposomes in collagen-based scaffolds for infection control in wounds.* Acta Biomaterialia, 2020. 103: p. 115-128.
128. Brandes, C., et al., *Gel casting of large area micro- and sub-micropatterned thin ceramic tapes.* Ceramics International, 2016. 42(4): p. 5036-5044.

129. Brandes, C., et al., *Gel Casting of Free-Shapeable Ceramic Membranes with Adjustable Pore Size for Ultra- and Microfiltration.* Journal of the American Ceramic Society, 2014. 97(5): p. 1393-1401.
130. Brandes, C., et al., *Aluminium acetate as alternative cross-linker for temperature controlled gel-casting and joining of ceramics.* Journal of the European Ceramic Society, 2016. 36(5): p. 1241-1251.
131. Pokhrel, A., et al., *Processing of Porous Ceramics by Direct Foaming: A Review.* J. Korean Ceram. Soc, 2013. 50(2): p. 93-0.
132. Studart, A.R., et al., *Processing Routes to Macroporous Ceramics: A Review.* Journal of the American Ceramic Society, 2006. 89(6): p. 1771-1789.
133. Mao, X., *Processing of ceramics foams*, in *Recent advances in porous ceramics*, U.M.B. Al-Naib, Editor. 2018, IntechOpen: London, United Kingdom. p. 31 - 47.
134. Murray, B.S., *Stabilization of bubbles and foams.* Current Opinion in Colloid & Interface Science, 2007. 12(4): p. 232-241.
135. Wang, J., A.V. Nguyen, and S. Farrokhpay, *A critical review of the growth, drainage and collapse of foams.* Advances in Colloid and Interface Science, 2016. 228: p. 55-70.
136. Barg, S., et al., *Cellular Ceramics by Direct Foaming of Emulsified Ceramic Powder Suspensions.* Journal of the American Ceramic Society, 2008. 91(9): p. 2823-2829.
137. Langevin, D., *Influence of interfacial rheology on foam and emulsion properties.* Advances in Colloid and Interface Science, 2000. 88(1): p. 209-222.
138. Carl, A., A. Bannuscher, and R. von Klitzing, *Particle Stabilized Aqueous Foams at Different Length Scales: Synergy between Silica Particles and Alkylamines.* Langmuir, 2015. 31(5): p. 1615-1622.
139. Binks, B.P. and R. Murakami, *Phase inversion of particle-stabilized materials from foams to dry water.* Nature Materials, 2006. 5(11): p. 865-869.
140. Dickinson, E., et al., *Factors Controlling the Formation and Stability of Air Bubbles Stabilized by Partially Hydrophobic Silica Nanoparticles.* Langmuir, 2004. 20(20): p. 8517-8525.
141. Cui, Z.G., et al., *Aqueous Foams Stabilized by in Situ Surface Activation of CaCO3 Nanoparticles via Adsorption of Anionic Surfactant.* Langmuir, 2010. 26(15): p. 12567-12574.
142. Tzoumaki, M.V., et al., *Aqueous foams stabilized by chitin nanocrystals.* Soft Matter, 2015. 11(31): p. 6245-6253.

143. Wege, H.A., et al., *Long-Term Stabilization of Foams and Emulsions with In-Situ Formed Microparticles from Hydrophobic Cellulose.* Langmuir, 2008. 24(17): p. 9245-9253.
144. Jin, H., et al., *Super stable foams stabilized by colloidal ethyl cellulose particles.* Soft Matter, 2012. 8(7): p. 2194-2205.
145. Pugh, R.J., *Particle-stabilized foams*, in *Bubble and Foam Chemistry*, R.J. Pugh, Editor. 2016, Cambridge University Press: Cambridge. p. 269-306.
146. Carl, A., J. Witte, and R. von Klitzing, *A look inside particle stabilized foams—particle structure and dynamics.* Journal of Physics D: Applied Physics, 2015. 48(43): p. 434003.
147. Tyowua, A.T. and B.P. Binks, *Growing a particle-stabilized aqueous foam.* Journal of Colloid and Interface Science, 2020. 561: p. 127-135.
148. Gonzenbach, U.T., et al., *Stabilization of Foams with Inorganic Colloidal Particles.* Langmuir, 2006. 22(26): p. 10983-10988.
149. Wijaya, W., et al., *Functional colloids from proteins and polysaccharides for food applications.* Trends in Food Science & Technology, 2017. 68: p. 56-69.
150. Petkova, B., et al., *Foamability of aqueous solutions: Role of surfactant type and concentration.* Advances in Colloid and Interface Science, 2020. 276: p. 102084.
151. Maestro, A., et al., *Foams stabilised by mixtures of nanoparticles and oppositely charged surfactants: relationship between bubble shrinkage and foam coarsening.* Soft Matter, 2014. 10(36): p. 6975-6983.
152. Maas, M., et al., *Towards the synthesis of hydroxyapatite/protein scaffolds with controlled porosities: Bulk and interfacial shear rheology of a hydroxyapatite suspension with protein additives.* Journal of Colloid and Interface Science, 2013. 407: p. 529-535.
153. Langevin, D., *Aqueous foams and foam films stabilised by surfactants. Gravity-free studies.* Comptes Rendus Mécanique, 2017. 345(1): p. 47-55.
154. Ngo, T.D., et al., *Additive manufacturing (3D printing): A review of materials, methods, applications and challenges.* Composites Part B: Engineering, 2018. 143: p. 172-196.
155. Lee, J.-Y., J. An, and C.K. Chua, *Fundamentals and applications of 3D printing for novel materials.* Applied Materials Today, 2017. 7: p. 120-133.
156. Provaggi, E. and D.M. Kalaskar, *2 - 3D printing families: Laser, powder, nozzle based techniques*, in *3D Printing in Medicine*, D.M. Kalaskar, Editor. 2017, Woodhead Publishing. p. 21-42.

157. Shirazi, S.F.S., et al., *A review on powder-based additive manufacturing for tissue engineering: selective laser sintering and inkjet 3D printing.* Science and Technology of Advanced Materials, 2015. 16(3): p. 033502.
158. Brunello, G., et al., *Powder-based 3D printing for bone tissue engineering.* Biotechnology Advances, 2016. 34(5): p. 740-753.
159. Guo, N. and M.C. Leu, *Additive manufacturing: technology, applications and research needs.* Frontiers of Mechanical Engineering, 2013. 8(3): p. 215-243.
160. Ligon, S.C., et al., *Polymers for 3D Printing and Customized Additive Manufacturing.* Chemical Reviews, 2017. 117(15): p. 10212-10290.
161. Chen, Z., et al., *3D printing of ceramics: A review.* Journal of the European Ceramic Society, 2019. 39(4): p. 661-687.
162. Feilden, E., et al., *Robocasting of structural ceramic parts with hydrogel inks.* Journal of the European Ceramic Society, 2016. 36(10): p. 2525-2533.
163. Peng, E., D. Zhang, and J. Ding, *Ceramic Robocasting: Recent Achievements, Potential, and Future Developments.* Advanced Materials, 2018. 30(47): p. 1802404.
164. Blanco, I., *The Use of Composite Materials in 3D Printing.* Journal of Composites Science, 2020. 4(2): p. 42.
165. Ren, B., et al., *Hierarchical cellular scaffolds fabricated via direct foam writing using gelled colloidal particle-stabilized foams as the ink.* Journal of the American Ceramic Society, 2019. 102(11): p. 6498-6506.
166. Liang, C., et al., *Light and Strong Hierarchical Porous SiC Foam for Efficient Electromagnetic Interference Shielding and Thermal Insulation at Elevated Temperatures.* ACS Applied Materials & Interfaces, 2017. 9(35): p. 29950-29957.
167. Chen, Q., P.-F. Cao, and R.C. Advincula, *Mechanically Robust, Ultraelastic Hierarchical Foam with Tunable Properties via 3D Printing.* Advanced Functional Materials, 2018. 28(21): p. 1800631.
168. Minas, C., et al., *3D Printing of Emulsions and Foams into Hierarchical Porous Ceramics.* Advanced Materials, 2016. 28(45): p. 9993-9999.
169. Muth, J.T., et al., *Architected cellular ceramics with tailored stiffness via direct foam writing.* Proceedings of the National Academy of Sciences, 2017. 114(8): p. 1832.
170. Correia Carreira, S., R. Begum, and A.W. Perriman, *3D Bioprinting: The Emergence of Programmable Biodesign.* Advanced Healthcare Materials, 2020. 9(15): p. 1900554.
171. Chimene, D., R. Kaunas, and A.K. Gaharwar, *Hydrogel Bioink Reinforcement for Additive Manufacturing: A Focused Review of Emerging Strategies.* Advanced Materials, 2020. 32(1): p. 1902026.

172. Tasoglu, S. and U. Demirci, *Bioprinting for stem cell research.* Trends Biotechnol., 2013. 31: p. 10.
173. Hsieh F-Y, L.H.H. and S. Hsu, *3D bioprinting of neural stem cell-laden thermoresponsive biodegradable polyurethane hydrogel and potential in central nervous system repair.* Biomaterials, 2015. 71: p. 48.
174. Tasnim, N., et al., *3D Bioprinting Stem Cell Derived Tissues.* Cellular and Molecular Bioengineering, 2018. 11(4): p. 219-240.
175. Markstedt K, M.A.T.I.M.A.H.H.D. and P. Gatenholm, *3D bioprinting human chondrocytes with nanocellulose–alginate bioink for cartilage tissue engineering applications.* Biomacromolecules, 2015. 16: p. 1489.
176. Matai, I., et al., *Progress in 3D bioprinting technology for tissue/organ regenerative engineering.* Biomaterials, 2020. 226: p. 119536.
177. Murphy, S.V. and A. Atala, *3D bioprinting of tissues and organs.* Nat. Biotechnol., 2014. 32: p. 773.
178. Shavandi, A. and E. Jalalvandi, *Biofabrication of Bacterial Constructs: New Three-Dimensional Biomaterials.* Bioengineering, 2019. 6(2): p. 44.
179. Lehner, B.A.E., D.T. Schmieden, and A.S. Meyer, *A Straightforward Approach for 3D Bacterial Printing.* ACS Synthetic Biology, 2017. 6(7): p. 1124-1130.
180. Trampe, E., et al., *Functionalized Bioink with Optical Sensor Nanoparticles for O2 Imaging in 3D-Bioprinted Constructs.* Advanced Functional Materials, 2018. 28(45): p. 1804411.
181. Hölzl, K., et al., *Bioink properties before, during and after 3D bioprinting.* Biofabrication, 2016. 8(3): p. 032002.
182. Gungor-Ozkerim, P.S., et al., *Bioinks for 3D bioprinting: an overview.* Biomaterials Science, 2018. 6(5): p. 915-946.
183. Dababneh, A.B. and I.T. Ozbolat, *Bioprinting technology: a current state-of-the-art review.* J. Manuf. Sci. Eng., 2014. 136.
184. Merceron, T.K. and S.V. Murphy, *Hydrogels for 3D Bioprinting Applications*, in *Essentials of 3D Biofabrication and Translation*, A. Atala and J.J. Yoo, Editors. 2015, Academic Press: Boston. p. 249-270.
185. Choudhury, D., S. Anand, and M.W. Naing, *The arrival of commercial bioprinters - Towards 3D bioprinting revolution!* Int J Bioprint, 2018. 4(2): p. 139.
186. Xu T, J.J.G.C.H.J.J. and T. Boland, *Inkjet printing of viable mammalian cells.* Biomaterials, 2005. 26: p. 93.
187. Calvert, P., *Inkjet printing for materials and devices.* Chem. Mater., 2001. 13: p. 3299.

188. Saunders, R.E. and B. Derby, *Inkjet printing biomaterials for tissue engineering: bioprinting.* Int. Mater. Rev., 2014. 59: p. 430.
189. Donderwinkel, I., J.C.M. van Hest, and N.R. Cameron, *Bio-inks for 3D bioprinting: recent advances and future prospects.* Polymer Chemistry, 2017. 8(31): p. 4451-4471.
190. Chen, D.X.B., *Extrusion Bioprinting of Scaffolds: An Introduction*, in *Extrusion Bioprinting of Scaffolds for Tissue Engineering Applications*. 2019, Springer International Publishing: Cham. p. 1-13.
191. Zhang, Z., et al., *Evaluation of bioink printability for bioprinting applications.* Applied Physics Reviews, 2018. 5(4): p. 041304.
192. Groll, J., et al., *A definition of bioinks and their distinction from biomaterial inks.* Biofabrication, 2018. 11(1): p. 013001.
193. Paxton, N., et al., *Proposal to assess printability of bioinks for extrusion-based bioprinting and evaluation of rheological properties governing bioprintability.* Biofabrication, 2017. 9(4): p. 044107.
194. Chimene, D., et al., *Advanced Bioinks for 3D Printing: A Materials Science Perspective.* Annals of Biomedical Engineering, 2016. 44(6): p. 2090-2102.
195. Moreno, R., *Rheology*, in *Encyclopedia of Materials: Science and Technology*, E.S. Ltd, Editor. 2001. p. 8192 - 8197.
196. Struble, L.J. and X. Ji, *Rheology*, in *Handbook of Analytical Techniques in Concrete Science and Technology*, V.S. Ramachandran and J.J. Beaudoin, Editors. 2001, William Andrew Publishing: Norwich, NY. p. 333-367.
197. Sanchez, L.C., et al., *Rheological approach for an additive manufacturing printer based on material extrusion.* The International Journal of Advanced Manufacturing Technology, 2019. 105(5): p. 2403-2414.
198. O'Connell, C., et al., *Characterizing Bioinks for Extrusion Bioprinting: Printability and Rheology*, in *3D Bioprinting: Principles and Protocols*, J.M. Crook, Editor. 2020, Springer US: New York, NY. p. 111-133.
199. Willson, K., et al., *Extrusion-Based Bioprinting: Current Standards and Relevancy for Human-Sized Tissue Fabrication*, in *3D Bioprinting: Principles and Protocols*, J.M. Crook, Editor. 2020, Springer US: New York, NY. p. 65-92.
200. Mewis, J. and N.J. Wagner, *Thixotropy.* Advances in Colloid and Interface Science, 2009. 147-148: p. 214-227.
201. Schaffner, M., et al., *3D printing of bacteria into functional complex materials.* 2017. 3(12): p. eaao6804.
202. Diamantides, N., et al., *High density cell seeding affects the rheology and printability of collagen bioinks.* Biofabrication, 2019. 11(4): p. 045016.

203. Boularaoui, S., et al., *An overview of extrusion-based bioprinting with a focus on induced shear stress and its effect on cell viability.* Bioprinting, 2020. 20: p. e00093.
204. Blaeser, A., et al., *Controlling Shear Stress in 3D Bioprinting is a Key Factor to Balance Printing Resolution and Stem Cell Integrity.* Advanced Healthcare Materials, 2016. 5(3): p. 326-333.
205. Cidonio, G., et al., *The cell in the ink: Improving biofabrication by printing stem cells for skeletal regenerative medicine.* Biomaterials, 2019. 209: p. 10-24.
206. Nair K, G.M.K.S.Y.K.C.M.M.B.K. and W. Sun, *Characterization of cell viability during bioprinting processes.* Biotechnol. J., 2009. 4: p. 1168.
207. Li, M., et al., *Effect of needle geometry on flow rate and cell damage in the dispensing-based biofabrication process.* Biotechnology Progress, 2011. 27(6): p. 1777-1784.
208. Billiet T, G.E.D.S.T.C.M. and P. Dubruel, *The 3D printing of gelatin methacrylamide cell-laden tissue-engineered constructs with high cell viability.* Biomaterials, 2014. 35: p. 49.
209. Williams, C.G., et al., *Variable cytocompatibility of six cell lines with photoinitiators used for polymerizing hydrogels and cell encapsulation.* Biomaterials, 2005. 26(11): p. 1211-1218.
210. Jakus, A.E., A.L. Rutz, and R.N. Shah, *Advancing the field of 3D biomaterial printing.* Biomedical Materials, 2016. 11(1): p. 014102.
211. Kean, T.J. and M. Thanou, *Utility of Chitosan for 3D Printing and Bioprinting*, in *Sustainable Agriculture Reviews 35: Chitin and Chitosan: History, Fundamentals and Innovations*, G. Crini and E. Lichtfouse, Editors. 2019, Springer International Publishing: Cham. p. 271-292.
212. Freyman, M.C., et al., *3D printing of living bacteria electrode.* Nano Research, 2020. 13(5): p. 1318-1323.
213. Wei, J., et al., *A 3D-printable TEMPO-oxidized bacterial cellulose/alginate hydrogel with enhanced stability via nanoclay incorporation.* Carbohydrate Polymers, 2020. 238: p. 116207.

3

Materials and methods

Chapter 3 has been partially adapted from Bioprocess and Biosystems Engineering, 2019 - 42(7): p. 1215-1224 (DOI: 10.1007/s00449-019-02119-4) with permission from Springer Nature number 5265951472044 [1], from Journal of Materials Science, 2022 - 57, 3662–3677. (DOI: 10.1007/s10853-021-06829-7) with permission from Springer Nature [2], and from Bioprocess and Biosystems Engineering, 2022 - 45: p. 171-185. (DOI: 10.1007/s00449-021-02650-3) with permission from Springer Nature [3]. Additionally, a detailed description of feedstocks synthesis can be found in Chapters 4 [1], 5 [2], and 6 [3] along with the results and discussion of the referring topic.

3.1 Materials and chemicals

All materials and chemicals used in this work are listed here. The polymers used in this work were alginic acid sodium salt from brown algae - medium viscosity (product number: A2033) from Sigma Aldrich Chemie GmbH (Taufkirchen, Germany), sodium alginate (Protanal LFR 5/60) from FMC Biopolymer (Philadelphia, USA) and chitosan polymer with 85 ± 5% deacetylation degree, η=15-25 cps. The alumina powder (CT 3000 SG, d50 = 500 nm, purity 99.78%) was purchased from Almatis (Ludwigshafen am Rhein, Germany) and protein albumin from chicken egg white powder 62-88% (ovalbumin) (product number: A5253) from Sigma Aldrich Chemie GmbH. Crosslinking was done with calcium carbonate (product number: 795445), gluconic acid (product number: G1951), and with calcium chloride dehydrate (product number: 21102), all from Sigma Aldrich Chemie GmbH (Taufkirchen, Germany), or with genipin (product number: 6902-77-8) from Challenge Bioproducts Co., Ltd. (Douliu city, Taiwan).

For bacteria cultivation lysogeny broth (LB) medium (product number: L3022), Sodium Chloride (product number: S7653) and phosphate buffered saline PBS (product number: P4417) were purchased from Sigma-Aldrich Chemie GmbH. For bacterial viability measurements BacTiter-Glo (product number: G8231) from Promega (Walldorf, Germany), resazurin salt (product number: Cay14322) from Cayman chemical (Hamburg, Germany), and WST-I assay (product number: 5015944001) from Roche (Mannheim, Germany) and for fluorescence microscope SYTO 9 and propidium iodide (Live/Dead viability kit – product number: L10316) from Thermo Fisher Scientific (Waltham, USA) were used. For glucose consumption tests, glucose (product number: G8270) from Sigma Aldrich Chemie GmbH and Glucose Liquicolor (product number.: 10121, Lot.: 0168) from HUMAN (Wiesbaden, Germany) were used.

3.2 Rheology of suspensions for 3D printing

Bioink materials must fulfill two primary criteria: high cell viability and high printability, whereas printability is the ability to form 3D structures with good shape fidelity and integrity. Thus, understanding the flow behavior of suspensions is essential and facilitates the printing process [4]. Rheology is the science of deformation and flow of fluids, and it is used to characterize particle-liquid systems and how their interactions with each other affect suspensions flow and deformation behavior. Fluid internal friction forces are generated by the constant movement of the molecules. Thus, by applying shear rate ($\dot{\gamma}$), a certain shear stress (τ) will be necessary to move the fluid. The quotient of shear stress divided by shear rate is the viscosity (η) (Equation 2.2) [5-8].

The viscosity of a fluid depends on the intermolecular interactions and can be either constant with the increase of shear rate/shear stress (Newtonian fluid) or change with the increase of shear rate/shear stress (non-Newtonian fluid). Newtonian fluids have a linear relationship between shear stress and shear rate (Figure 3.1) and describe an ideal fluid behavior, such as water. Adding particles or polymers into water to form a suspension increases the complexity of the system. Molecules and particles start to interact with each other, and this interaction can be altered by increasing or decreasing shear rate/stress describing a non-Newtonian fluid. Certain suspensions generate particle agglomeration by increasing shear rate/stress and this results in an increment of viscosity with increasing shear rate, describing a shear thickening behavior (Figure 3.1). In opposition, and more often, agglomerates can be disintegrated by increasing shear rate causing a reduction of viscosity by increasing shear rate, describing a shear thinning fluid (Figure 3.1). Furthermore, particles and molecules can be oriented by increasing shear rate and this orientation facilitates the movement, also decreasing suspensions viscosity. Moreover, many fluids additionally show a Bingham behavior, in which flow only initiates above some level of stress - called yield stress (Figure 3.1). This behavior is also described as a transition from an elastic-plastic deformation region. While shear is applied and does not irreversibly disturb the structure of the fluid, the fluid does not flow and describes the elastic region. When stress overcomes the yield stress, an irreversible distortion of the system takes place and results in the flow initiation, describing the outset of the plastic deformation [5-8].

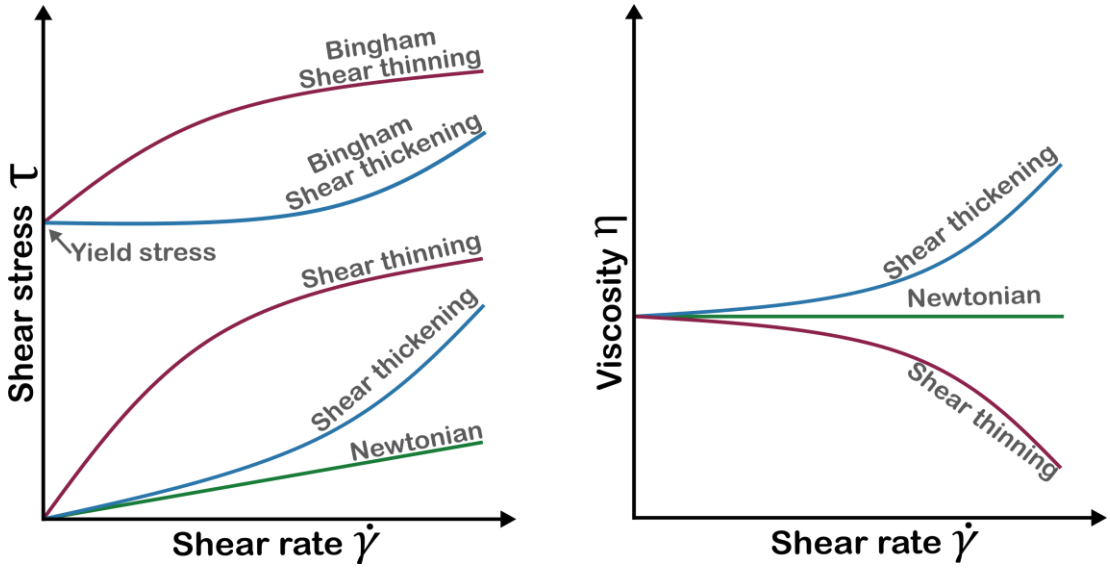

Figure 3.1 – Representation of the relationship between shear stress and shear rate as well as viscosity and shear rate for Newtonian and non-Newtonian (shear thinning and shear thickening) fluids. Furthermore, Bingham behavior is also represented where the fluid flow initiates just after some level of stress (yield stress).

In addition to the shear rate dependence, suspensions flow behavior is usually time-dependent as well. In this case, viscosity changes with shearing time because particles and molecules require time to arrange. If a suspension is sheared at a constant rate and its viscosity decrease, this fluid has a thixotropic behavior. In opposition and less often, viscosity can increase at a constant shear rate (rheopectic behavior) [5-8].

Suspensions usually have viscoelastic properties, where a part of the mixture has a solid-like behavior (G') and another part shows a liquid-like behavior (G''). The solid-like properties are described by the elastic modulus (G') and the liquid part by the viscous modulus (G') via oscillatory rheological tests. For instance, gel materials act as solid materials and show a G' higher than G''.

Optimal feedstocks for extrusion 3D printing should have a shear thinning behavior with a clear yield point to allow feedstock to flow through the nozzle just when pressure is applied. The feedstock should ideally have an instantaneous recovery of properties after printing to avoid filament deformation. The feedstock materials should exhibit a solid-like behavior of the printed filaments already previous to the crosslinking process, which should be strong enough to maintain filament shape and support the deposition of further layers. Furthermore, printed filaments should stack with each other without merging and gelation should occur after filament extrusion to avoid nozzle blocking [9,10].

In this work, a rotational rheometer Kinexus pro (Malvern Panalytical, Kassel, Germany) was used to characterize feedstock properties. Here, the feedstock is positioned between a metallic plate/plate geometry, whereas the upper plate can rotate and the base plate is fixed (Figure 3.2). The movement of the upper plate with a force F initiates the shearing of the feedstock and results in a movement of the feedstock with a velocity profile v higher near to the upper plate and lower near to the fixed plate. The resistance to the movement and resultant torque are measured and can correlate to feedstock rheological properties such as viscosity in dependence of time, shear rate, and flow initiation [5-8]. If the upper plate moves in an oscillatory instead of a rotatory pattern, viscoelastic properties can be measured to understand elastic behavior and crosslinking time.

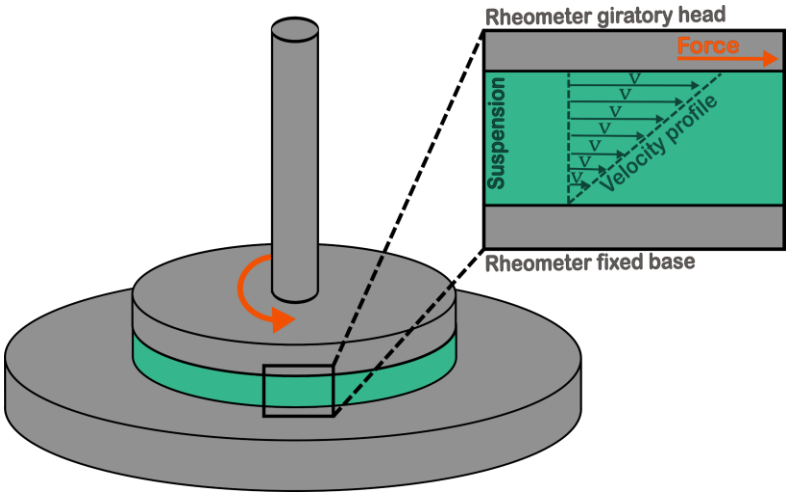

Figure 3.2 - Illustration of rheological measurement of a suspension, whereas the base plate is fixed and the head plate is gyratory/oscillatory. By the movement of the head, a force is applied to the suspension in the direction of the head movement and results in a velocity profile of the suspension.

To test feedstocks rheological behavior, the feedstocks were deposited between a base plate and a Ø 20 mm parallel plate geometry at a gap of 0.5 mm at a temperature of 30°C and a solvent trap containing water was positioned around the plate to avoid drying. Stepped shear rate increment experiments were performed to analyze the change of viscosity with a shear rate range between 0.01 and 1000 s^{-1} with 8 logarithmic increments per decade of shear rate and 1 min holding time at each shear rate. Additionally, the yield point of the suspensions was determined with a continuous shear rate ramp from 0.001 to 100 s^{-1}. Thixotropic behavior was analyzed by a three-step shear test with a shear rate of 0.05 s^{-1} and a holding time of 60 s for the first step, 50 s^{-1} for 60 s for the second step and 0.05 s^{-1} for 60 s for the third step.

Furthermore, oscillatory tests were performed to analyze the viscoelastic behavior of the feedstocks [11]. First, amplitude tests were performed between 0.01 and 100% amplitude with a constant frequency of 0.5 Hz to determine the linear viscoelastic (LVE) range or rather regions of parallel moduli that indicate reversible deformation. Thereafter, frequency sweep tests were performed to analyze changes in the structure within 0.01 to 50 Hz frequencies and 0.05% shear strain. Additionally, time tests were performed at a constant frequency of 0.5 Hz and constant amplitudes of 0.05% or 10% over a duration of 8 h to analyze feedstock gel formation.

3.2.1 Interfacial shear rheology

Surface rheology is considered an important approach to understand the mechanisms of bubble formation and stability. While bulk rheology characterizes interactions between particles and polymers in the fluid, interfacial rheology describes the interactions between adsorbed molecules and particles at the air/water interface [12, 13].

Proteins adsorb spontaneously at the air/water interfaces to reduce the interfacial free energy. During the adsorption, proteins unfold and establish intermolecular interaction with each other at or close to the air/water interface leading to the formation of an interfacial film with viscoelastic properties. A correlation between bubble formation and stability can be established by understanding the viscoelastic properties of the film via interfacial shear rheology. Some associations between surface viscoelasticity and foam properties were defined in the past years such as (i) films with large elastic modulus result in small strain for a given stress, consequential less stretch of the foam film is observed and it is less likely ruptured; (ii) the film elasticity will restore the interface by bringing back surfactants and by limiting the stretch of the interface; (iii) surface elasticity modifies the process of drainage in foam films and controls the appearance of bell-shaped liquid drops that have a destabilizing effect on films [14-16].

In this work, interfacial shear rheology was used to understand which and how the feedstock components (alumina, alginate, albumin) influence film formation and elasticity at the air/water interface and correlate the results to bubble stability. Interfacial shear rheology measurements are sensitive to the fluid composition and measure intermolecular interactions between the adsorbed molecules by disrupting a film with shear and describe film growth and integrity, which is related to bubbles' long-term stability. Thus, interfacial shear rheology was measured using a high-precision stress-controlled rheometer (DHR-3 rheometer from TA Instruments, New Castle, USA). The feedstocks were diluted ten times with water to ensure that the rheological modules of the bulk phase are significantly lower than those of the interface. Thereafter, 5.8 mL of the diluted suspension was loaded

into a double-wall Delrin support to pin the meniscus. Subsequently, a Pt/Ir DuNoüy ring (20 mm ring diameter, 0.36 mm wire diameter) was positioned exactly at the air/suspension interface (as illustrated in Figure 3.3) and time test measurements were performed in the linear-viscoelastic region with 0.1% strain amplitude and 0.1 Hz frequency. The measurements were repeated in triplicates showing similar plateau values, although the kinetics of adsorption were less reproducible. Solutions containing only water and albumin solution were tested as well for comparative purposes.

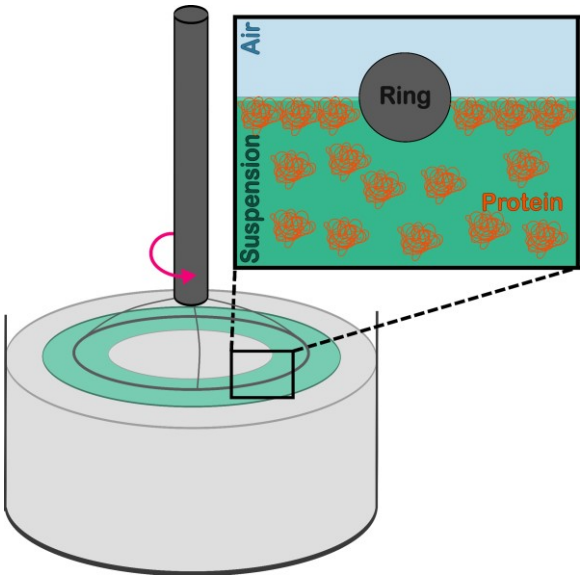

Figure 3.3 – Illustration of interfacial rheology using a ring at the air/suspension interface to measure film elastic modulus of suspensions containing alginate, alumina, and albumin.

3.3 3D printer settings

3D bioprinting materials consist of a pre-processing stage, where the geometry is generated in a computer-aided design program (CAD); a processing stage where the bioink is deposited to build the 3D construct; and a post-processing stage, where the crosslink takes place [17]. In this work, a solid cuboid (2 x 2 x 1 cm) was initially generated using the software SolidWorks. Thereafter, the solid cuboid was uploaded into the software Cellink HeartWare 2.4.1 to generate the numerical controlled programming language G-code with the printing commands with a 67 % infill density, a 0.85 mm layer height, and a 10 mm/s printing speed. The processing stage consists in printing the feedstock into lattice cubes (2 x 2 x 1 cm) with an extrusion printer (Inkredible by Cellink, Gothenburg, Sweden – Figure 3.4). Feedstocks were loaded into the printing cartridge connected to a precision tip nozzle (Ø 940 µm) at one end while on the other end a pneumatic pressure of 20 ± 5 kPa was applied to establish the feedstock flow and the

printed filament was deposited in a 6-well plate for the post-processing stage of crosslinking.

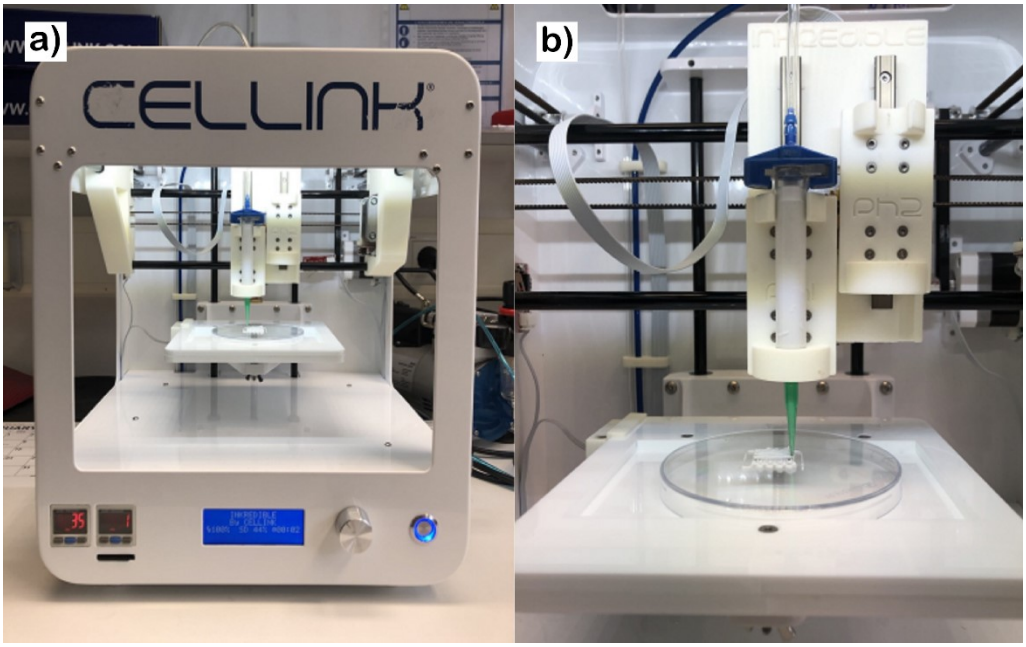

Figure 3.4 – Illustration of the 3D printed from Cellink in a) while b) the printing procedure the cartridge filled with the feedstock and the green precision tip nozzle attached to the cartridge, which defines the printed filament diameter.

3.4 Feedstock printability characterization

Feedstock printability, namely the ability to form 3D structures with good fidelity and integrity, was evaluated by means of image analysis. Ideally, printed constructs should display a clear morphology with smooth surfaces, constant diameters after printing and the ability to stack with other filaments without merging. Therefore, for regular lattice grid structures, square-shaped holes should in principle be formed in the interstitial spaces between interconnected filaments in the fabricated constructs. Ouyang et. al. [18] proposed an approach to define bioink printability (Pr) based on the analysis of the hole shape using Equation 3.1:

$$\mathrm{Pr} = \frac{L^2}{16A} \qquad \text{Equation 3.1}$$

Where L means hole perimeter and A means hole area. Ideally, Pr values should be 1 so that the interconnected channels of the constructs would form a square shape. $\mathrm{Pr} > 1$ indicates that the feedstock shows a high solid-like behavior, usually due to an early crosslinking, and printing constructs show a fractured morphology with irregular filaments while $\mathrm{Pr} < 1$ points towards insufficient crosslinking, where the feedstock shows a liquid-

like behavior and filaments merge with each other, forming circular holes rather than square holes (Figure 3.5).

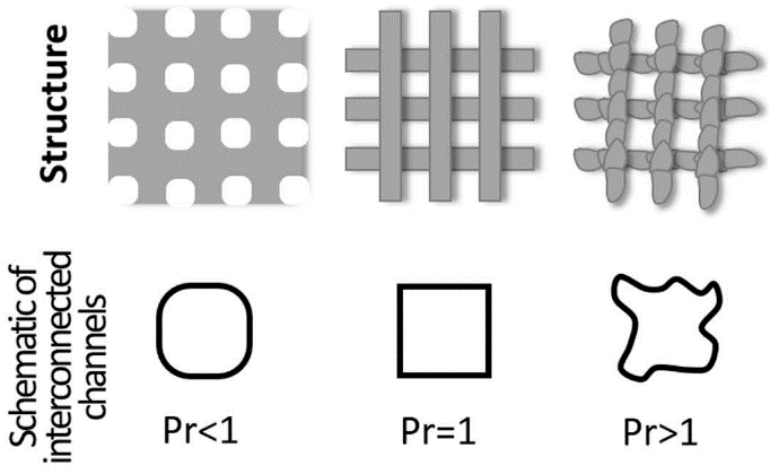

Figure 3.5 – Illustration of the grip shape and its printability value (Pr). Pr < 1 means insufficient crosslinking, Pr = 1 for optimal printability, and Pr > 1 means that the feedstock shows a high solid-like behavior, usually due to an early crosslinking. Adapted from [18].

To determine Pr values of printed samples, the spacing between interconnected channels was analyzed after printing 3 and 8 layers with a digital optical microscope (VHX-5000 from Keyence - Neu-Isenburg, Germany) after drying at ambient conditions. Perimeter and area of the space between the interconnected channels were determined using the microscope's software VHX-5000 from Keyence.

3.5 Microscopy analysis: optical, fluorescence and electron microscope

Microscopy is used to view objects, surfaces, and areas which can not be seen by the human eye. Electromagnetic radiation or electron beams can interact with a material surface by e.g. reflection, adsorption, refraction or diffraction, and the scattered radiation/electron beam is used to generate the image. There are different types of microscopes, such as optical, fluorescence, electron scanning and X-ray microscope. Different microscopes are used to examine the material from different perspectives such as color, polarization, magnification, topography, densities, and inner structure [19-22]. The three microscopy techniques used in this work were optical, fluorescence, and scanning electron microscopy and each technique is going to be explained in more detail.

Optical microscopy

Optical microscopes use the transmission of visible light to observe samples in a 2D pattern. Basically, visible light is projected onto the surface of the samples, whereas the light is either reflected (surface examination) or transmitted through the sample (biological samples). The light passes through a multi-lenses system to increase the magnification of the sample, which can range up to 50,000x and a resolution of up to 250 nm under ideal conditions [20]. In this work, the printability of samples was measured using an optical microscope (VHX-5000 from Keyence - Neu-Isenburg, Germany) with a magnification of 30x after printing 3 and 8 layers while the cross-section of the printed structure was likely analyzed after printing 8 layers but with 50x magnification.

Fluorescence microscopy

Fluorescence microscopes are optical microscopes that emit and capture radiation at different wavelengths to form an image. Certain materials and chemicals have the ability to emit visible light (fluorescence light) after absorbing radiation of a short wavelength which is normally not visible, such as blue or ultraviolet (UV) light. Thus, the microscope illuminates the sample with light of a short wavelength and a fluorescence light is emitted at another wavelength from the sample [21]. Some samples are naturally fluorescent and do not need any extra chemicals to be analyzed. Still, several biological characterizations can be performed by means of fluorescent microscopy, such as visualization of tissues, cell nuclei, membranes, and can even measure cell viability. This technique helps to further understand the impact of processes and chemicals on cell viability and morphology. In this case, solutions containing certain molecules such as fluorophores, dyes, and assays are required [23]. When these molecules are excited by illumination of a short wavelength, the short wavelengths is converted into a longer wavelengths and light with different colors is emitted depending on emitted wavelength, which again depends on the composition of the substance [24, 25].

For characterization of bacterial viability in the nanocomposites, bionanocomposites were cut into small pieces and stained with the chemicals from Thermo Fischer Scientific SYTO 9 and propidium iodide (Live/Dead staining) for 20 min, protected from light. SYTO 9 and propidium iodide are nucleic acids stains whereas SYTO 9 can enter all cells regardless of their membrane integrity, bind to DNA and RNA and emit green fluorescence light while propidium iodide can only enter cells with compromised membranes, bind to DNA and RNA and emit a red fluorescent light [26]. Thus, bionanocomposites were analyzed in a fluorescence microscope (AXIO from Zeiss) and the green color was emitted by SYTO 9 for living cells and red color was emitted by propidium iodide for dead cells.

Scanning electron microscopy

Scanning electron microscopy (SEM) is used to observe and study the surface topography, grain sizes, and chemical composition of many materials with a higher resolution than optical microscopes. An SEM is composed of an electron gun, which generates an electron beam. This electron beam passes through an electron column containing condenser lenses, scanning coils and deflector plates, to accelerate, focus, and deflect the electron beam onto the surface of the sample. When the beam hits the sample, the emitted electrons (primary electrons) lose energy by repeated scattering and adsorption and three different interactions can take place, generating secondary electrons, backscattered electrons, or characteristic X-ray radiation [19, 27].

Secondary electron images give more information about the surface and topography due to the superficial electron interactions. Backscattered electron images give deeper material information whereas the differences in image contrast depends on the atomic number of the atoms which constitute the material. This technique is mostly used to detect areas with different chemical compositions. X-ray information can just be translated if an energy-dispersive X-ray detector (EDS) is built into the SEM. The emitted characteristic X-rays have a specific wavelength depending on the atom the electron beam interacted with. Thus, this signal can be translated using the EDS detector to characterize atomic chemical composition and, in some cases, even quantification of some elements [28, 29].

In this work, SEM was used to observe the surface topography of the printed foams after samples dried for 5 days. SEM Camscan Series 2 (from Obducat CamScan Ltd. – Cambridge, UK) was used for the surface analysis using secondary electron images with 80x magnification.

3.6 Porosity measurements

3.6.1 Mercury intrusion porosimetry

Mercury intrusion porosimetry is a technique used to precisely measure pore size distribution and porosity of open porous samples with pores ranging between 0.01 and 10 µm. This technique is based on the penetration of mercury into the pores by the application of pressure since mercury has a high surface tension (480 mN/m) and contact angle (140°) and usually does not spontaneously adsorb on ceramics. The pressure applied depends on pore size and a correlation between pressure (p), pore radius (r_p), surface tension (γ) and contact angle ($\emptyset$) can be calculated by using the Washburn equation [30, 31] (Equation 3.2).

$$r_p = -\frac{2\gamma\cos(\emptyset)}{\Delta p} \qquad \text{Equation 3.2}$$

In this work, hydrogel nanocomposite samples were dried for 5 days at ambient conditions and thereafter sample porosity and pore size distribution between 0.01 and 10 µm was determined by mercury intrusion porosimetry (Pascal 140 and 440, Porotec – Hofheim am Taunus, Germany). The measurements were performed according to DIN 66133 using a pressure range between 0.1 and 400 kPa and an accuracy of < 0.24%.

3.6.2 Micro-computer tomography (µCT)

X-ray micro-computed tomography (µCT) is an advanced non-destructive imaging technique based on the attenuation of X-rays passing through a specimen to generate digital three-dimensional models of samples. The technique is similar to the computed tomography (CT) used in hospitals to examine the organs and bones of patients but µCT uses finely focused X-ray sources and microscope optics, allowing us to analyze micron to sub-micron three-dimensional details in samples [32-34].

In µCT, X-rays with wavelengths between 0.01 and 1 nm pass from a source, through a sample, to a detector (Figure 3.6). The detector produces a two-dimensional image of the sample's interactions with the X-rays. Differences in contrast depends on the X-ray adsorption whereas adsorption increases (contrast decrease) with the increasing of atomic number and material density. Three-dimensional models of the sample can be reconstructed by taking a series of 2D projection images as the sample is rotated by at least 180°. The 2D images are combined using geometrical calculations from the machine software to form an 'image stack' that represents virtual layers through a digital three-dimensional volume of the sample [34].

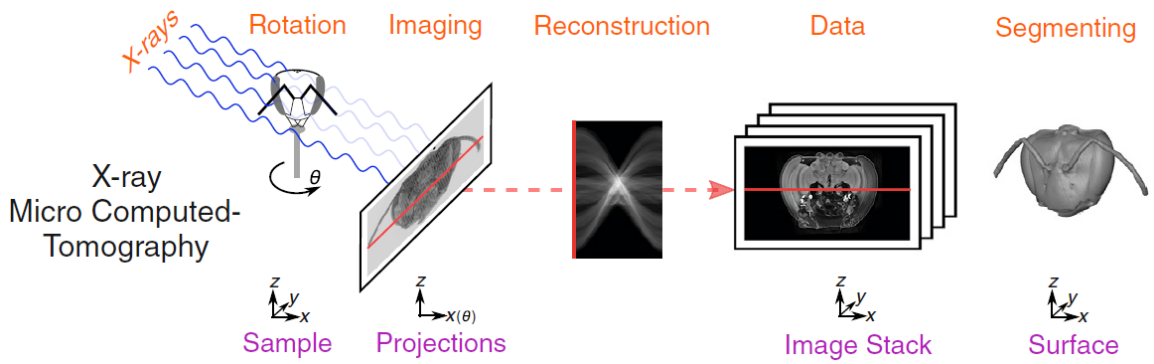

Figure 3.6 – Illustration of X-ray microcomputed tomography (µCT) measurements from a fly head whereas the X-rays pass through the specimen to generate a 2D image. A 3D models can be generated by stacking images done at different angles. Adapted from [34] with permission from Elsevier number 5265411221185.

In this work, X-ray microcomputed tomography (μCT) was used to determine pores sizes bigger than 10 μm. For this purpose, dry samples were cut into 5 x 5 x 5 mm cubes and were analyzed with μCT Xradia 520 Versa (from ZEISS – Jena, Germany). The images are generated by the attenuation of X-rays passing through the samples, whereas the voltage and X-ray radiation strength parameters are specified in Table 3.1. Thereafter, a reconstruction algorithm based on the work of Katsevich et al. [35] is used to generate a 3D spatial representation based on the helix trajectory through which the object has moved along. In the reconstructed image, each voxel with its 16-bit grayscale value represents a corresponding X-ray attenuation coefficient that is associated with the density of the sample.

Table 3.1 - X-ray microcomputed tomography scanning parameters and specifications.

Scanning parameters	Specification
Radiographic field of vision [mm]	28×35
Number of display voxels	982 X 1011
Detector pixel size [μm]	140
Acquisition time [min]	45
Exposure time [s]	0.7
Energy of X-ray	70 kV (6000 mA)
Number of projections per revolution	2400
Total number of projections	1024
The angular step [°]	0.15
Recorded data type	16-bit integer

Digital reconstruction of μCT images

For the μCT reconstruction, a binary image was generated indicating either voids or the matrix by using the Otsu multilevel filter to segment the background of the investigated region of interest of the sample from the matrix and pore volumes. A morphological filter was applied on the segmented binary pore images to remove salt and pepper type noise with a kernel size of 3 voxels in each axis. Only pore diameters larger than 10 μm were resolved by μCT analysis and regions with smaller pore sizes appear as dense material in the filtered image. Connected pores were then separated by applying a distance transform filter on the binary image and subsequently, the 3D watershed algorithm was applied. For pore analysis, each pore was labeled, and their respective morphological parameters pore diameter, volume and sphericity were calculated. From the individual pore properties, the pore size and pore volume distributions of pores > 10 μm were

obtained. Still, pores smaller than 10 μm cannot be measured by the μCT scans and thus these regions appear as dense material. Thus, to define samples' total porosity, mercury intrusion porosimetry and μCT techniques were combined. First, the total volume (V_{Total}) of the samples using the μCT scans was calculated by the sum of samples volume of the solid part (V_{solid}) and the volume of the pores (V_{pore}).

$$V_{Total} = V_{solid} + V_{pore} \quad \text{Equation 3.3}$$

The porosity of the samples with pores bigger than 10 μm ($P_{>10}$) was defined as the quotient between V_{pore} and V_{Total}:

$$P_{>10} = \frac{V_{pore}}{V_{Total}} \quad \text{Equation 3.4}$$

For pores smaller than 10 μm ($P_{<10}$), the volume solid part V_{solid} was multiplied by the porosity results obtained from mercury intrusion porosimetry (P_{Hg}) and it was divided the product by V_{Total}.

$$P_{<10} = \frac{V_{solid} \times P_{Hg}}{V_{Total}} \quad \text{Equation 3.5}$$

The total porosity (P_{total}) was calculated by the sum of $P_{>10}$ and $P_{<10}$ as follow:

$$P_{Total} = P_{>10} + P_{<10} = \frac{V_{pore}}{V_{Total}} + \frac{V_{solid} \times P_{Hg}}{V_{Total}} \quad \text{Equation 3.6}$$

3.7 Water content measurements by nuclear magnetic resonance (NMR)

Nuclear magnetic resonance (NMR) or magnetic resonance imaging (MRI) analyzes the molecular structure of a material by observing and measuring the interaction of nuclear spins when placed in a powerful magnetic field. MRI is known in the medical field to examine different tissues, but it has also application in the chemical reaction field to measure fluid diffusivity, molecule adsorption/desorption, and its influence on chemical/biological reactions [36, 37]. In this work, NMR was used to determine diffusion coefficients of water inside the porous hydrogel nanocomposite.

The technique works by applying a magnetic field B_0 onto the sample. With the magnetic field, the nucleus from some atoms aligns to the magnetic field B_0, resulting in a spin magnetization vector (M_0) which points towards the B_0 direction defined as z direction. While a magnetic field is still acting on the sample, a short radio frequency (RF) excitation pulse is applied onto the sample. This short pulse will disturb the atoms' spin, which flips

the magnetization vector to xy plane (M_{xy}). Thereafter, the magnetization vector realigns back to the magnetic field B_0 in the z direction, whereas the realignment emits a radio frequency pulse back as an oscillating signal wave. This wave is called the free induction decay (FID) which is a representation of the wave in the time domain. Depending on the atom, the free induction decay can differ and that is how different atoms can be differentiated [38-40].

Time is an essential variable in MRI measurements. For instance, four different times are relevant: repetition time (T_R), which is the time between successive radio frequency pulses; echo time (T_E), which refers to the time between the application of the radio frequency excitation pulse and measurement of the oscillating signal; and relaxation time, which can be divided into longitudinal and transverse relaxation time T_1 and T_2, respectively, and is important since magnetization (M) is a function of relaxation time T_1 and T_2. T_1 is longitudinal relaxation time which is the time needed for the longitudinal magnetization (M_z) to recover towards the equilibrium in z direction (M_0) after a radio frequency pulse. T_2 describes the exponential decay of the transverse magnetization (M_{xy}) towards zero. Figure 3.7 illustrates the different times and how T_1 and T_2 are related to the magnetization. In MRI, relaxation times are used to characterize the dynamics of molecules and are sensitive to the surrounding environment, which could be a human cell or a pore in porous media. Different porous structures will cause different relaxation properties based on the surface chemistry and pore size [39-41].

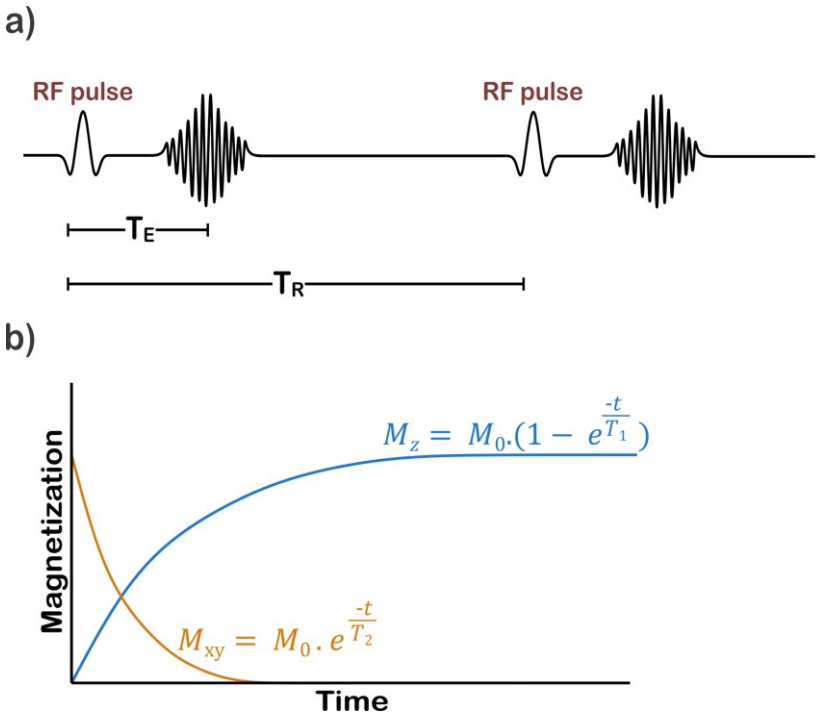

Figure 3.7 - a) shows the illustration of the echo time (T_E) and repetition time (T_R) after the radio frequency (RF) pulse while b) shows the relationship between longitudinal and transverse relaxation time T_1 and T_2 and respective longitudinal magnetization (M_z) and transverse magnetization (M_{xy}) recovery towards the equilibrium.

Large molecules and solids, such as ceramics, have short T_2 relaxation times while small molecules, such as water, have long T_2 relaxation times. Thus, to analyze water in solid porous ceramics, zero echo time (ZTE) pulse sequences MRI measurements can be used due to very short effective transverse relaxation time (T_2*). In zero echo time MRI measurements, frequency encoding gradients are switched on before the radio frequency excitation pulse is applied. A series of measurements with a short repetition time T_R is necessary to acquire data with different gradient orientations. Thereafter, the acquired data with different gradient orientations allows the reconstruction of a 3D image by 3D fast Fourier Transform [41, 42].

In order to measure water content in the bionanocomposites, magnetic resonance imaging (MRI) experiments were performed using a 7 Tesla preclinical MRI scanner (Bruker Biopin MRI GmbH, Ettlingen, Germany) equipped with a magnetic field gradient system BGA12S2 (maximum gradient strength per direction (x,y,z) 442 mT/m, rise time 130 µs). The Software platform Paravision 5.1 was used for both MRI measurements and data processing. Crosslinked samples were submerged in water for 2 weeks and thereafter positioned in the device. Images were generated using scout images of three orthogonal slices followed by a 3D gradient echo MRI sequence (repetition time T_R = 30 ms, echo time T_E = 0.9 ms, signal excitation with a flip angle of 30°, field-of-view: 32x32x32 mm^3, matrix size: 128x128x128 pixels).

Thereafter, MR images of a 1.5 mm slice were measured using two different pulse sequences to exploit spin relaxation time (T_2) and diffusion as contrast mechanisms. For that purpose, a multi-spin-echo MRI sequence (field-of-view: 32x32 mm^2, matrix size 64x64, spectral width 50 kHz, repetition time T_R = 1000 ms, 4 echoes with an echo time T_E 0f 5, 10, 15, 20 ms; two averages) was used for T_2 contrast. Second, a diffusion-weighted stimulated echo MRI sequence was applied for diffusion contrast (field-of-view: 64x64 mm^2, matrix size 64x64, spectral width 50 kHz, repetition time T_R = 1000 ms, echo time T_E = 9.9 ms, four averages, two diffusion sensitizing gradients with a duration of d = 2 ms separated by D = 50 ms, four images with diffusion weighting factor b=50, 400, 750, 1100 s/mm^2).

3.8 Compressive mechanical test

Particles can be integrated into hydrogels to form hydrogel nanocomposites to increase the mechanical properties of the hydrogels. In this work, alumina nanoparticles were integrated into alginate gels to increase mechanical properties and shape fidelity and the influence of the particles on mechanical properties after the crosslinking was measured by compressive tests. For that, eight types of cylindrical samples were prepared: alginate with internal gelation, alginate with internal/external gelation, nanocomposite with internal gelation, and nanocomposite with internal/external gelation. The proportion diameter: the length was set between 1:1 and 1:1.5. The tests were performed in a universal testing machine (Zwick/Roell Z005) and a half sphere was positioned on the sample to assure that the force was uniformly applied in the whole sample (Figure 3.8). The surfaces in contact with the sample were covered with a thin layer of oil (WD-40), to reduce the effect of friction between the gel and the machine during the compression test. Since these materials have high elastic properties, the cross-section will increase with the application of the force. Therefore, the cross-sectional area must be corrected in order to obtain reliable compressive strength results using Equation 3.7:

$$A_C = \frac{A_0}{1-\varepsilon} \qquad \text{Equation 3.7}$$

Where A_C is the corrected area, A_0 is the initial area and ε is the strain, which is defined as a quotient of the variation of high L and initial high L_0 ($\varepsilon = \frac{\Delta L}{L_0}$). After knowing the correct area of the cross-section it is possible to calculate the compression strength ($\sigma_{\text{comp.}}$) using Equation 3.8:

$$\sigma_{\text{comp.}} = \frac{F}{A_C} \qquad \text{Equation 3.8}$$

The elastic modulus of these materials was calculated from the slope of the stress vs. strain curves.

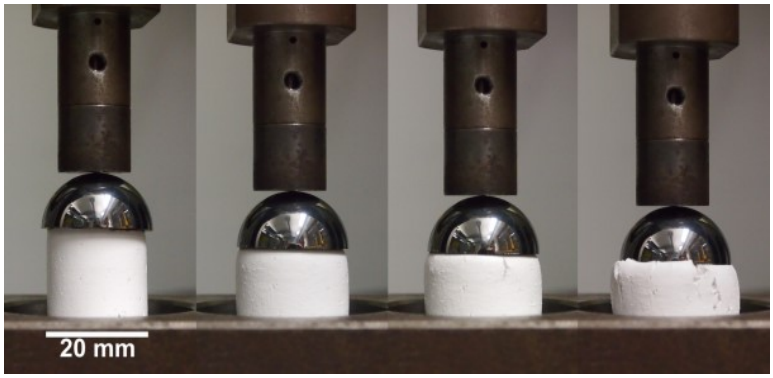

Figure 3.8 – Visualization of mechanical compression tests of the composite.

Table 3.2 - Parameters used on the flexural tests.

Parameters	
Travel speed	0.5 mm/min
Number of specimens	20
Distance on the base	40 mm
Distance on the top	10 mm

3.9 Bacterial strain and culture conditions

The bacterial strain *Escherichia coli* K12 (DMS 1077) and *Bacillus subtilis* (DMS 1088) were used as model bacteria to analyze the biocompatibility of the processing and crosslinking techniques from the bionanocomposites. *Escherichia coli* and *Bacillus subtilis* are gram-negative and gram-positive bacteria, respectively, and this means their cell membrane differs. Gram-negative bacteria have a thin peptidoglycan layer and have an outer lipid membrane while gram-positive bacteria have a thick peptidoglycan layer without an outer lipid membrane [43]. Both bacteria strains were set to grow in sterile Lysogeny broth (LB) medium at 37 °C under agitation at 150 rpm in an incubator (Heidolph Unimax 1010). Cells were centrifuged at 2500 rpm for 10 min to obtain the cell pellet. After that, the supernatant was mixed with phosphate buffered saline solution (PBS) until the desired concentration of approx. $32.5 \cdot 10^8$ cfu/mL of *E. coli* and $15 \cdot 10^8$ cfu/mL of *B subtilis*.

3.10 Propagation and characterization of bacteria

Characterization of immobilized bacteria was done without destruction of the bionanocomposite. Therefore, all viability measurements of immobilized cells show effective bacterial viability instead of total viability. Effective viability relates to the viability of the cells accessible by the assay molecules and the corresponding metabolite which could release the sample, considering not just bacteria viability but also permeability and diffusion aspects. Still, effective bacteria viability was given in this work always relating to similar experiments done with freely suspended bacteria. In total, four characterization assays were used in this work and the specifications are described below.

3.10.1 Bac Titer-Glo assay

Bac Titer-Glo assay was used to measure the influence of genipin on the viability of *E. coli* by incubating suspended bacteria in PBS with different concentrations of genipin: 1 mM, 0.75 mM, 0.5 mM, 0.25 mM, and a control of cells in PBS (0 mM). Bacteria-containing suspensions were then incubated at 37°C and 150 rpm and bacterial viability was determined after 5 and 24 h incubation using BacTiter-Glo assay. BacTiter-Glo is mixture to the solution after 5 or 24 h incubation for 5 min protected from light and thereafter the luminescence was measured with a Hidex Chameleon V plate reader (Mainz, Germany).

Crosslinked genipin is a fluorescent molecule [44, 45] and therefore an assay based on a fluorescent signal would give erroneous results. Thus, Bac Titer-Glo assay using luminescence was the suitable assay to measure cell viability after incubation.

3.10.2 Resazurin assay

Resazurin assay was used to determine immobilized cell viability by incubating the whole sample and comparing the results with freely suspended cells using also resazurin assay. The resazurin solution stocks were produced as follows: 1 g of resazurin salt was dissolved in 100 mL of sterile PBS and stirred for homogenization, followed by a filtration step in 0.2 µm filters under sterile conditions to obtain resazurin stock solutions with a concentration of 10 g/L. Resazurin can be reduced by viable cells with active metabolism into resorufin, which is pink and fluorescent. The product was quantified by measuring the fluorescence at excitation at 540 nm and emission at 590 nm using a UV/vis photometer (Chameleon V from Hidex – Mainz, Germany).

Immobilized bacteria viability was measured with an assay containing resazurin. For that, three replicates of gel-cast or 3D printed samples containing *E. coli* or *B. subtilis* were incubated protected from light for 4 hours at 37°C and 160 rpm in a solution of PBS with 10% of resazurin solution stock (Figure 3.9), as described above. Thereafter, effective bacterial viability was determined by measuring supernatant fluorescence at excitation at 540 nm and emission at 590 nm. The same experiment was performed with different known concentrations of freely suspended bacteria and calibration curves were obtained to quantify the number of active cells in the bionanocomposites.

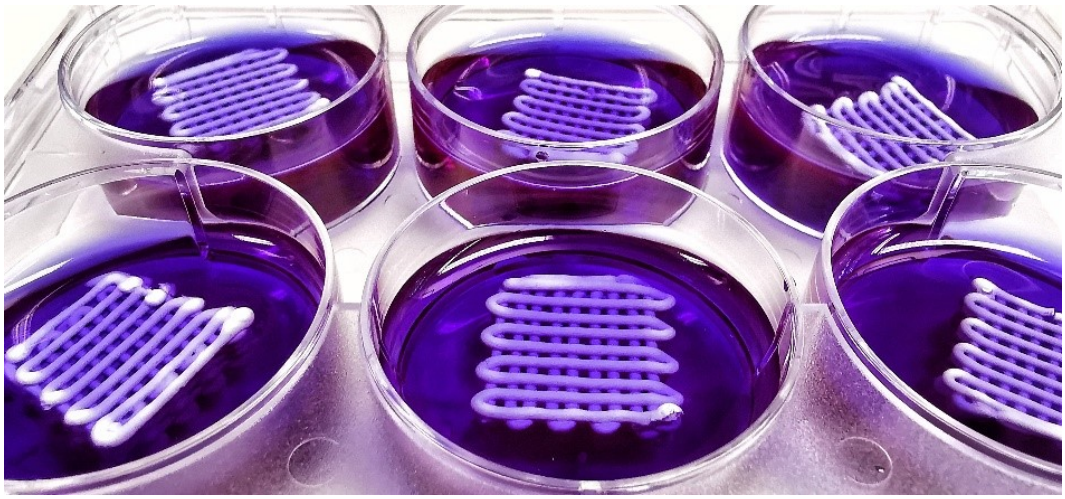

Figure 3.9 – 3D printed samples submerged in resazurin salt solution for bacteria viability measurements.

To determine the influence of alginate and albumin on bacterial viability, freely suspended bacterial were incubated in PBS with different concentrations of alginate (1 wt. %, 0.5 wt. % and 0.25 wt. %), with different concentrations of albumin (7 wt. %, 3.5 wt. % and 1.75 wt. %) or with different concentrations of alginate and albumin together (0.5 and 3.5 wt. % alginate with 0.25 and 1.75 wt. % albumin, respectively). Furthermore, control experiments with cells in PBS or in water were performed as well. For that purpose, bacteria-containing suspensions were then incubated at 37°C and 160 rpm and bacterial viability was determined after 4 h, 24 h and 48 h of incubation in a PBS solution with 10% of resazurin solution stock.

3.10.3 WST-I assay

To confirm the results of viability using the resazurin assay, a similar test was performed using the WST-I assay. This assay is a colorimetric method to define cell viability which is based on the conversion of the tetrazolium salt WST-1 (light pink color) into soluble formazan (orange color). This difference in color by the cells can be measured using a photometer and a correlation of the signal with cell viability can be established. For that, three replicates of samples containing *E. coli* were incubated protected from light for 1 hour, at 37°C, and 160 rpm in a solution of PBS with 10% of WST-I solution stock. Thereafter, absorbance measurements of the supernatant were performed at 450 nm. Previously, a calibration curve was obtained from testing different concentrations of freely suspended bacteria as well. Furthermore, a control test of nanocomposites without bacteria was performed as well to eliminate any influence of the material in both measurements (resazurin and WST-I assay).

3.10.4 Glucose consumption

To characterize immobilized bacteria, samples were incubated into glucose solutions and the change of glucose concentration over time was measured and related to bacteria viability and metabolic activity. This technique could also be used to characterize the reutilization of immobilized bacteria by repeating the experiment several cycles. Thus, samples were positioned inside a chamber of a 6-well plate directly after the external cross-linking with calcium chloride. The chamber of the well plate was afterwards filled with 3 mL of sterile glucose solution, with an initial concentration of 1 mg/mL. These plates were covered and partially closed with Parafilm, to ensure oxygen diffusion into the chamber. Three replicates from different suspension batches of nanocomposite containing *E. coli*, *E. coli* with LB medium, *B. subtilis* and *B. subtilis* with LB medium were tested. Controls containing freely suspended bacteria and nanocomposites without bacteria were also tested. Samples in contact with the glucose solution were incubated in the 6-well plate

in a shaker at 37°C and 140 rpm and the glucose concentration was measured each hour for 24 h. Small amounts (7.5 µL) of the solution were taken out each hour and were mixed with the enzymatic assay Glucose Liquicolor in 96-well plate. The absorbance was measured at 500 nm to define the glucose concentration. In the case of the cyclic tests, the samples were rigorously washed with PBS after each cycle (24h) to remove free bacteria and remaining glucose. Subsequently, the bionanocomposites were dried for 20 min and then transferred into fresh glucose media, with a concentration of 1 mg/mL. This procedure was repeated until less than 50% of glucose was consumed. For the storage test, three samples from different batches were removed from refrigerator every 5 days and tested for 24 h, up to day 60. The samples were not submerged in buffer solution during storage.

3.11 References

1. Condi Mainardi, J., K. Rezwan, and M. Maas, *Embedding live bacteria in porous hydrogel/ceramic nanocomposites for bioprocessing applications.* Bioprocess and Biosystems Engineering, 2019. 42(7): p. 1215-1224.
2. Condi Mainardi, J., et al., *3D bioprinting of hydrogel/ceramic composites with hierarchical porosity.* Journal of Materials Science, 2022. 57(5): p. 3662-3677.
3. Condi Mainardi, J., K. Rezwan, and M. Maas, *Genipin-crosslinked chitosan/alginate/alumina nanocomposite gels for 3D bioprinting.* Bioprocess and Biosystems Engineering, 2022. 45(1): p. 171-185.
4. O'Connell, C., et al., *Characterizing Bioinks for Extrusion Bioprinting: Printability and Rheology*, in *3D Bioprinting: Principles and Protocols*, J.M. Crook, Editor. 2020, Springer US: New York, NY. p. 111-133.
5. Moreno, R., *Rheology*, in *Encyclopedia of Materials: Science and Technology*, E.S. Ltd, Editor. 2001. p. 8192 - 8197.
6. Joyner , H.S. and C.R. Daubert, *Rheological Principles for Food Analysis*, in Food Analysis, S.S. Nielsen, Editor. 2017, Springer International Publishing: Cham. p. 511-527.
7. Liu, S. and J.H. Masliyah, *Rheology of Suspensions*, in Suspensions: Fundamentals and Applications in the Petroleum Industry. 1996, American Chemical Society. p. 107-176.
8. Struble, L.J. and X. Ji, *Rheology*, in Handbook of Analytical Techniques in Concrete Science and Technology, V.S. Ramachandran and J.J. Beaudoin, Editors. 2001, William Andrew Publishing: Norwich, NY. p. 333-367.

9. Paxton N, Smolan W, Böck T, Melchels F, Groll J, Jungst T. *Proposal to assess printability of bioinks for extrusion-based bioprinting and evaluation of rheological properties governing bioprintability*. Biofabrication. 2017;9(4):044107.

10. Hölzl, K., et al., *Bioink properties before, during and after 3D bioprinting.* Biofabrication, 2016. 8(3): p. 032002.

11. Malkin, A.Y. and A.I. Isayev, *2 - VISCOELASTICITY*, in *Rheology Concepts, Methods, and Applications (Second Edition)*, A.Y. Malkin and A.I. Isayev, Editors. 2012, Elsevier: Oxford. p. 43-126.

12. Maas, M., et al., *Towards the synthesis of hydroxyapatite/protein scaffolds with controlled porosities: Bulk and interfacial shear rheology of a hydroxyapatite suspension with protein additives*. Journal of Colloid and Interface Science, 2013. 407: p. 529-535.

13. Kloek, W., T. van Vliet, and M. Meinders, *Effect of Bulk and Interfacial Rheological Properties on Bubble Dissolution.* Journal of Colloid and Interface Science, 2001. 237(2): p. 158-166.

14. Studart, A.R., et al., *Processing Routes to Macroporous Ceramics: A Review.* Journal of the American Ceramic Society, 2006. 89(6): p. 1771-1789.

15. Petkova, B., et al., *Foamability of aqueous solutions: Role of surfactant type and concentration.* Advances in Colloid and Interface Science, 2020. 276: p. 102084.

16. Maas, M., et al., *Towards the synthesis of hydroxyapatite/protein scaffolds with controlled porosities: Bulk and interfacial shear rheology of a hydroxyapatite suspension with protein additives.* Journal of Colloid and Interface Science, 2013. 407: p. 529-535.

17. Boularaoui, S., et al., *An overview of extrusion-based bioprinting with a focus on induced shear stress and its effect on cell viability.* Bioprinting, 2020. 20: p. e00093.

18. Ouyang, L., et al., *Effect of bioink properties on printability and cell viability for 3D bioplotting of embryonic stem cells.* Biofabrication, 2016. 8(3): p. 035020.

19. Van Meerbeek, B., et al., *Microscopy investigations*. Techniques, results, limitations. Am J Dent, 2000. 13(Spec No): p. 3d-18d.

20. Ebnesajjad, S., *Chapter 4 - Surface and Material Characterization Techniques*, in *Surface Treatment of Materials for Adhesive Bonding (Second Edition)*, S. Ebnesajjad, Editor. 2014, William Andrew Publishing: Oxford. p. 39-75.

21. Rost, F., *Fluorescence Microscopy, Applications*, in *Encyclopedia of Spectroscopy and Spectrometry (Third Edition)*, J.C. Lindon, G.E. Tranter, and D.W. Koppenaal, Editors. 2017, Academic Press: Oxford. p. 627-631.

22. Zulkifli, S.M., et al. *High-res 3D X-ray microscopy for non-destructive failure analysis of chip-to-chip micro-bump interconnects in stacked die packages*. in 2017 IEEE 24th International Symposium on the Physical and Failure Analysis of Integrated Circuits (IPFA). 2017.

23. Lichtman, J.W. and J.-A. Conchello, *Fluorescence microscopy*. Nature Methods, 2005. 2(12): p. 910-919.

24. Magidson, V. and A. Khodjakov, *Chapter 23 - Circumventing Photodamage in Live-Cell Microscopy*, in *Methods in Cell Biology*, G. Sluder and D.E. Wolf, Editors. 2013, Academic Press. p. 545-560.

25. Lovitt, R.W. and C.J. Wright, *MICROSCOPY | Light Microscopy*, in *Encyclopedia of Food Microbiology (Second Edition)*, C.A. Batt and M.L. Tortorello, Editors. 2014, Academic Press: Oxford. p. 684-692.

26. Rosenberg, M., Azevedo, N.F. & Ivask, A. *Propidium iodide staining underestimates viability of adherent bacterial cells*. Sci Rep 9, 2019, 6483.

27. Goldstein, G. I.; Newbury, D. E.; Echlin, P.; Joy, D. C.; Fiori, C.; Lifshin, E.. *Scanning electron microscopy and X-ray microanalysis*. New York: Plenum Press. 1981 ISBN 978-0-306-40768-0.

28. *Characterizing Structure, Defects, and Chemistry*, in *Ceramic Materials: Science and Engineering*. 2007, Springer New York: New York, NY. p. 154-177.

29. *Principles of SEM*, in *Principles and Practice of Variable Pressure/Environmental Scanning Electron Microscopy (VP-ESEM)*. 2008. p. 17-62.

30. Cerepi, A., L. Humbert, and R. Burlot, *Pore-Scale Complexity of a Calcareous Material by Time-Controlled Mercury Porosimetry*, in *Studies in Surface Science and Catalysis*, K.K. Unger, G. Kreysa, and J.P. Baselt, Editors. 2000, Elsevier. p. 449-458.

31. Washburn, E.W., *The Dynamics of Capillary Flow.* Physical Review, 1921. 17(3): p. 273-283.

32. Nakanishi, K., *Porosity Measurement*, in *Handbook of Sol-Gel Science and Technology*, L. Klein, M. Aparicio, and A. Jitianu, Editors. 2016, Springer International Publishing: Cham. p. 1-11.

33. Tariq, F., et al., *Characterization of hierarchical pore structures in ceramics using multiscale tomography.* Acta Materialia, 2011. 59(5): p. 2109-2120.

34. Emily Baird, Gavin Taylor, *X-ray micro computed-tomography*, Current Biology, Volume 27, Issue 8, 2017, Pages R289-R291, ISSN 0960-9822,.

35. Katsevich, A., *Theoretically Exact Filtered Backprojection-Type Inversion Algorithm for Spiral CT.* SIAM Journal on Applied Mathematics, 2002. 62(6): p. 2012-2026.

36. Robinson, N. and C. D'Agostino, *NMR Investigation into the Influence of Surface Interactions on Liquid Diffusion in a Mesoporous Catalyst Support.* Topics in Catalysis, 2020. 63(3): p. 319-327.

37. Di Tullio, V., D. Capitani, and N. Proietti, *Unilateral NMR to study water diffusion and absorption in stone-hydrogel systems.* Microporous and Mesoporous Materials, 2018. 269: p. 180-185.

38. Bloch, F., *Nuclear Induction.* Physical Review, 1946. 70(7-8): p. 460-474.

39. Argentieri, E.C., et al., *3 - Magnetic Resonance Imaging of the Knee: Conventional and Novel Techniques*, in *Evidence-Based Management of Complex Knee Injuries*, R.F. LaPrade and J. Chahla, Editors. 2022, Elsevier: Philadelphia. p. 29-49.

40. Dale, B.M., Brown, M.A. and Semelka, R.C. (2015). Production of net magnetization. Chater 1-4 in MRI Basic Principles and Applications (eds B.M. Dale, M.A. Brown and R.C. Semelka)

41. Weiger, M. and K.P. Pruessmann, *MRI with Zero Echo Time*, in *eMagRes*. 2012.

42. Nehlig, A. and A. Obenaus, *Chapter 47 - Imaging Approaches in Small Animal Models*, in *Models of Seizures and Epilepsy*, A. Pitkänen, P.A. Schwartzkroin, and S.L. Moshé, Editors. 2006, Academic Press: Burlington. p. 583-600.

43. Coico, R., *Gram Staining*. Current Protocols in Microbiology, 2006 00: A.3C.1-A.3C.2.

44. Hwang, Y.J., et al., *Effect of genipin crosslinking on the optical spectral properties and structures of collagen hydrogels*. ACS Appl Mater Interfaces, 2011. 3(7): p. 2579-84.

45. Fessel, G., et al., *Dose- and time-dependent effects of genipin crosslinking on cell viability and tissue mechanics – Toward clinical application for tendon repair*. Acta Biomaterialia, 2014. 10(5): p. 1897-1906.

4

Embedding live bacteria in porous hydrogel/ceramic nanocomposites

4.1 Introduction

Chapter 4 has been adapted from Bioprocess and Biosystems Engineering, 2019 - 42(7): p. 1215-1224 (DOI: 10.1007/s00449-019-02119-4) with permission from Springer Nature number 5265951472044 [1].

Immobilizing bacteria or other microorganisms inside semi-permeable substrates can be desirable for biotechnological processes like wastewater treatment [2-4], fermentation of sugars [5-8] or manufacturing of nutritional [9] and pharmaceutical products [10, 11]. However, embedding living microorganisms in artificial materials necessitate the use of both biocompatible starting materials as well as fully biocompatible processing steps. For that reason, bacteria are frequently encapsulated in hydrogels to simplify the process of separation and purification [12-15]. Furthermore, immobilized bacteria are more strongly protected from toxic substances and adverse surroundings and were shown to exhibit higher activity under some circumstances [16, 17]. Especially alginates are widely used for microorganism immobilization because of their biocompatible gelation reaction, which takes place at room temperature and at physiological pH [18-20]. However, alginate hydrogels can hardly meet the mechanical requirements for the harsh conditions that are often present in bioreactors [21]. Furthermore, the fabrication of complex shapes with a combination of advanced material properties like macro porosity and structural stability is difficult to achieve with soft polymer gels.

To overcome common limitations of hydrogels, several strategies focus on hybrid materials consisting of combinations of hydrogels and inorganic materials [22-24]. In this respect, ceramic nanoparticles like alumina are widely known for their high hardness, chemical inertness, and high biocompatibility [25, 26]. The combination of organic and inorganic materials can enhance a range of properties, resulting in the emergence of unique and novel features [27]. However, producing a nanocomposite hydrogel with mechanical stability and bioactivity is still a challenge [28, 29]. Particularly, the presence of living microorganisms restricts some processing routes and parameters, since cell survival requires mild pH, moderate temperature, and low shrinkage of the composite matrix. Furthermore, it is essential that nutrients are able to reach the microorganisms inside the material.

This study aims to develop a biocompatible strategy for synthesizing ceramic/hydrogel nanocomposites in which live bacteria can be embedded. Several factors can potentially

influence the viability of embedded cells, such as preparation conditions, type of cell, residual water content, storage conditions [1] and accessibility of nutrients. Furthermore, a matrix with structural rigidity assures stability of both the overall material as well as of the pore structure. For this reason, a straightforward one-pot processing route based on the reinforcement of an alginate hydrogel with alumina nanoparticles, followed by the addition of bacteria and subsequent internal/external ionotropic gelation steps is developed. The immobilization of gram-negative (*E. coli*) and gram-positive (*B. subtilis*) model bacteria in an alginate structure during gelation is expected to provide a suitable environment for bacteria since this structure possesses high water content and good biocompatibility. Moreover, alumina nanoparticles are used as a reinforcement to increase structural stability of the porous hydrogel matrix while shrinkage is reduced. All bionanocomposites are characterized concerning their pore window size, open porosity, shrinkage, and water content. Compression tests are performed to determine the influence of alumina nanoparticles and the gelation process on structural stability. Furthermore, bacterial viability and activity inside the composites are determined by measuring glucose consumption over time and the long-term performance and stability of the bionanocomposites are also characterized.

4.2 Fabrication of bionanocomposites

The suspension was prepared based on Brandes et al. [30, 31] but under sterile conditions. A mixture of both alginates (Alginic acid sodium salt from brown algae - medium viscosity from Sigma Aldrich Chemie GmbH with product Number.: A2033, and sodium alginate Protanal LFR 5/60 from FMC Biopolymer) were dissolved in 50 mL millipore water at room temperature (RT) via a dispermat (IKA RW20.n, Staufen, Germany) for 30 min at 600 rpm. After dissolving the alginates, the alumina powder was slowly added into the prepared alginate-containing aqueous suspension under continuous stirring at 1200 rpm for 30 min at RT, resulting in agglomerate-free alumina suspension with 40 vol.% of ceramic particles. The suspension could directly be used for bionanocomposite formation or stored in a refrigerator at 4°C for up to 3 weeks. After removal from storage at 4°C, the suspensions were stirred for five minutes at 1200 rpm in sterile conditions, followed by the addition of calcium carbonate salt (product number: 795445 from Sigma Aldrich Chemie GmbH) (Figure 4.1). In order to test the effect of nutrient addition during bionanocomposite processing, two different compositions were produced: with LB medium and without. Therefore, for the samples with LB medium 2 mL of the sterile nutrient solution was added in this step to the slurry, before the bacteria. After the suspension was homogenized by stirring, stirring velocity was decreased to 400 rpm

and the bacteria solution in PBS was added to the mixture, followed by intense stirring at 1000 rpm for 30 s. Thereafter, gluconic acid (product number: G1951 from Sigma Aldrich Chemie GmbH) was added into the dispersion to initiate the internal crosslinking. Gluconic acid dissociates calcium carbonate, releasing calcium cations which are then able to cross-link alginate. A molar ratio of 1:2 calcium carbonate : gluconic acid was used to maintain a neutral pH value [32, 33]. This suspension was mixed at 1200 rpm for 20 s. Subsequently, the suspension was cast at RT into small petri dishes (Ø 35 mm), which were covered and half closed with Parafilm to avoid drying and stored in an incubator for crosslinking at 37°C for 24h. After 24h the samples were removed from the incubator and directly tested or further stored in a refrigerator at 4°C. The external gelation was performed just before the glucose uptake experiments to increase structural stability. The samples were submerged separately in a sterile 0.1 M $CaCl_2$ solution for 30 min. After that, the samples were rigorously washed in PBS and were dried for 20 min.

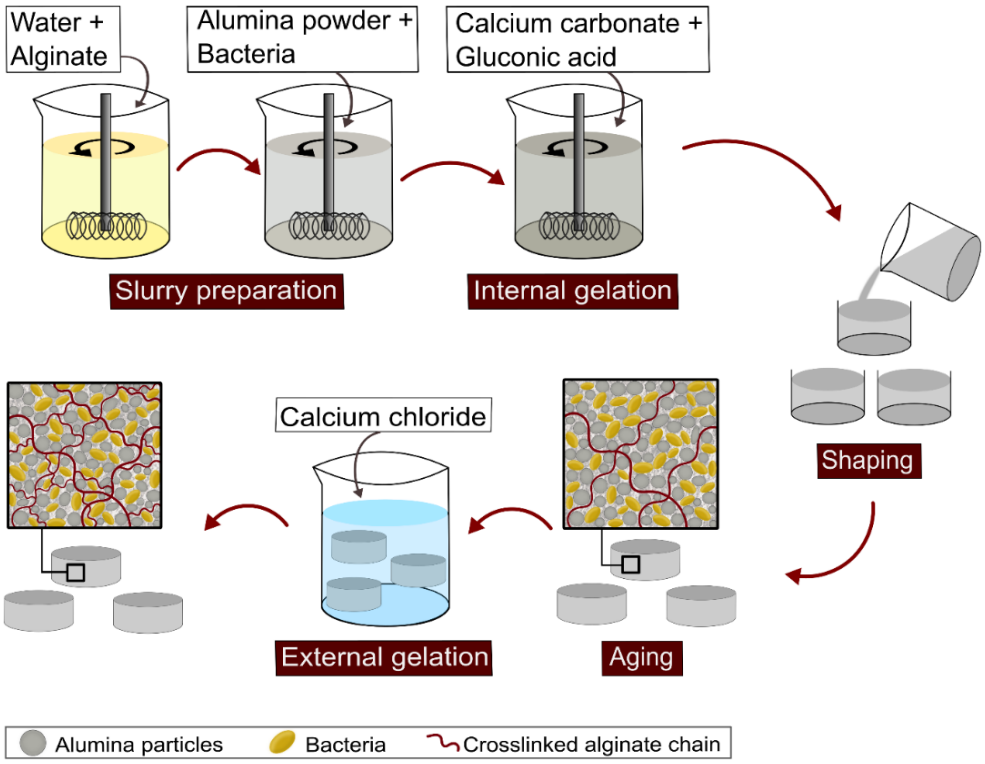

Figure 4.1 – Scheme illustrating the bionanocomposite processing route based on ionotropic gelation. First alginates are dissolved in water followed by the addition of alumina powder. After homogenization of the mixture, microorganisms can be incorporated into the suspension and thereafter internally gelled and cast. To assure sample mechanical stability an external gelation was performed before the samples were tested.

4.3 Results and discussion

4.3.1 Structure characteristics

The ceramic/hydrogel nanocomposites were prepared in small petri dishes (d = 35 mm) which defined their cylindrical shape (Figure 4.1). Alumina particles, which are positively charged at physiological pH, electrostatically interact with alginate chains, which are negatively charged. The alginate/particle suspension was afterward crosslinked with Ca^{2+} cations and the combination of these interactions resulted in white composite gels which maintained their overall shape and could be handled without damage for the successive testes. The composites were dehydrated by a graded series of ethanol to characterize porosity and pore size, while different samples were dried at room conditions and their weight loss was measured to define shrinkage and water content (Table 4.1). Here, an open porosity of around 46% with a pore window size of 0.14 µm was observed. Additionally, the wet sample contained ca. 54 vol.% of internal water and showed a shrinkage of ca. 7.4% after aging. Samples containing the bacteria *E. coli* or *B. subtilis*, which are called bionanocomposite in this study, were also prepared and characterized. The bionanocomposites did not show any significant change in water content, shrinkage, or pore size. However, the porosity slightly increased with both bacteria, which might be related to the bacteria population.

Long-term material stability was indirectly measured by determining the weight loss of the composites after a certain time in PBS buffer or water, with and without external gelation, at a temperature of 37°C and 140 rpm. These results are shown in Figure 4.2. Nanocomposites without external gelation incubated in PBS were stable for less than 24 h. External gelation could extend the stability of the nanocomposites which were completely degraded after nine days. This low stability of alginate in PBS was noted by several authors [34-37] as a result of calcium exchange with buffer ions, resulting in the decalcification of the gel and consequently destabilization. No significant degradation was observed with the nanocomposites submerged in water. Overall, the long-term stability of the samples was sufficient compared to the lifetime of the encapsulated bacteria under the real experimental conditions.

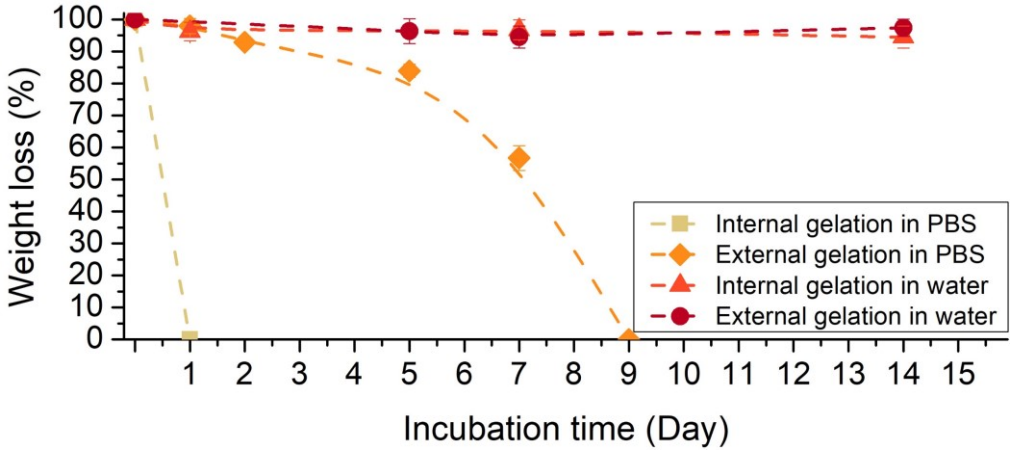

Figure 4.2 - Measurement of nanocomposite stability in water or PBS with and without external gelation.

Table 4.1 – Structural properties of the bionanocomposite.

Bionanocomposite	Porosity (%)	Pore window size (μm)	Shrinkage (Vol. %)	Water content (Vol. %)
without bacteria	46 ± 1.2	0.14 ± 0.01	7.4 ± 0.9	54 ± 0.8
with *E. coli*	49 ± 4.8	0.13 ± 0.01	7.9 ± 0.7	53 ± 0.7
with *B. subtilis*	50 ± 1.7	0.14 ± 0.01	6.9 ± 0.9	55 ± 0.8

4.3.2 Mechanical properties

The mechanical properties of hydrogels can be a critical limitation for these materials in different applications. Here, the composites were initially produced via internal gelation followed by a second crosslinking (external gelation) to achieve sufficient mechanical strength. For mechanical testing, the samples were first submerged in 0.1 M $CaCl_2$ solution for 30 min. Compression tests were performed to evaluate the influence of the gelation steps as well as the mechanical reinforcement of the hydrogel by the addition of ceramic nanoparticles.

The compressive strength and the elastic modulus (Young's modulus) of the bacteria-free hydrogel after internal gelation and after the combination of internal and external gelation, with and without the addition of ceramic particles are presented in Table 4.2 and Figure 4.3. Internally-gelled alginate hydrogels are capable of high deformation (approx. 40%) but this material shows low elastic modulus (1.5 ± 0.3 KPa) and fails at low compressive strength (33.9 ± 4.9 KPa). A subsequent external gelation resulted in a similar elastic modulus (1.7 ± 0.1 KPa) and a slightly higher compressive strength (44.6 ± 3.7 KPa). This means that the gel matrix, with or without external gelation, can be easily deformed but

does not support high compressive strength. However, adding alumina nanoparticles to the internally-gelled composite increased the elastic modulus twofold (3.6 ± 0.2 KPa), resulting in a stiffer material. This material reached the maximum compressive strength (59.4 ± 2.6 KPa) at smaller deformation (approx. 20%). After reaching maximum strength, the material started to fail and deform up to 40%. The compressive strength of the hydrogel/ceramic composites increases to 132.9 ± 5.8 KPa with a subsequent external gelation. Moreover, external gelation increased the elastic modulus to 8.4 ± 0.3 KPa and the material failed at lower deformation (approx. 20%). The combination of internal and external gelation with alumina nanoparticles, which are only electrostatic interactions, reinforced the compressive strength by a factor of about four and also increased elastic modulus six times. This strong structural reinforcement might be caused by the interaction between ceramic particles and polymer chains, which might facilitate the diffusion of Ca^{2+} into the composite during external gelation, crosslinking the inner parts of the composite beyond the surface.

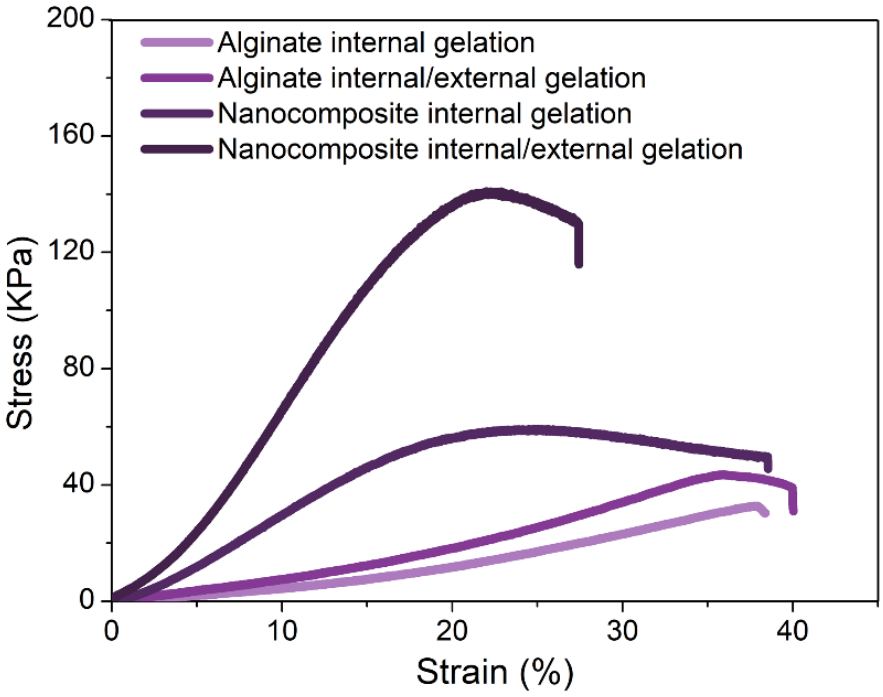

Figure 4.3 – Compression test of the cylindrical samples showing the influence of the reinforcement and combination of internal and external gelation of the gel on the compression strength.

Table 4.2 – Compressive strength and elastic modulus of the hydrogel after internal gelation and after the combination of internal and external gelation, with and without the addition of ceramic particles.

	Compressive strength (KPa)	Elastic modulus (KPa)
Alginate - internal gelation	33.9 ± 5.0	1.5 ± 0.3
Alginate - internal/external gelation	44.6 ± 3.7	1.7 ± 0.1
Nanocomposite - internal gelation	59.4 ± 2.6	3.6 ± 0.2
Nanocomposite - internal/external gelation	132.2 ± 5.8	8.4 ± 0.3

4.3.3 Bacterial viability

Bacterial activity can be observed in all bacteria-containing samples, while negative controls did not show any significant levels of resorufin (Figure 4.4 and Figure 4.5). For both *E. coli* and *B. subtilis* containing samples, only approximately 10% of bacteria were still viable after bionanocomposite processing. However, after initial processing, the samples were kept in an incubator for 24 h before testing for aging. This period of time could have been detrimental for the bacteria even without any material processing. Therefore, freely suspended bacteria viability was measured after 24 h to determine the influence of the storage time on bacteria viability. For that, bacteria were kept in an incubator for 24 h in PBS solution. The aging reduced approx. 15% of *E. coli* viability and 85% *B. subtilis* viability. Based on these results, freely suspended *B. subtilis* and the bionanocomposite containing the same bacteria showed similar viability, which indicates that the material processing itself might not have strongly influenced *B. subtilis* viability. However, opposite behavior was observed with *E. coli*. In this case, immobilized *E. coli* showed approx. 80% less viable cells than freely suspended bacteria after 24 h, showing that the processing was more detrimental for *E. coli*.

The effect of the addition of LB medium during nanocomposite processing on bacteria viability was also analyzed. Here, LB medium increased cell viability in a factor of approx. 5.8 ± 0.29 for *E. coli* and 3.6 ± 0.3 for *B. subtilis*. The nutrients provide a suitable environment and supply the cells during the aging process. The differences between *E. coli* and *B. subtilis* are related to the specific metabolism characteristics of each microorganism. These differences also highlight the importance of working with model bacteria of the two different groups.

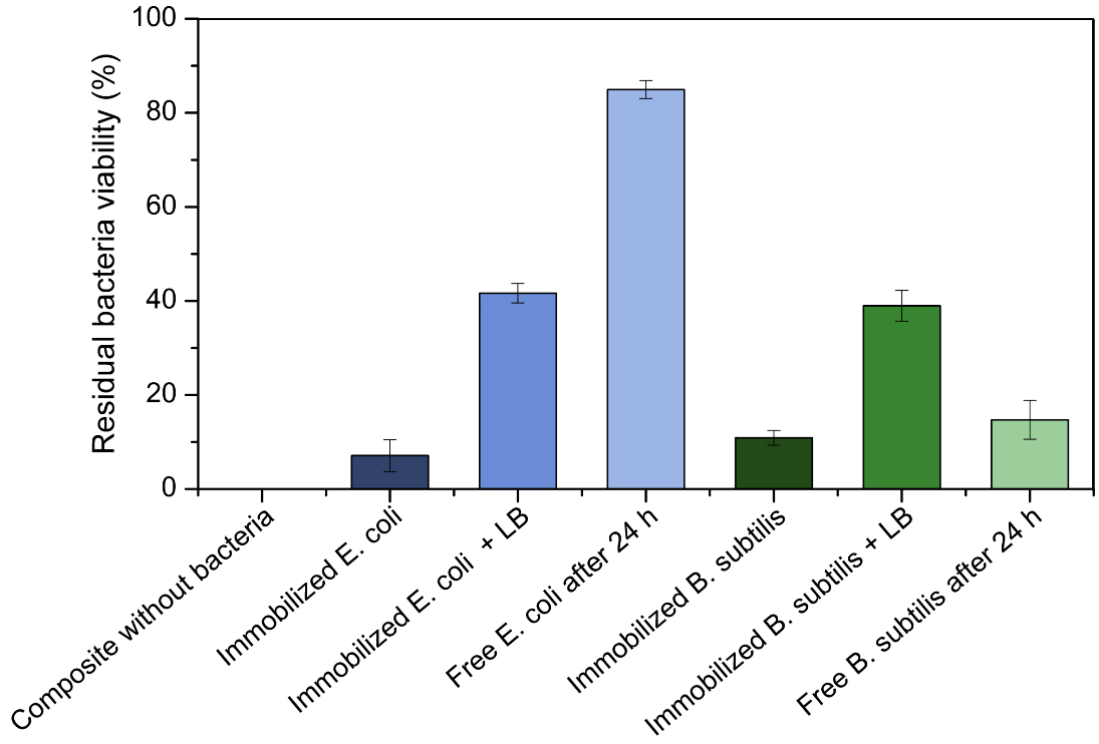

Figure 4.4 – Viability test of embedded *E. coli* (a) and *B. subtilis* (b) and freely suspended bacteria after 24 h at 37°C in comparison to initial bacterial concentration. The influence of additional nutrients (LB medium) on the bionanocomposite was also analyzed.

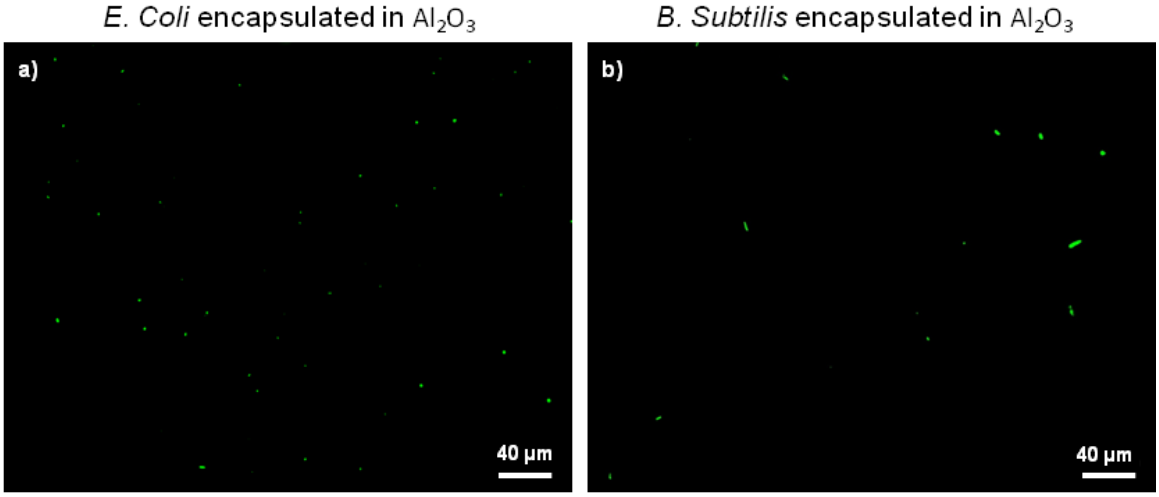

Figure 4.5 – Fluorescence microscopy images showing viability of encapsulated *E. coli* (a) and *B. subtilis* (b) cells in the nanocomposite using Live/Dead staining (green stains living cells, red stains dead cells). The figure shows both green and red channels of the microscope, only living cells are observed.

4.3.4 Influence of immobilization on bacterial metabolism

The immobilization of bacteria in an inorganic structure protects them by preventing direct contact with the potentially harmful environment. However, the structure can also hinder nutrients to reach the cell, leading to cell death. Therefore, glucose consumption of the embedded cells was measured to determine if the bacteria were active and accessible inside the bionanocomposite. For that, three replicates of different batches were tested in order to evaluate the performance of *E. coli* and *B. subtilis*, free and immobilized, as well as a negative control without bacteria towards their ability to consume glucose, which is a simple indicator for bacterial viability. These samples were incubated for 24 h and the glucose concentration was measured each hour (Figure 4.6).

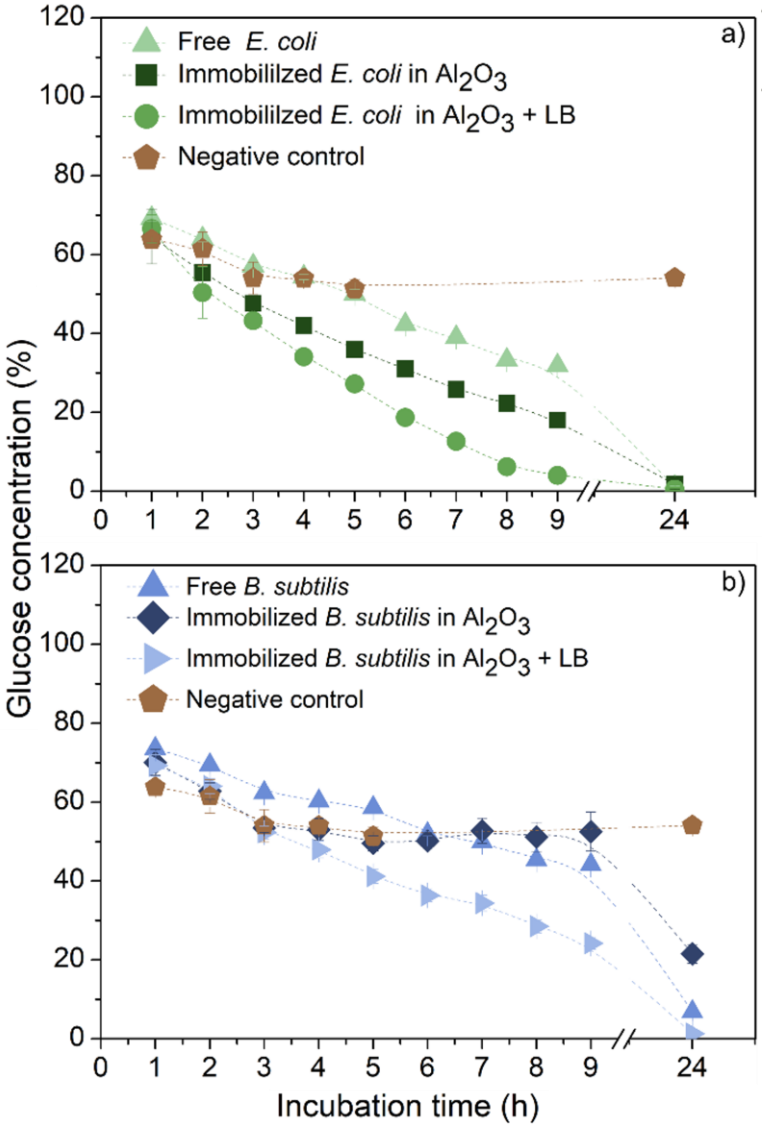

Figure 4.6 – Glucose uptake from freely suspended and embedded *E. coli* (a) and *B. subtilis* (b) as a function of time. The influence of additional nutrients (LB medium) on the bionanocomposite was also analyzed.

As shown in Figure 4.6, all samples demonstrated some reduction in glucose concentration. Samples containing immobilized *E. Coli* or *B. subtilis*, as well as freely suspended bacteria, exhibited an almost linear glucose consumption over incubation time. Comparing the consumption curves for *E. Coli* and *B. Subtilis*, it is possible to observe a higher inclination of the curve for *E. Coli*, which corresponds to a higher glucose consumption. However, the negative control without bacteria also showed a slight reduction in glucose concentration. This might be related to the residual internal water content (approx. 54 vol.%) of the nanocomposites, which were never completely dried to ensure the survival of the embedded bacteria. In the absence of bacteria, dilution of glucose into the water inside the nanocomposite might occur, resulting in the observed initial reduction of the glucose concentration. However, with samples containing bacteria, only small amounts (or no glucose for *E. coli*) were detected after 24 h. Nevertheless, immobilized bacteria showed a higher glucose uptake than free bacteria at comparable bacteria concentrations. This observation might again be related to the internal water content of the samples, which dilutes the glucose in the surrounding medium. Considering this, the behavior of the free and immobilized *E. coli* is similar, with nearly parallel consumption curves.

Additionally, the effect of the addition of nutrients in the form of LB medium during the production of the bionanocomposite was analyzed. The addition of the LB medium resulted in a higher glucose uptake for both bacteria. This improvement might correspond to higher bacterial viability during sample preparation. For *E. coli*, only the initial glucose consumption was faster for samples with LB medium. However, for *B. subtilis*, the addition of LB medium generally increased consumption rates, reducing the glucose concentration at 24 h from 20% to 2%. Accordingly, the nutrients seem to provide a suitable environment and supply the cells during sample processing.

4.3.5 Long-term performance of bionanocomposites

Repeated testing cycles were carried out in order to evaluate bionanocomposite performance after multiple uses (Figure 4.7). For this purpose, after 24 h of glucose consumption with an initial concentration of 1 mg/mL, the bionanocomposites were rigorously washed with PBS to remove any remaining glucose and free bacteria. Subsequently, the composites were dried for 20 min and then transferred into fresh glucose media with a concentration of 1 mg/mL. This procedure was repeated after each 24 h consumption cycle. This was investigated again with and without the addition of LB medium.

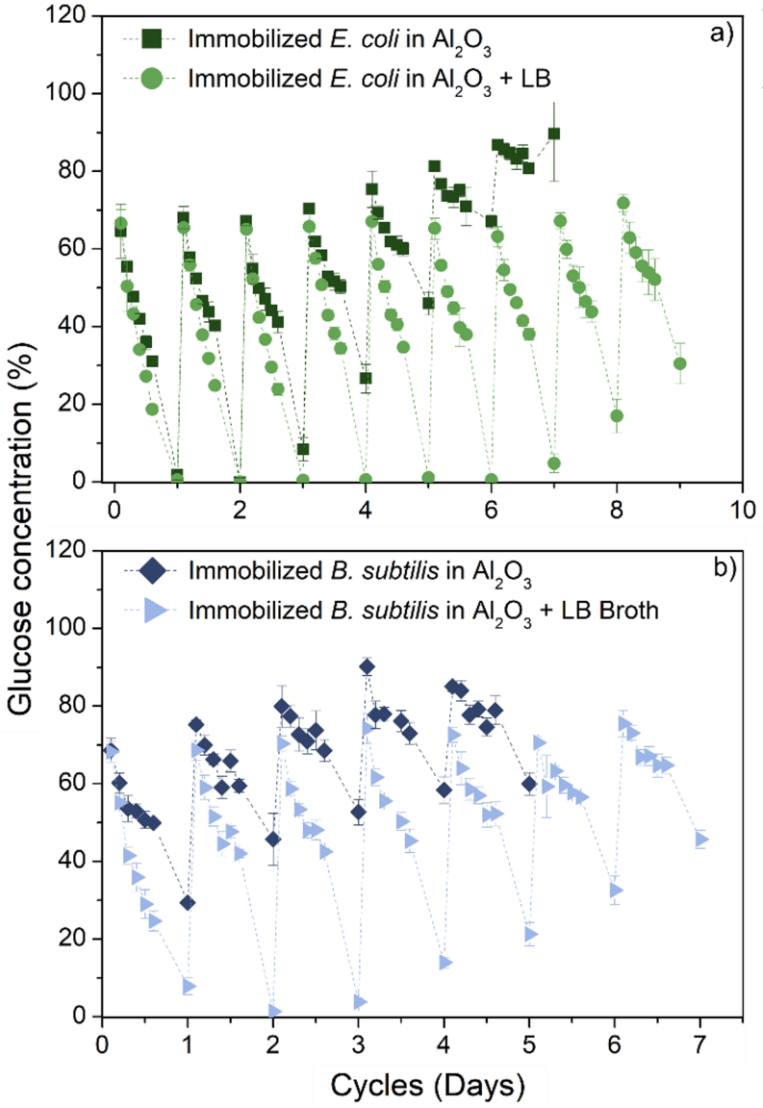

Figure 4.7 – Long-term performance of bionanocomposites with embedded E. coli (a) and B. subtilis (b) with and without the addition of LB medium during several cycles, measured by the glucose concentration over time. Each cycle represents 24h.

Both *E. coli* and *B. subtilis* showed a decrease in cell viability after each cycle. Without the addition of LB medium, samples with *E. coli* could metabolize all glucose within just two cycles and its consumption gradually decreased after each cycle until the sixth day, when almost no glucose was metabolized anymore. In contrast, all glucose could be consumed up to the sixth day when LB medium was added to the composite. Besides that, it took approximately six days longer for the samples with LB medium to show similar residual concentrations of glucose and with that deterioration of their viability as the samples with no medium. Similar tendencies were observed with *B. subtilis*. Accordingly, for both bacteria, the addition of LB medium extended the timeframe for glucose consumption

approximately six times. Based on these results, the long-term performance of the embedded bacteria inside the ceramic during repeated test cycles could be confirmed.

4.3.6 Long-term stability of bionanocomposites

To determine the long-term stability of the bionanocomposites, the embedded bacteria were stored, without being submersed in buffer solution, under sterile conditions at 4°C. Glucose uptake was analyzed every five days with different samples which results are depicted in Figure 4.8. For samples produced with *E. coli*, a reduction of the bioactivity was observed with storage. After 60 days, a remaining glucose concentration of about 20 and 25% was observed for samples with and without the addition of LB, respectively. The associated decrease in glucose consumption likely occurred gradually during storage and might be related to a reduction in the number of live cells. Samples with LB medium had a slightly higher glucose consumption after 60 days than samples without LB medium, the influence of LB medium being less significant for *E. coli*. Nevertheless, a reduction of just 20% of glucose from *E. coli* bioactivity after 60 days is a promising result, since the nanocomposite structure limits cell division or might otherwise negatively affect the microorganisms.

A different behavior was observed for the bionanocomposites with embedded *B. Subtilis*. These samples did not show a reduction in glucose consumption, which might be explained by the capability of *B. Subtilis* to undergo sporulation. Besides that, the influence of LB Broth on cell viability was the same as for the cyclic tests (Figure 4.6), which was constant during all cycles.

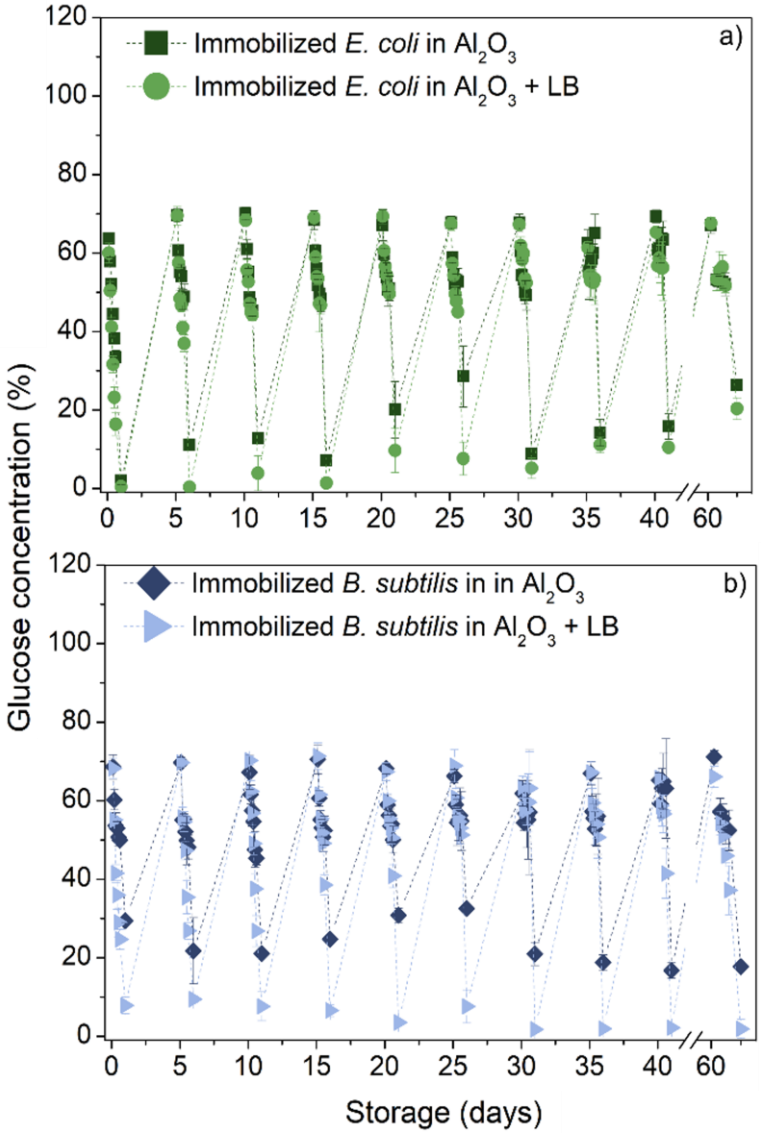

Figure 4.8 – Long-term stability of bionanocomposite with embedded *E. coli* (a) and *B. subtilis* (b) with and without the addition of LB medium stored in a refrigerator, measured by the glucose concentration over time.

4.4 Conclusions

This study showed that ceramic/hydrogel nanocomposites produced by ionotropic gelation are a suitable encapsulation matrix for bacteria. Electrostatic interactions of the negatively charged alginate and the positively charged alumina nanoparticles in combination with internal/external crosslinking increased compression strength four times as well as elastic modulus six times and resulted in a highly stable porous structure with low shrinkage and high-water content. Furthermore, embedded bacteria viability increased approx. five times for *E. coli* and three times for *B. subtilis* by just adding LB medium during processing. In addition, immobilized bacteria showed high glucose consumption which was comparable to non-immobilized cells. Furthermore, adding LB medium to the bionanocomposites also

increased glucose consumption for both bacteria. The long-term performance of immobilized bacteria was examined by performing repeated cycles of glucose consumption. Both bacteria *E. coli* and *B. subtilis* showed a gradual decrease in cell viability after each cycle. For both bacteria, the addition of LB medium extended the timeframe for glucose consumption approximately six times. Moreover, in long-term experiments, the immobilized *E. coli* showed a gradual decrease in cell viability during storage up to a reduction 25% in glucose consumption capacity after 60 days. Conversely, storage did not significantly influence immobilized *B. subtilis* performance for 60 days. These results demonstrate the great potential of this approach for producing bioactive composite materials for applications in bioprocessing.

4.5 References

1. Condi Mainardi, J., K. Rezwan, and M. Maas, *Embedding live bacteria in porous hydrogel/ceramic nanocomposites for bioprocessing applications.* Bioprocess and Biosystems Engineering, 2019. 42(7): p. 1215-1224.
2. Dash, H.R. and S. Das, *Bioremediation of mercury and the importance of bacterial mer genes.* International Biodeterioration & Biodegradation, 2012. 75: p. 207-213.
3. Dixit, R., et al., *Bioremediation of Heavy Metals from Soil and Aquatic Environment: An Overview of Principles and Criteria of Fundamental Processes.* Sustainability, 2015. 7(2): p. 2189-2212.
4. Kang, C.-H., Y.-J. Kwon, and J.-S. So, *Bioremediation of heavy metals by using bacterial mixtures.* Ecological Engineering, 2016. 89: p. 64-69.
5. Han, D., et al., *Bacterial biotransformation of phenylpropanoid compounds for producing flavor and fragrance compounds.* Journal of the Korean Society for Applied Biological Chemistry, 2013. 56(2): p. 125-133.
6. Quintana, M.G. and H. Dalton, *Biotransformation of aromatic compounds by immobilized bacterial strains in barium alginate beads.* Enzyme and Microbial Technology, 1999. 24(3): p. 232-236.
7. Heipieper, H.J., et al., *Solvent-tolerant bacteria for biotransformations in two-phase fermentation systems.* Applied Microbiology and Biotechnology, 2007. 74(5): p. 961-973.
8. Dien, B.S., M.A. Cotta, and T.W. Jeffries, *Bacteria engineered for fuel ethanol production: current status.* Applied Microbiology and Biotechnology, 2003. 63(3): p. 258-266.

9. Leroy, F. and L. De Vuyst, *Lactic acid bacteria as functional starter cultures for the food fermentation industry.* Trends in Food Science & Technology, 2004. 15(2): p. 67-78.
10. Anal, A.K. and H. Singh, *Recent advances in microencapsulation of probiotics for industrial applications and targeted delivery.* Trends in Food Science & Technology, 2007. 18(5): p. 240-251.
11. Huq, T., et al., *Encapsulation of probiotic bacteria in biopolymeric system.* Crit Rev Food Sci Nutr, 2013. 53(9): p. 909-16.
12. Zhang, B.-B., et al., *Robust and Biocompatible Hybrid Matrix with Controllable Permeability for Microalgae Encapsulation.* ACS Applied Materials & Interfaces, 2016. 8(14): p. 8939-8946.
13. Kang, A., et al., *Cell encapsulation via microtechnologies.* Biomaterials, 2014. 35(9): p. 2651-2663.
14. Gombotz, W.R. and S. Wee, *Protein release from alginate matrices.* Advanced Drug Delivery Reviews, 1998. 31(3): p. 267-285.
15. Das, M. and A. Adholeya, *Potential Uses of Immobilized Bacteria, Fungi, Algae, and Their Aggregates for Treatment of Organic and Inorganic Pollutants in Wastewater*, in *Water Challenges and Solutions on a Global Scale*. 2015, American Chemical Society. p. 319-337.
16. Böttcher, H., et al., *Biocers: ceramics with incorporated microorganisms for biocatalytic, biosorptive and functional materials development.* Journal of Materials Chemistry, 2004. 14(14): p. 2176-2188.
17. Martín, M.J., et al., *Microencapsulation of bacteria: A review of different technologies and their impact on the probiotic effects.* Innovative Food Science & Emerging Technologies, 2015. 27: p. 15-25.
18. de Vos, P., et al., *Polymers in cell encapsulation from an enveloped cell perspective.* Advanced Drug Delivery Reviews, 2014. 67-68: p. 15-34.
19. Orive, G., et al., *Cell encapsulation: technical and clinical advances.* Trends in Pharmacological Sciences, 2015. 36(8): p. 537-546.
20. Riddle, K.W. and D.J. Mooney, *Biomaterials for Cell Immobilization*, in *Fundamentals of Cell Immobilisation Biotechnology*, V. Nedović and R. Willaert, Editors. 2004, Springer Netherlands: Dordrecht. p. 15-32.
21. Fedorovich, N.E., et al., *Organ printing: the future of bone regeneration?* Trends in Biotechnology, 2011. 29(12): p. 601-606.
22. Haraguchi, K., *Nanocomposite hydrogels.* Current Opinion in Solid State and Materials Science, 2007. 11(3): p. 47-54.

23. Haraguchi, K., T. Takehisa, and S. Fan, *Effects of Clay Content on the Properties of Nanocomposite Hydrogels Composed of Poly(N-isopropylacrylamide) and Clay.* Macromolecules, 2002. 35(27): p. 10162-10171.
24. Kopecek, J., *Hydrogel biomaterials: a smart future?* Biomaterials, 2007. 28(34): p. 5185-5192.
25. Thamaraiselvi, T. and S. Rajeswari, *Biological Evaluation of Bioceramic Materials - A Review.* Trends in biomaterials & artificial organs, 2004. 18.
26. Warashina, H., et al., *Biological reaction to alumina, zirconia, titanium and polyethylene particles implanted onto murine calvaria.* Biomaterials, 2003. 24(21): p. 3655-3661.
27. Zhao, F., et al., *Composites of Polymer Hydrogels and Nanoparticulate Systems for Biomedical and Pharmaceutical Applications.* Nanomaterials (Basel, Switzerland), 2015. 5(4): p. 2054-2130.
28. Carrow, J.K. and A.K. Gaharwar, *Bioinspired Polymeric Nanocomposites for Regenerative Medicine.* Macromolecular Chemistry and Physics, 2015. 216(3): p. 248-264.
29. Song, F., et al., *Nanocomposite Hydrogels and Their Applications in Drug Delivery and Tissue Engineering.* J Biomed Nanotechnol, 2015. 11(1): p. 40-52.
30. Brandes, C., et al., *Aluminium acetate as alternative cross-linker for temperature controlled gel-casting and joining of ceramics.* Journal of the European Ceramic Society, 2016. 36(5): p. 1241-1251.
31. Brandes, C., et al., *Gel Casting of Free-Shapeable Ceramic Membranes with Adjustable Pore Size for Ultra- and Microfiltration.* Journal of the American Ceramic Society, 2014. 97(5): p. 1393-1401.
32. Kuo, C.K. and P.X. Ma, *Ionically crosslinked alginate hydrogels as scaffolds for tissue engineering: Part 1. Structure, gelation rate and mechanical properties.* Biomaterials, 2001. 22(6): p. 511-521.
33. Growney Kalaf, E.A., et al., *Characterization of slow-gelling alginate hydrogels for intervertebral disc tissue-engineering applications.* Materials Science and Engineering: C, 2016. 63: p. 198-210.
34. Smidsrød, O. and G. Skja˚k-Br৷k, *Alginate as immobilization matrix for cells.* Trends in Biotechnology, 1990. 8: p. 71-78.
35. Groboillot, A., et al., *Immobilization of Cells for Application in the Food Industry.* Critical Reviews in Biotechnology, 1994. 14(2): p. 75-107.
36. Bajpai, S.K. and N. Kirar, *Swelling and drug release behavior of calcium alginate/poly (sodium acrylate) hydrogel beads.* Designed Monomers and Polymers, 2016. 19(1): p. 89-98.

37. Lin, Z., et al., *3D Printing of Mechanically Stable Calcium-Free Alginate-Based Scaffolds with Tunable Surface Charge to Enable Cell Adhesion and Facile Biofunctionalization.* Advanced Functional Materials, 2019. 29(9): p. 1808439.

5

3D bioprinting of hydrogel/ceramic composites with hierarchical porosity

5.1 Introduction

Chapter 5 has been adapted from Journal of Materials Science, 2022 - 57, 3662–3677. (DOI: 10.1007/s10853-021-06829-7) with permission from Springer Nature [1].

The development of new hydrogel compositions and biocompatible crosslinking strategies opened the door to customizing cell-containing materials into complex shapes by 3D bioprinting [2-5]. In order to maintain structural fidelity and mechanical properties, 3D bioprinting research has mainly utilized hydrogel structures with porosity stemming from the microporous polymer mesh. Although the used hydrogels are generally biocompatible, such comparably dense gels often hinder the supply of nutrients and oxygen to the cells [6-8] and limit the migration and proliferation of immobilized cells [9-11]. Consequently, there is a demand for hydrogel materials with hierarchical pore structures including larger interconnected pores that enable effective diffusion of nutrients/oxygen towards the material as well as cell proliferation. At the same time, the materials must exhibit good structural fidelity and adequate mechanical properties.

In the previous Chapter 4, the immobilization of bacteria *E. coli* or *B. subtilis* into rigid alginate/alumina nanocomposites by gel casting with good mechanical properties and high cell viability after 60 days of storage was analyzed. Nevertheless, sample size influences the nutrient exchange where a clear influence could be observed for negative controls, whereas samples took approx. 3 h to stabilize the glucose concentration in the solution due to residual water in the sample [12]. Ideally, structures with incorporated cells require a broad range of pores from nm to mm scales (hierarchical porosity). Small pores (nm scale) are essential for nutrient adsorption/retention as well as for structural support. Middle-sized pores (µm scale) are desired for cell proliferation as well as nutrient diffusion while pores in the mm scale decrease diffusion pathways and therefore enhance permeability of the material and accessibility of embedded cells [13, 14]. Extrusion-based 3D printing results in high amount of mm pores but printing feedstocks that contain large pores is challenging due to potential nozzle blocking, strand breaks, or poor shape fidelity [15, 16].

A detailed characterization of pore size, morphology, interconnectivity and its impact on fluid transport and diffusion within the material are crucial factors for designing porous materials [17]. Particularly modern X-ray computed tomography with submicrometer resolution (µCT) is an advanced imaging technique that has the ability to precisely

visualize pore size/morphology as well as pore interconnectivity of different ceramic, meta,l and polymer materials [17, 18]. Complementary, nuclear magnetic resonance (NMR) tomography, among other things, is able to measure diffusion coefficients of water in porous materials in 3D space based on an evaluation of the volume-averaged diffusivity of the respective molecules. Thus, the combination of X-ray and NMR tomography techniques has the potential to provide a comprehensive picture of the inner structure of a porous material including both the material matrix and the contained fluid [19, 20].

In this chapter, a feedstock for 3D-bioprinting with hierarchical pore structure to minimize mass transport limitations in bioprocessing applications is presented. The bioink is based on Chapter 4 feedstock, which is a highly particle-filled bionanocomposite material containing alginate, alumina nanoparticles and *E. coli* bacteria [12]. To increase the porosity of the printed filaments and to create the hierarchical porosity, different concentrations of the protein ovalbumin were incorporated into the suspension as a foaming agent and the influence of the protein on bulk and interfacial rheology as well as on the printability was analyzed. The porosity of the structure was characterized by µCT along with mercury intrusion porosimetry while the water content in the material based on its porosity and albumin concentration was evaluated by NMR tomography. Furthermore, the influence of the printing process and the material composition on bacterial viability was analyzed.

5.2 Fabrication of bionanocomposites

All colloidal dispersions were prepared under sterile conditions and Figure 5.1 illustrates the processing route. First, a 4.2 wt.% alginate solution was prepared by dissolving 2.1 g alginate (1 g of alginic acid sodium salt from brown algae medium viscosity from Sigma-Aldrich Chemie with product number: A203 and 1.1 g Protanal LFR 5/60 Sodium alginate Protanal LFR 5/60 from FMC Biopolymer) in 50 mL millipore water at room temperature (RT) via a dispermat (IKA RW20.n - Staufen, Germany) using a milk frother from Manufactum (Waltrop, Germany, product number: 27570) as stirring geometry for 30 min at 600 rpm. After total dissolution of alginate, alumina powder (66 vol.%) was slowly added into the alginate solution and was further stirred at 1200 rpm for 20 min for homogenization. Thereafter, the stirring velocity was decreased to 400 rpm and 11 mL of bacteria suspension in PBS was slowly added to the mixture, followed by intense stirring at 1000 rpm for 30 s. Afterward, different albumin powder concentrations were added into the suspensions, resulting in suspensions with final concentrations of 2, 4.5 and 7 wt.% albumin. A feedstock without albumin was also produced for comparison. Successively,

the suspensions with and without albumin were intensively stirred for two minutes at 1200 rpm with the milk frother stirrer for air incorporation and thereafter they were either printed or gel cast.

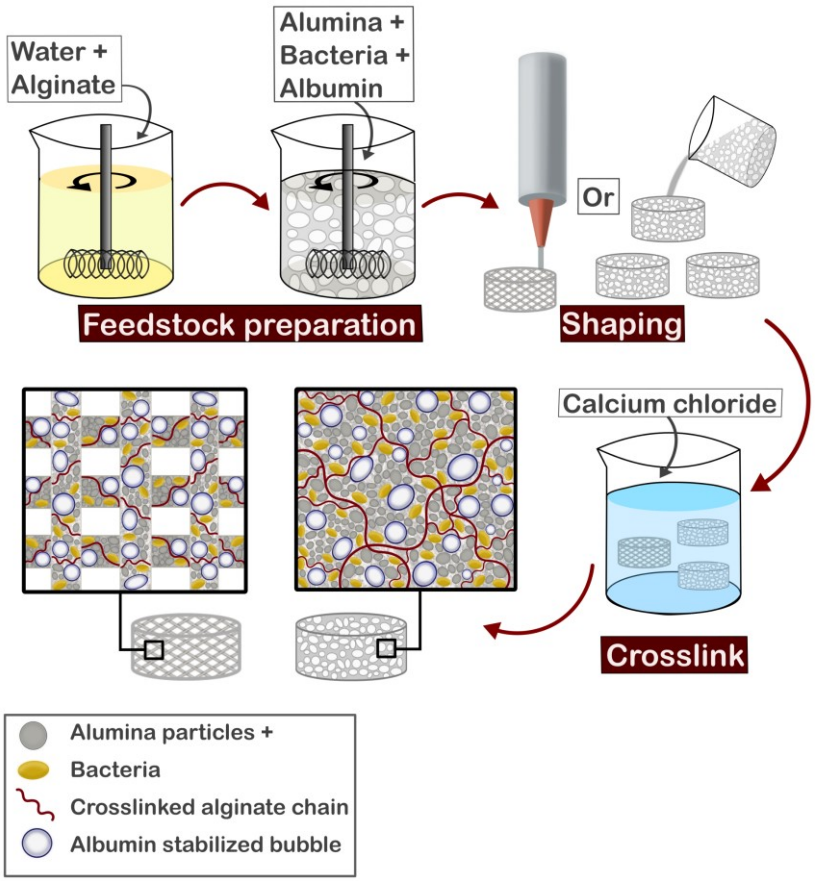

Figure 5.1 – Scheme illustrating the bionanocomposite processing route based on ionotropic gelation. First, alginate is dissolved in water followed by the addition of alumina powder and microorganisms to produce the feedstock. After homogenization of the mixture, ovalbumin is incorporated into the feedstock and a foam is produced by air incorporation. Thereafter, the suspensions are cast into the desired shape by either 3D printing or gel casting. Lastly, the samples are submersed in a calcium chloride solution for crosslinking.

Bionanocomposite suspensions were printed with the 3D bioprinter Inkredible from Cellink – Gothenburg, Sweden, which is a pneumatic-based extrusion printer. First, 3 mL cartridges from Nordson (Erkrath, Germany) were filled with alginate/alumina suspensions with or without albumin. Lattice cuboids (1.5 x 1.5 x 0.5 mm) with a 90° grid structure were printed using conical precision tip nozzles (Ø 940 µm) from Techcon (Eastleigh Hampshire, United Kingdom) with an air pressure of 45 ± 5 kPa and a printing speed of 10 mm/s. The numerical code with the printing commands was generated using the Cellink Heartware 2.4.1 software, with a 67% infill density and 0.85 mm layer height, with

exception of the first layer, which had 0.7 mm height to assure a better contact between feedstock and substrate. Additionally, the printing settings were maintained constant during the whole printing procedure and were the same for all printed samples. Conversely, gel-cast samples were produced by pouring the suspension on a petri dish and slicing it into 2 x 1.5 x 0.5 mm cuboids. After shaping, gel-cast and printed samples were crosslinked for 8 min with a 0.5 M calcium chloride by dropping the solution onto the samples. Thereafter, samples were rigorously washed with PBS to stop the crosslinking.

5.3 Results and discussion

5.3.1 Bulk rheology

The rheological properties are critical for controlling printability and shape fidelity of the feedstock formulations. In this study, we characterized the rheological properties of the feedstock to obtain information about its behavior before, during, and after the printing process for all different concentrations of albumin. First, a shear rate ramp test was performed to analyze flow initiation and the material's yield stress (Figure 5.2 – a). The yield point of the feedstocks was approx. 690 Pa, 460 Pa, 400 Pa and 220 Pa for samples with 0 wt.%, 2 wt.%, 4.5 wt.% and 7 wt.% albumin, respectively. A sufficiently high yield point ensures that the material acts like a solid in a steady state and only starts to flow after a suitable stress is applied.

Shear rate tests were performed to analyze the material's flow behavior (Figure 5.2 – b). All four compositions, with and without albumin, showed shear thinning behavior as a decrease in viscosity with increasing shear. A shear thinning behavior is a desirable characteristic for extrusion-based printing to ensure lower viscosity while the feedstock is pressed through the nozzle of the printing head at higher shear rates. Furthermore, all compositions show similar flow behavior which indicates that the addition of albumin concentrations did not significantly influence viscosity and flow behavior of the suspensions which is instead dominated by the interactions between alginate and alumina particles.

Post-printing recovery was estimated by a three-step thixotropy test by successively applying low (0.05 s-1), high (50 s-1) and low (0.05 s-1) shear rates, each for a duration of 60 s (Figure 5.2 – c). All four feedstock compositions, with and without albumin, showed an initial viscosity of approx. 7800 Pa·s at 0.05 s-1 (baseline). By increasing the shear rate to 50 s-1, the viscosity of all four feedstocks dropped to approx. 14 Pa·s. Subsequently, the shear rate was switched back to 0.05 s-1 and the complete recovery of the initial viscosity was observed. All feedstocks showed a high increase in viscosity to 550 Pa·s in

the first two seconds and thereafter the viscosity continuously increased for 20 s until a plateau with the initial viscosity values was reached. Moreover, the shapes of the recovery curve of all four compositions are similar which again indicates that the addition of albumin did not significantly influence feedstock thixotropy.

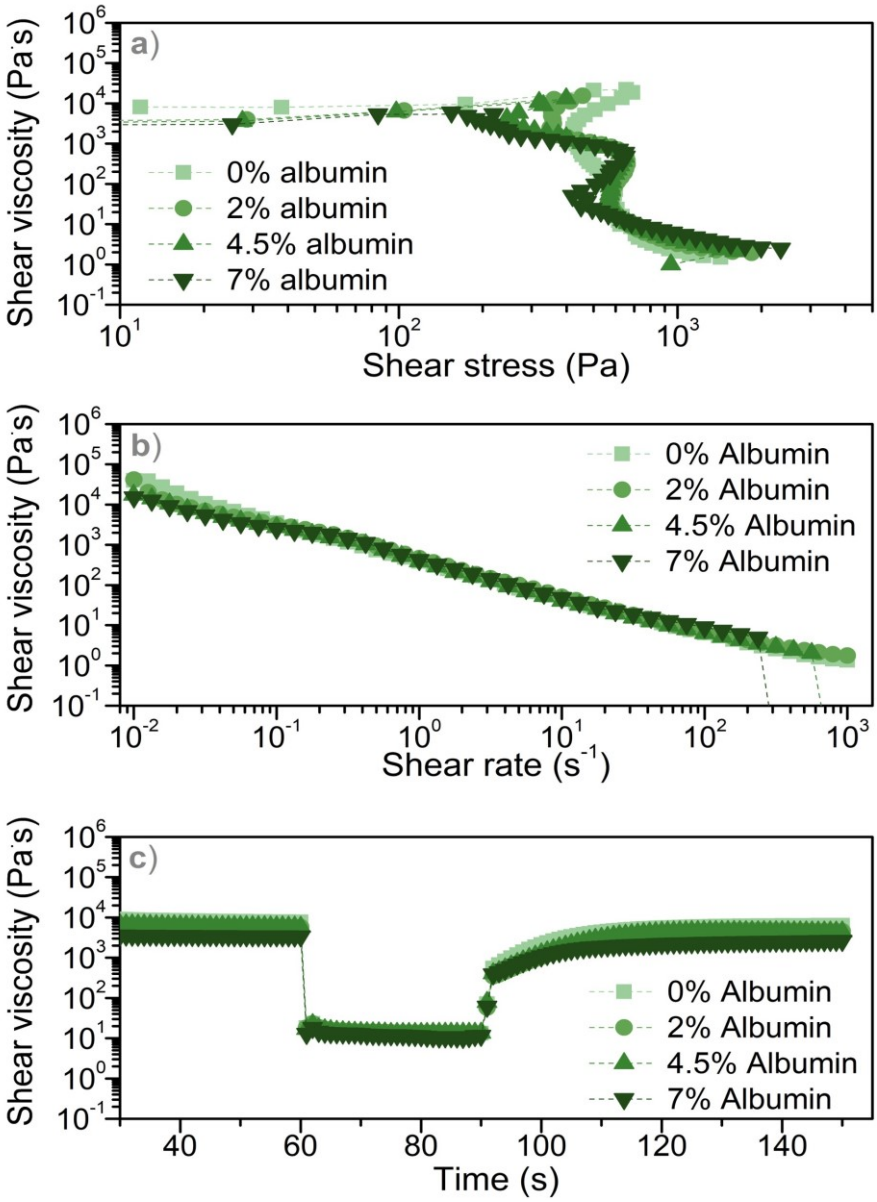

Figure 5.2 – Rotational rheological measurements of a) shear rate ramp, b) shear rate test and c) three-step thixotropy test, and oscillatory rheological measurements. Albumin concentrations are in wt.%.

Oscillatory rheology tests were used to characterize viscoelastic properties of the feedstocks by measuring the elastic (G') and the viscous (G'') modulus. First, oscillatory deformation amplitude (strain) sweeps were performed with all four feedstocks compositions, with and without albumin (Figure 5.3 – a). At low deformation amplitude, all samples showed solid-like behavior with G' higher than G''. This is already evident in the

other gel-like properties discussed above, like high viscosity and a pronounced yield point. The gel-like behavior can be observed for all four compositions up to 10% shear strain. Afterward, G'' is higher than G', which manifests in a fluid-like behavior. Furthermore, frequency sweep tests were performed to observe internal changes in the material (Figure 5.3 – b). All four compositions showed a gel-like behavior with constant moduli during the whole experiment. For both amplitude and frequency sweep tests, the addition of albumin at different concentrations did not significantly influence the rheological behavior of the feedstocks.

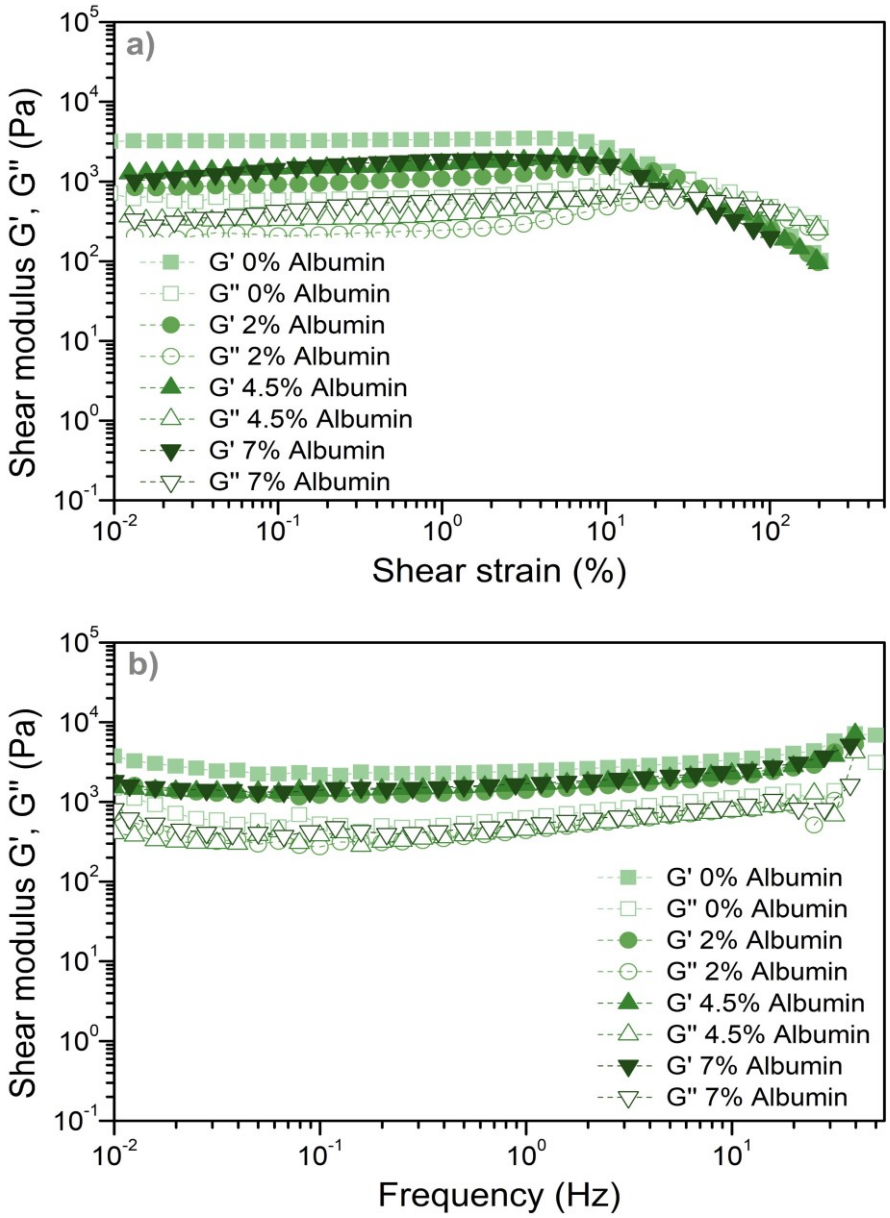

Figure 5.3 – Rotational rheological measurements of a) amplitude sweep and b) frequency of feedstocks with different concentrations of albumin. Albumin concentrations are in wt.%.

5.3.2 Interfacial shear rheology

Interfacial shear rheology experiments were performed to analyze the contributions of alginate, particles, and proteins to the formation of interfacial films that lead to bubble stabilization. Figure 5.4 shows an overview of the two-dimensional storage modulus G' as a function of time for water and feedstocks with albumin concentrations of 2 and 7 wt.% and a control without albumin. G'' is omitted for clarity and is much lower than G' for all samples. Note that the suspensions were diluted ten times with water to ensure that the rheological modules of the bulk phase are significantly lower than those at the interface. First, we analyzed the interfacial shear rheology of the feedstock with alumina particles, but without albumin and the data showed a broad noise spectrum around 10-3 N/m. Accordingly, the device is not sensitive enough to detect potential adsorption of particles at the suspension/air interface. Furthermore, if particles did adsorb at the interface at all, most likely no cohesive thin film was formed [21].

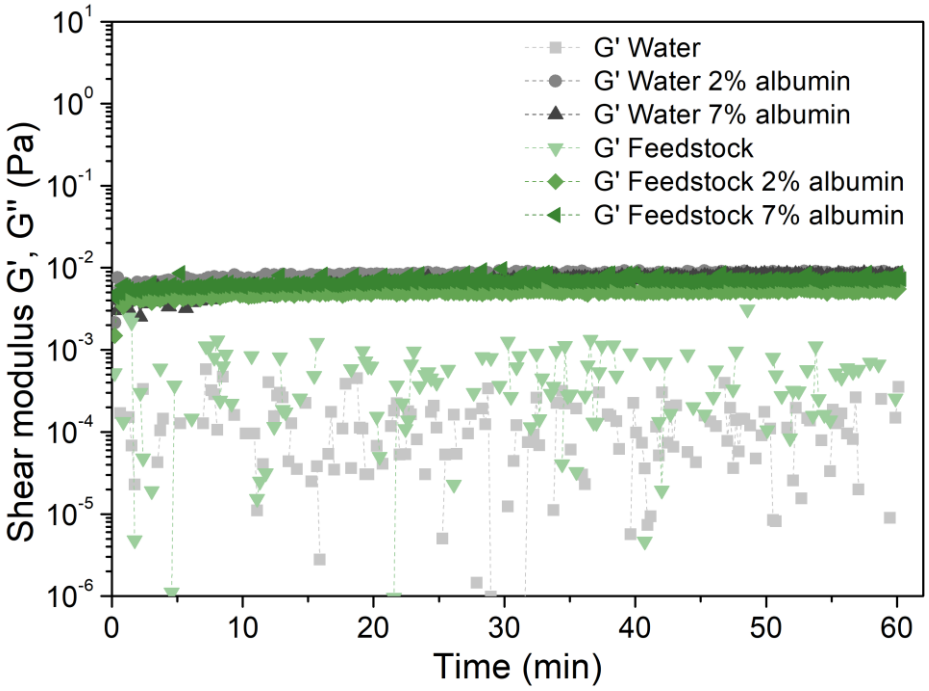

Figure 5.4 – Interfacial rheological measurements of different albumin concentrations dissolved in water and in alginate/alumina suspensions. Albumin concentrations are in wt.%.

When albumin is added into the feedstock, elastic moduli around 10-2 N/m are recorded, indicating that elastic thin films were formed at the interface. Moreover, a constant elastic modulus could be observed already at the beginning of the experiment, indicating fast film formation at the interface. Furthermore, the addition of different concentrations of albumin (2 and 7 wt.%) did not seem to influence the elastic moduli of the film. This indicates that already with 2 wt.% albumin the interface was saturated with albumin resulting in a stable

and cohesive interfacial film. Additionally, albumin dissolved in water showed similar elastic moduli as the suspension containing albumin. This indicates that mostly albumin was responsible for the film formation while alginate or the particles did not significantly influence film formation.

5.3.3 Printability characterization

Next to rheological behavior, several other parameters can influence shape fidelity and integrity of the printed filaments. Here, feedstock printability (Pr) was assessed by measuring the spacing between printed constructs. Ideally, feedstocks (Pr = 1) should demonstrate a clear morphology with a smooth surface and constant diameter of the extruded filament, which results in square holes in the fabricated regular grids. An irregular spacing (Pr > 1) could for example be observed due to irregular filaments with fractured morphology, which might be the result of premature crosslinking or solidification, while a more liquid-like behavior feedstock can result in more circular spacing (Pr < 1) due to filament merging.

To test printability, all four feedstock compositions, with and without albumin, were printed through a Ø 0.93 mm nozzle into a cuboid (final size 2 x 2 x 1 cm) with a 90° grid structure and printability was analyzed after printing 3 and 8 layers (Figure 5.5). The printed filaments exhibited smooth surfaces and with the addition of albumin into the feedstock, small bubbles can be observed on the filament surface. The addition of albumin in either quantities (2 wt. %, 4.5 wt. % or 7 wt. %) maintained good feedstock printability even after printing 8 layers without significantly influencing printability despite the presence of the larger pores inside the strands. On the contrary, samples without albumin showed optimal printability values after printing 3 layers, but after printing 8 layers the structures began to sag and the holes could poorly be measured, indicating that samples without albumin could not resist the weight of following layers and collapsed. Square shapes between the printed channels were observed after printing 3 layers, with Pr values of 0.96 ± 0.02, 1.15 ± 0.05, 1.00 ± 0.05 and 1.03 ± 0.02 for samples with 0 wt.%, 2 wt.%, 4.5 wt.% and 7 wt.% albumin, respectively. After printing 8 layers with 0 wt.%, 2 wt.%, 4.5 wt.% and 7 wt.% albumin, the samples showed Pr values of 0.91 ± 0.03, 1.02 ± 0.04, 1.02 ± 0.02, and 1.02 ± 0.03, respectively. Interestingly, the Pr value of 2 wt.% albumin after printing 3 layers is higher than with 4.5 wt.% and 7 wt.%, but the Pr values of samples containing albumin were all similar after printing 8 layers. Upon visual inspection, the samples at 2 wt.% albumin show some irregularities in filament width, which are not clearly represented in the Pr values that only consider the sphericity of the structure. These irregularities might be related to the relatively low water content at 2 wt.% albumin (see discussion below)

and therefore increased weight of the extruded strands. The first printed layer was set to a lower height than the subsequent layers to assure a better contact between feedstock and substrate and this difference was not taken into account in the Pr value measurement. However, depending on the composition this interaction could be higher or lower. Thus, a higher Pr value of the 2 wt.% albumin samples might indicate a higher interaction of the feedstock with the printing substrate (plastic petri dish), which decreased by increasing the albumin concentration, resulting in a more rectangular form of the spacings for the 2 wt.% albumin feedstocks. Nevertheless, this did not influence further printed layers. Furthermore, the circular forms of the printed filaments could be observed clearly in the vertical cross-sections for samples containing albumin while for samples without albumin no filaments could be identified.

As discussed above, the printability of a feedstock can usually be described by its rheological behavior. Here, based on the rheological characterization, samples with and without albumin should exhibit similar printability but a lower printability of samples without albumin after printing 3 and 8 layers was observed. Consequently, the difference in printability between the samples may be due to different densities whereas filaments without albumin are heavier due to the absence of air bubbles.

Higher concentrations of albumin were not tested since no influence on porosity, printability, or on rheological properties could be observed but higher concentration might decrease material stability due to a lower crosslinking density of the printed filaments.

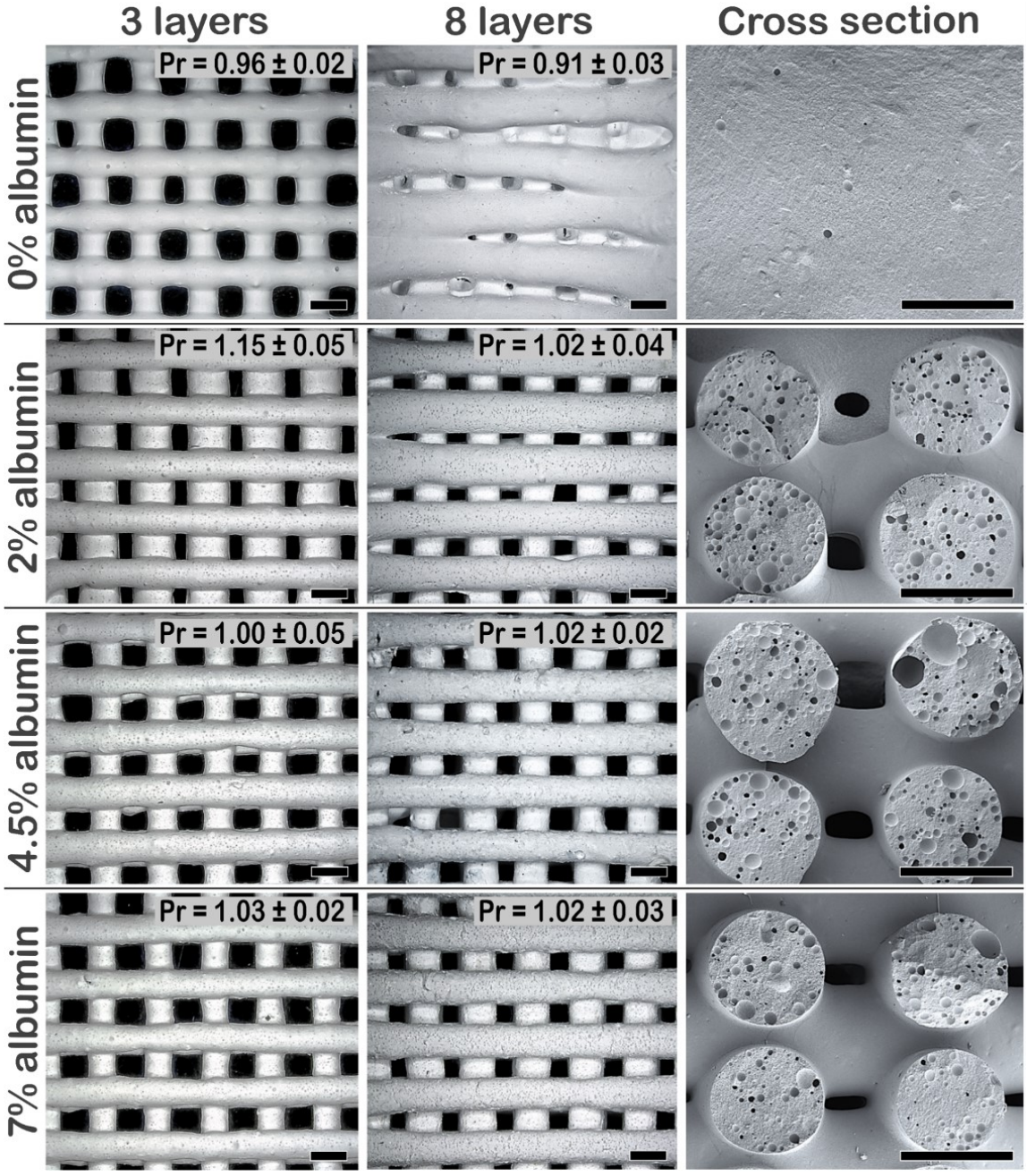

Figure 5.5 – Analysis of feedstock printability with different concentrations of albumin after 3 and 8 printed layers as well cross-section views from 8 printed layers samples. Albumin concentrations are in wt.%. (Scale bar: 1 mm)

5.3.4 Sample porosity

Sample porosity was determined by a combination of two methods: mercury intrusion porosimetry and μCT scans. First, the porosity of samples with 0% albumin was measured by mercury intrusion porosimetry (Figure 5.6) which is able to record pores with diameters

between 0.01 and 10 µm (Figure 5.5). Here, the samples showed 40% open porosity and pore size distribution with pores ranging from 0.01 µm and 0.2 µm.

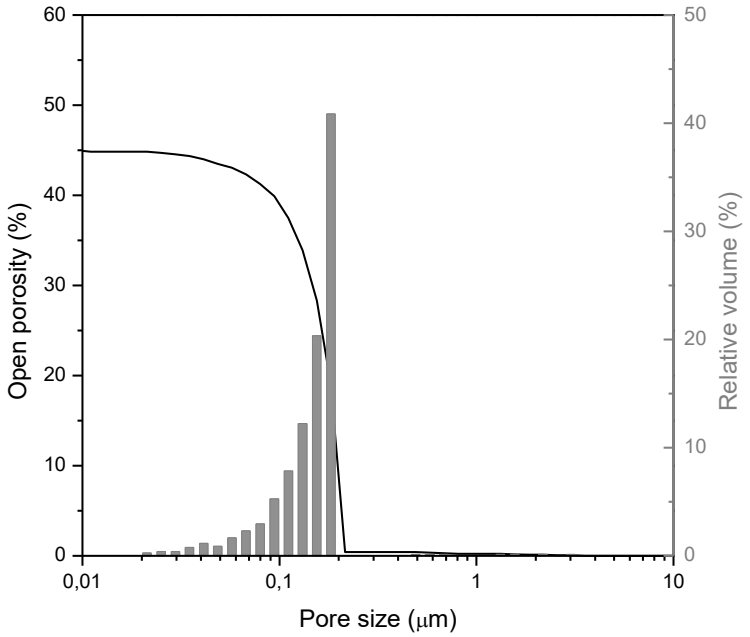

Figure 5.6 - Pore size distribution of 0% albumin samples with pores size between 0.01 and 10 µm, measured by mercury intrusion porosimetry.

Pores bigger than 10 µm were analyzed using µCT (Figure 5.7). For 0% albumin samples, just a few pores bigger than 10 µm could be observed. A higher concentration of pores could be obtained for samples containing albumin with pore radius mainly ranging from 10 µm to 150 µm for gel-cast (GC) and 3D-printed (3D) samples with additional pore sizes ranging from 150 to 500 µm for 3D printed samples stemming from the printed mesh structure. Note that here the pores obtained between the printed constructs were also considered to the pore size distribution. Moreover, a slight influence of the printing process on pore size distribution could be observed for samples containing albumin with a reduction of medium-sized pores (10-150 µm) in comparison with GC samples, which might be related to bubble coalescence during the printing process. Nevertheless, the printed samples still maintained most pores and exhibit high porosity as desired.

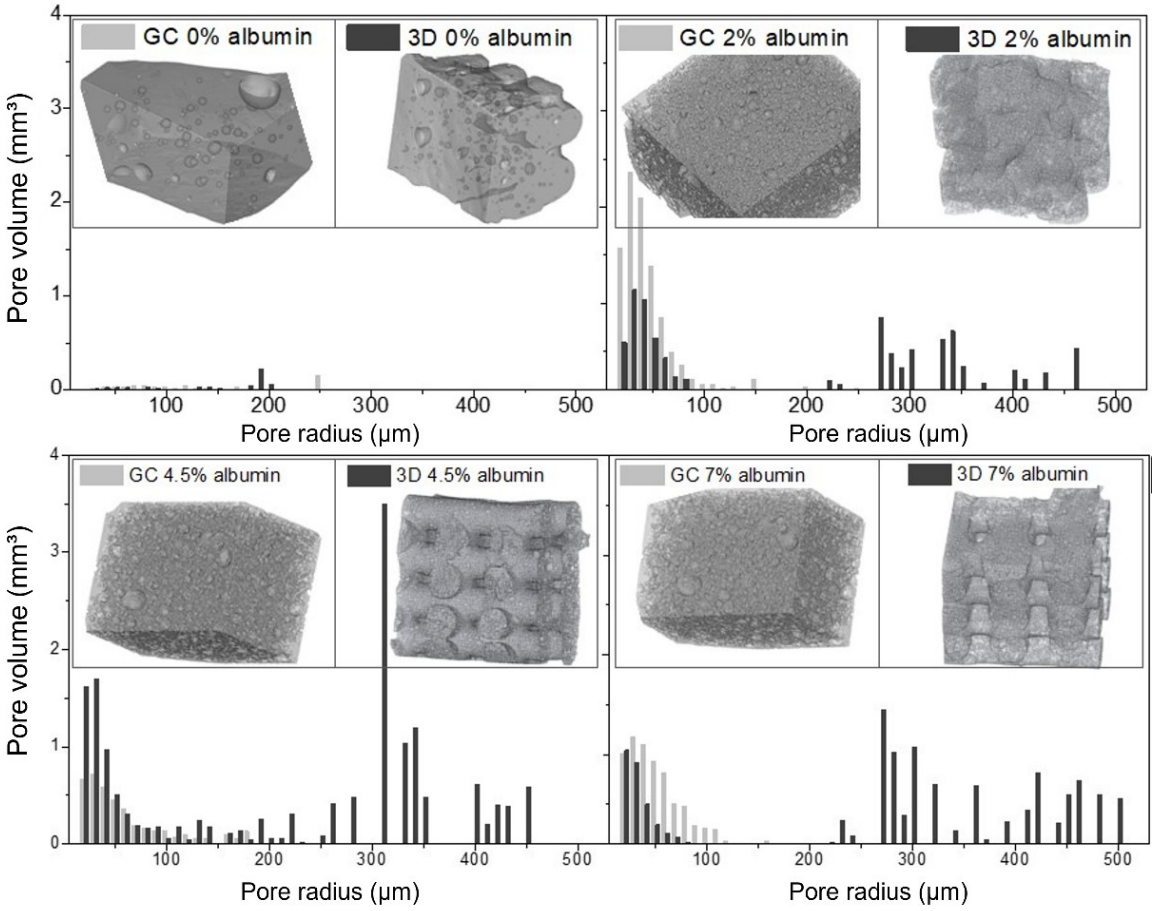

Figure 5.7 – Pore size distribution of pores > 10 μm of gel-cast (GC) and 3D-printed (3D) samples with different albumin concentrations and corresponding 3D images from CT scans of samples with and without albumin (b). Albumin concentrations are in wt.%.

To determine total sample porosity, both measurement techniques were combined to be able to measure pores from 0.01 to 500 μm. For this purpose, μCT scans were used to reconstruct digital representations of the samples from which the total volume was derived. For the regions with pore size smaller than 10 μm, which are shown as dense regions in the filtered μCT scans, porosity was obtained by the mercury intrusion measurements. Thus, the total porosity can be calculated by adding up the porosity of the apparently dense region in μCT and the porosity as determined by mercury intrusion porosimetry to the total material porosity (Table 5.1). The addition of 2 wt.% albumin to the gel-cast samples increased the porosity > 10 μm by approx. 18%, in comparison with gel-cast samples without albumin, whereas the addition of 2 wt.% albumin followed by 3D printing increased the porosity > 10 μm by approx. 32%. Further comparing 2 wt.% albumin samples with gel-cast samples without albumin, sample total porosity increased approx. 10% and 20% for gel-cast and 3D printed. Moreover, higher concentrations of albumin did not significantly influence the total porosity further. The difference in porosity confirms the

explanation for the difference in printability between samples containing albumin and without it, showing samples without albumin have lower porosity and therefore a higher density than samples containing albumin.

Table 5.1 - Samples total porosity depending on the shaping method of gel casting (GC) or 3D printing (3D) and with different albumin concentrations. Albumin concentrations are in wt.%.

	Porosity < 10 µm (%)	Porosity > 10 µm (%)	Total Porosity (%)
GC 0% Albumin	45.33 ± 0.05	0.59 ± 0.12	45.92 ± 0.06
GC 2% Albumin	37.09 ± 0.27	18.66 ± 0.58	55.76 ± 0.32
GC 4.5% Albumin	38.77 ± 0.09	14.98 ± 0.20	53.75 ± 0.11
GC 7% Albumin	36.97 ± 0.41	18.93 ± 0.89	55.90 ± 0.49
3D 0% Albumin	45.60 ± 0.05	6.76 ± 3.27	52.36 ± 5.79
3D 2% Albumin	27.90 ± 1.79	38.83 ± 3.93	66.72 ± 2.14
3D 4.5% Albumin	27.07 ± 2.14	40.65 ± 4.70	67.71 ± 2.56
3D 7% Albumin	31.20 ± 1.64	31.58 ± 3.60	62.78 ± 1.96

5.3.5 NMR diffusion characterization

The volume-averaged effective diffusion coefficient of water in the samples produced by gel casting (GC) and 3D printing (3D) with different concentrations of albumin was measured using NMR tomography. In this context, the effective diffusion coefficients provide a relative measure of water concentration in the sample and therefore help to assess changes in porosity in the wet hydrogel nanocomposite samples with different compositions. First, the diffusion coefficient of the liquid in the structure was determined by choosing three arbitrary regions of interest (ROIs). The averaged diffusion coefficients D were reported for the measured ROIs based on an exponential relation between signal amplitude and diffusion weighting $S = S0 \cdot \exp(-bD)$ with the signal amplitudes S and S0 measured with and without diffusion sensitizing gradients and the strength of diffusion weighting b. The data is given in Table 3. Additionally, Figure 5.8 shows GC and 3D printed samples containing different albumin concentrations with the obtained signal intensity versus the applied diffusion weighting (DW). For GC samples, the diffusion coefficient increased from 0.9304 to 1.0707, 1.2368, and 1.2365 $103 \cdot mm^2.s\text{-}1$ while for 3D printed samples, the diffusion coefficient increased from 0.63 to 1.03, 1.27, and 1.63 $10^3 \cdot mm^2.s\text{-}1$ for samples with 0%, 2%, 4.5% and 7% albumin, respectively.

Contrary to the CT and mercury intrusion results, an increase in water content and therefore porosity was observed in samples with higher albumin concentration. This might

be explained by the different sample preparation since CT and mercury intrusion measurements were performed with dry samples and NMR experiments with wet samples. Accordingly, slight swelling of the structure might have led to increased water uptake and an increase in porosity. Notably, albumin itself is capable of absorbing water and forming gels [22-24] and consequently, a higher concentration of albumin might increase the water content of the sample. Furthermore, the printing process did not seem to have a significant influence on the diffusion coefficient compared to the gel-cast samples (Table 5.2).

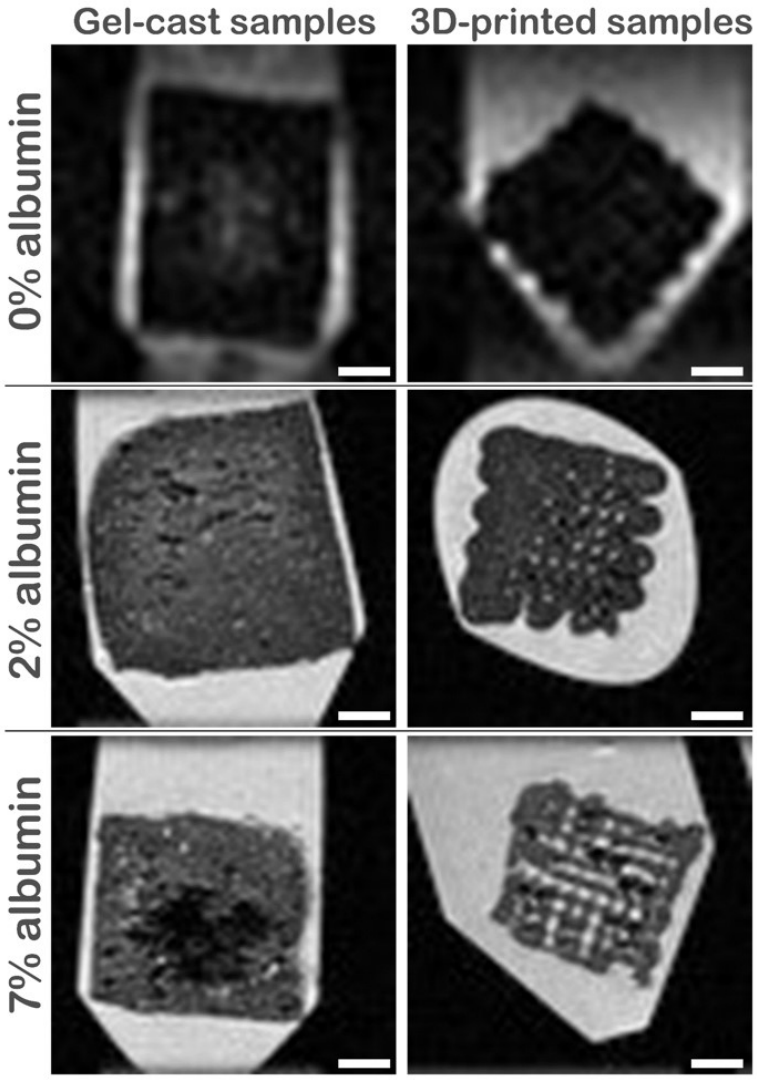

Figure 5.8 – Diffusion-weighted (DW) MRI imaging from water diffusion in gel-cast and 3D-printed samples with different albumin concentrations. Albumin concentrations are in wt.% (scale bar: 5 mm).

Table 5.2 - Diffusion coefficient depending on the shaping method of gel casting (GC) and 3D printed structures (3D) for different albumin concentrations. Albumin concentrations are in wt.%.

	Diffusion coefficient ($10^3 \cdot mm^2 \cdot s^{-1}$)
GC 0% Albumin	0.93 ± 0.10
GC 2% Albumin	1.07 ± 0.09
GC 4.5% Albumin	1.24 ± 0.10
GC 7% Albumin	1.24 ± 0.10
3D 0% Albumin	0.63 ± 0.18
3D 2% Albumin	1.03 ± 0.07
3D 4.5% Albumin	1.27 ± 0.05
3D 7% Albumin	1.63 ± 0.05

5.3.6 Bacterial viability

Compatibility of the nanocomposite gels with bacterial cells was exemplarily characterized for *E. coli*. To determine the influence of the feedstock's chemical composition and printing process on the embedded bacteria, the effective viability of the immobilized bacteria in gel-cast and 3D-printed samples with all four compositions after calcium crosslinking was analyzed by cellular reduction of resazurin (blue color) into resorufin (pink and fluorescent color). The effective bacteria viability was then quantified by the resazurin assay after 4, 24, and 48 hours of incubation in PBS (Figure 5.9 - a) and compared with the viability of the same quantity of freely suspended cells (Figure 5.9 - b). It is important to note that the obtained effective bacterial viability relates to the viability of the fraction of cells embedded inside the samples that are accessible by resazurin molecules and the corresponding metabolites.

For gel-cast samples (GC), approx. 20% effective bacterial viability was measured with 0% and 2% albumin samples after 4 hours of incubation. By increasing albumin concentrations to 4% and 7%, the effective bacterial viability also increased to 40% and 50%, respectively. This increase in effective bacterial viability is an interesting behavior since pore size and porosity minimally changed between the different albumin concentrations. Thus, to understand the effects of alginate and albumin on the viability of the accessible bacteria, analogous viability tests were performed after 4, 24, and 48 hours of incubation with freely suspended cells and different concentrations of alginate (1 wt.%, 0.5 wt.% and 0.25 wt.%), different concentrations of albumin (7 wt.%, 3.5 wt.%, and 1.75 wt.%) and with different concentrations of alginate and albumin mixtures (0.5 and 3.5 wt.%, and 0.25 and 1.75 wt.%, respectively) – Figure 5.9 - b. Alginate does not seem to influence

viability of the suspended bacteria, since cells incubated with all alginate concentrations showed similar viability values as cells incubated in PBS. Conversely, an increase in bacterial viability could be observed incubating cells in albumin solutions, indicating that bacteria could use albumin proteins as nutrition, inducing bacterial growth. Furthermore, similar viability values could be observed for 7 wt.%, 3.5 wt.%, and 1.75 wt.% albumin, as well as mixtures of alginate and albumin. Moreover, solutions containing 1.75% albumin and a mixture of 0.25% alginate and 1.75% albumin showed a decrease in cell viability after 24 and 48 hours while no changes in bacterial viability were observed for the other samples containing 3.5% and 7% albumin. This may indicate that 1.75% albumin induced cell proliferation in the first hours, but the protein concentration was not sufficient to maintain cell viability after 24 and 48 hours. Therefore, the slight increase in effective bacterial viability with increasing albumin concentration of gel-cast samples most likely indicates bacterial proliferation inside the structure.

Immobilized cells in 3D-printed samples (3D) with 0% albumin showed similar effective viability results (20%) as GC 0% albumin, indicating that the printing process has a minimal influence on the effective bacterial viability. Increasing albumin concentration results in an increase of effective viability of approx. 50%, 80%, and 120% after 4h incubation for 2%, 4.5%, and 7% albumin samples, respectively. Thus, the effective bacterial viability of 3D-printed samples is significantly higher than for GC samples. This difference in bacterial viability is related to the higher accessibility of the embedded bacteria for the porous samples containing albumin while no significant differences between GC and 3D at 0% albumin could be observed since the printed structure with 0% albumin collapsed to a similar shape as the GC sample. Furthermore, the effective viability over time shows a decrease in cell viability mainly for 4.5% and 7% albumin samples, which diverges from the freely suspended bacterial test (Figure 5.8 - b). This may be related to the accessibility of the immobilized cells which may decrease over time due to cell growth and therefore cause a lower effective bacterial viability.

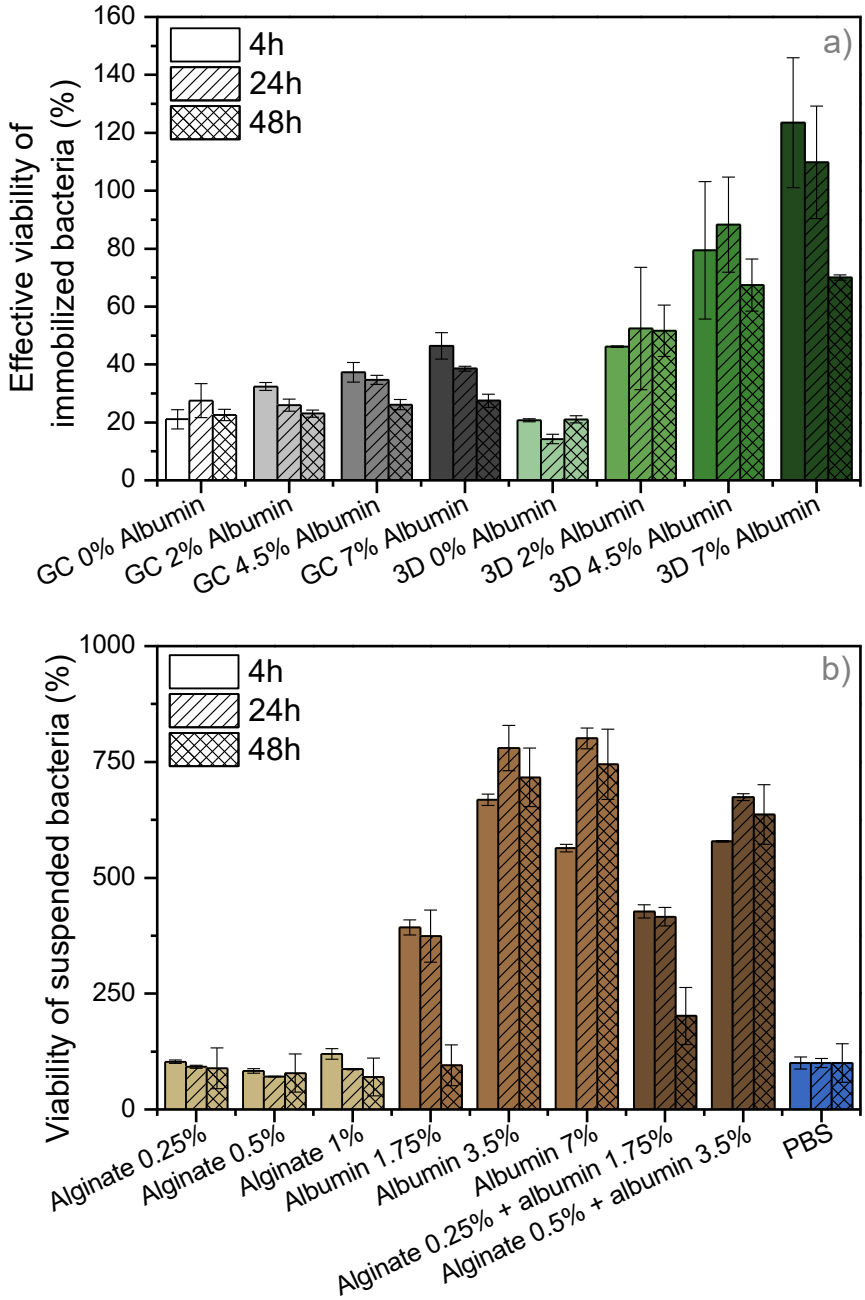

Figure 5.9 –Immobilized bacterial viability in gel-cast and 3D-printed samples with different albumin concentrations (a) and influence of different alginate, albumin, and alginate + albumin concentrations on bacterial viability of freely suspended cells (b). Albumin concentrations are in wt.%.

5.4 Conclusions

In summary, a new feedstock suitable for 3D printing nanocomposite materials with hierarchical porosity and embedded bacteria was developed. The feedstock is composed of a highly filled alginate/alumina nanocomposite to assure mechanical stability whereas

the addition of ovalbumin as a foaming agent added large pores in the range of 10 µm to 150 µm into the nanocomposite. The formation of interfacial films at the pore interface was analyzed by interfacial shear rheology to assess bubble stability. The results show that mostly albumin was responsible for film formation while alginate or the particles did not significantly stabilize the foam. Furthermore, rheological characterization of the bulk showed suitable characteristics for 3D printing like shear thinning, high yield stress, fast thixotropic recovery time and a gel-like behavior while albumin did not significantly influence bulk rheological properties. Nevertheless, the addition of albumin improved printability, which might be related to the difference in filament densities whereas filaments without albumin are heavier due to the absence of air bubbles. To quantify the sample's porosity and pore size from 0.01 µm to 1 mm, a combination of mercury intrusion porosimetry and µ-CT was implemented. The addition of albumin increased the porosity by approx. 10% and 20% for gel-cast and 3D-printed samples, respectively, while different albumin concentrations did not significantly influence the porosity further in dry samples. Additionally, with NMR tomography an increase in the water content with increasing albumin concentrations was observed, which might be related to the capacity of albumin to form hydrogels. Furthermore, the influence of albumin addition could also be observed by analyzing the viability of *E. coli* bacteria, whereas a higher albumin concentration also resulted in higher effective cell viability. Furthermore, an increase in bacteria viability was observed with increasing albumin concentration in bacterial suspensions, indicating that bacteria could use albumin as nutrition. Consequently, the presence of albumin might enhance bacterial proliferation as well as the accessibility of the bacteria inside the structure due to enhanced porosity. The open mesh structure of the printed parts further improved the accessibility of nutrients to the bacteria inside the structure. This demonstrates the potential of 3D-printed hierarchical structures for novel applications in bioprocessing and related applications.

5.5 References

1. Condi Mainardi, J., Bonini Demarchi, C., Mirdrikvand, M. et al. *3D bioprinting of hydrogel/ceramic composites with hierarchical porosity*. J Mater Sci (2022).

2. Correia Carreira, S., R. Begum, and A.W. Perriman, *3D Bioprinting: The Emergence of Programmable Biodesign*. Advanced Healthcare Materials, 2020. 9(15): p. 1900554.

3. Skardal, A. and A. Atala, *Biomaterials for integration with 3D bioprinting*. Ann. Biomed. Eng., 2015. 43: p. 730.

4. Tasoglu, S. and U. Demirci, *Bioprinting for stem cell research*. Trends Biotechnol., 2013. 31: p. 10.

5. Dababneh, A.B. and I.T. Ozbolat, *Bioprinting technology: a current state-of-the-art review*. ASME J. Manuf. Sci. Eng., 2014. 136(6): 061016.

6. Willaert, R., *Cell immobilization and its applications in biotechnology: Current trends and future prospects*. 2007. p. 289-362.

7. Nemati, M. and C. Webb, 2.24 - *Immobilized Cell Bioreactors*, in Comprehensive Biotechnology (Second Edition), M. Moo-Young, Editor. 2011, Academic Press: Burlington. p. 331-346.

8. Zhu, Y., *Chapter 14 - Immobilized Cell Fermentation for Production of Chemicals and Fuels*, in Bioprocessing for Value-Added Products from Renewable Resources, S.-T. Yang, Editor. 2007, Elsevier: Amsterdam. p. 373-396.

9. Armstrong, J.P.K., et al., *3D Bioprinting Using a Templated Porous Bioink*. Advanced Healthcare Materials, 2016. 5(14): p. 1724-1730.

10. Kessel, B., et al., *3D Bioprinting of Architected Hydrogels from Entangled Microstrands*. bioRxiv, 2019: p. 2019.12.13.870220.

11. Ruiz-Cantu, L., et al., *Multi-material 3D bioprinting of porous constructs for cartilage regeneration*. Materials Science and Engineering: C, 2020. 109: p. 110578.

12. Condi Mainardi, J., Rezwan, K. & Maas, M. *Embedding live bacteria in porous hydrogel/ceramic nanocomposites for bioprocessing applications*. Bioprocess Biosyst Eng 42, 1215–1224 (2019).

13. Bao, G., et al., *Triggered micropore-forming bioprinting of porous viscoelastic hydrogels*. Materials Horizons, 2020. 7(9): p. 2336-2347.

14. Shao, L., et al., *Sacrificial microgel-laden bioink-enabled 3D bioprinting of mesoscale pore networks*. Bio-Design and Manufacturing, 2020. 3(1): p. 30-39.

15. Ying, G.-L., et al., *Aqueous Two-Phase Emulsion Bioink-Enabled 3D Bioprinting of Porous Hydrogels*. Advanced Materials, 2018. 30(50): p. 1805460.

15. Minas, C., et al., *3D Printing of Emulsions and Foams into Hierarchical Porous Ceramics*. Advanced Materials, 2016. 28(45): p. 9993-9999.

17. Tariq, F., et al., *Characterization of hierarchical pore structures in ceramics using multiscale tomography*. Acta Materialia, 2011. 59(5): p. 2109-2120.

18. Nakanishi, K., *Porosity Measurement*, in Handbook of Sol-Gel Science and Technology, L. Klein, M. Aparicio, and A. Jitianu, Editors. 2016, Springer International Publishing: Cham. p. 1-11.

19. Robinson, N. and C. D'Agostino, *NMR Investigation into the Influence of Surface Interactions on Liquid Diffusion in a Mesoporous Catalyst Support*. Topics in Catalysis, 2020. 63(3): p. 319-327.

20. Di Tullio, V., D. Capitani, and N. Proietti, *Unilateral NMR to study water diffusion and absorption in stone-hydrogel systems*. Microporous and Mesoporous Materials, 2018. 269: p. 180-185.
21. Maas, M., et al., *Towards the synthesis of hydroxyapatite/protein scaffolds with controlled porosities: Bulk and interfacial shear rheology of a hydroxyapatite suspension with protein additives*. Journal of Colloid and Interface Science, 2013. 407: p. 529-535.
22. Nojima, T. and T. Iyoda, *Egg white-based strong hydrogel via ordered protein condensation*. NPG Asia Materials, 2018. 10(1): p. e460-e460.
23. Rathna, G., J. Li, and S. Gunasekaran, *Functionally-modified egg white albumen hydrogels*. Polymer International, 2004. 53(12): p. 1994-2000.
24. Godiya, C.B., S. Kumar, and Y. Xiao, *Amine functionalized egg albumin hydrogel with enhanced adsorption potential for diclofenac sodium in water*. Journal of Hazardous Materials, 2020. 393: p. 122417.

6 Genipin-crosslinked chitosan/alginate/alumina nanocomposite gels for 3D bioprinting

6.1 Introduction

Chapter 6 has been adapted from Bioprocess and Biosystems Engineering, 2022 - 45: p. 171-185. (DOI: 10.1007/s00449-021-02650-3) with permission from Springer Nature [1].

Developing a bioink to 3D bioprinting of innovative bioreactor concepts necessitates support material and the embedded cells which are able to withstand the rigors of long-term continuous flow processing of the bioreactor or in related conditions. Likewise, the fabrication of complex porous geometries for bioreactors with highly accessible surface areas necessitates innovative printing strategies that result in rigid and insoluble materials. While bioprinting of cells embedded in soft hydrogels has been well established especially in the field of regenerative medicine [2], printing of biomaterials that incorporate living cells is still very challenging, especially considering the production of mechanically rigid and insoluble substrates usually requires non-biocompatible processes such as chemical crosslinking or sintering [3].

In the previous chapters, the immobilization of bacteria *E. coli* or *B. subtilis* into rigid alginate/alumina nanocomposites by gel casting with good mechanical properties and high cell viability after 60 days of storage and the 3D-bioprinting of hierarchical structures by the addition of the protein albumin was analyzed. Alginate is a gelling polysaccharide with high biocompatibility that undergoes a biocompatible gelation process with Ca^{2+} ions. Forming a highly-filled nanocomposite of alginate with alumina results in enhanced mechanical properties of the gel, particularly greatly reduced shrinking during drying and net-near-shape processing during extrusion and molding. However, due to the lack of covalent crosslinking in this hydrogel/ceramic nanocomposite, the material degrades over time and is therefore unsuited for long-term application. To further enhance this nanocomposite hydrogel, oppositely charged polymers (e.g. chitosan) can be used to crosslink alginate by forming polyelectrolyte complexes [4-7]. This strategy is widely used for cell encapsulation, usually by first encapsulating cells in alginate microspheres via ionotropic gelation, followed by a coating with chitosan via the principle of polyelectrolyte complexation [8-10]. By coating alginate with chitosan, a slower degradation rate could be demonstrated while high bacteria viability was achieved by protecting bacteria within the alginate from the antibacterial properties of chitosan [11]. Colosi et al. used the same principle for 3D printing by first printing alginate suspensions (without cells) followed by a coating step with chitosan [12], and the coating was further reinforced by covalent

crosslinking to ensure the structural stability of the materials in culture media for a prolonged period of time.

To date, 3D bioprinting of chitosan corresponds to just approx. 4% of bioprinting publications but has shown promising results in the field of tissue engineering. In the field of bioprocessing, the use of chitosan in conjunction with 3D printing is still nascent [13, 14]. However, chitosan gels have low mechanical resistance, which is one of the main limitations of their use in 3D bioprinting. To overcome this drawback, chitosan is often used in combination with other components to enhance its mechanical properties [15]. An innovative alternative for covalently crosslinking chitosan is to use genipin as a crosslinking agent, which is a small molecule with very low toxicity and it is able to crosslink proteins and polysaccharides containing amine groups [16-18]. However, the genipin–chitosan crosslinking reaction takes several hours [19, 20] and is therefore not fast enough to immediately reinforce 3D-printed structures that otherwise would not maintain their shape after printing [21]. Therefore, a combination of reinforcement strategies might be required to improve printability, shape fidelity, and long-term stability [22, 23-25].

In this chapter, a biocompatible feedstock for 3D bioprinting which utilizes the crosslinking reaction between chitosan and genipin was developed. To achieve printability and structural fidelity, the feedstock is based on a highly filled alumina/chitosan nanocomposite gel which is combined with different admixtures of alginate to tailor the rheological properties of this gel and to enhance its biocompatibility. The slow crosslinking reaction between genipin and chitosan enables the addition of genipin before printing without blocking the printing nozzle. Furthermore, the covalent crosslinking reaction should prevent long-term dissolution of the samples. The rheological properties of the feedstock were analyzed in depth providing information on network structure and printability. Detailed feedstock printability characterization and assessment of long-term stability were carried out via image analysis of printed constructs. Living *Escherichia coli* were integrated into the feedstock to test the biocompatibility of the nanocomposite with bacteria and to demonstrate potential applications in bioprocessing. Therefore, bacterial viability was analyzed as a function of the different material components as well as of the printing process.

6.2 Fabrication of bionanocomposites

All dispersions and solutions were prepared in sterile conditions. First, 1.3 g chitosan was dissolved in 50 mL of 0.1 % acetic acid solution at room temperature (RT) via a dispermat (IKA RW20.n - Staufen, Germany) for 30 min at 600 rpm. After total dissolution of chitosan,

alumina powder was slowly added into the solution and was further stirred at 1200 rpm for 30 min for homogenization. Thereafter, the pH was adjusted to 6 with 1M NaOH solution. In parallel, 1.3 g alginate (alginic acid sodium salt from brown algae medium viscosity from Sigma Aldrich Chemie GmbH with product number: A2033) was dissolved in 50 mL millipore water at room temperature (RT) using a dispermat (IKA RW20.n - Staufen, Germany) for 30 min at 600 rpm and thereafter NaCl was added to a final concentration of 0.7 wt. % and mixed until dissolution. Then, 20 mL of the 2.5 wt.% alginate solution was added into the chitosan/alumina suspension to a total polymer concentration of 2.5 % which contains 30 wt.% of alginate and stirred for homogenization at 1000 rpm for 20 min. For all suspensions, the ceramic and overall polymer content was maintained constant at 42 vol.% and 2.5 wt.%, respectively. A solution without alginate was also produced for comparison purposes (see Table 6.1). After that, the suspension could be further processed or stored at 4°C.

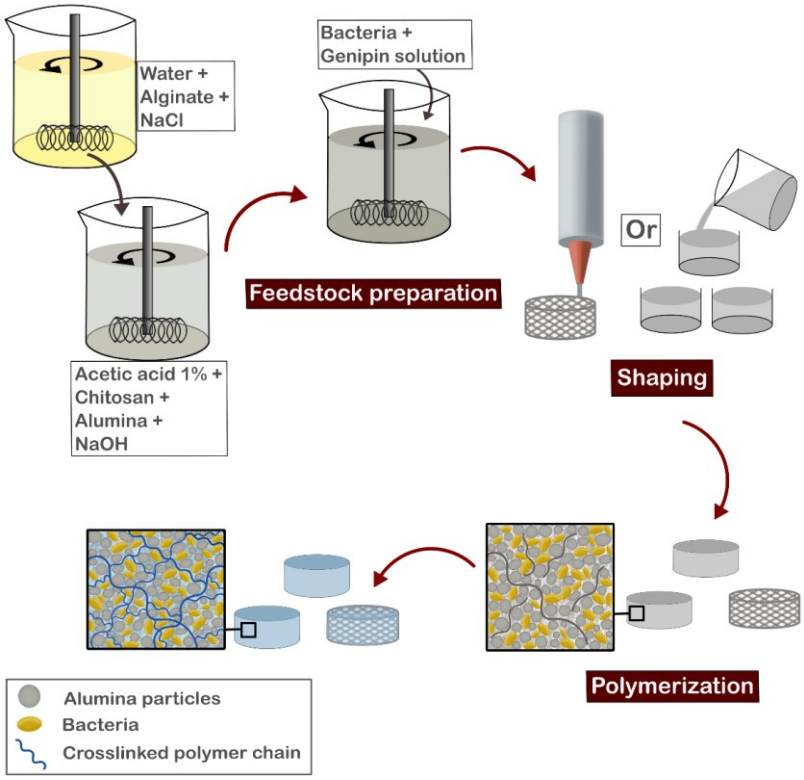

Figure 6.1 - Scheme illustrating the bionanocomposite processing route. First, chitosan is dissolved in water followed by the addition of alumina powder. After homogenization of the mixture, alginate solution and thereafter microorganisms can be incorporated into the suspension. Lastly, genipin is added as a crosslinking agent. The feedstock can be shaped by either gel casting or 3D printing.

After removal from storage at 4°C, the suspensions were stirred for five minutes at 1200 rpm in sterile conditions to increase the temperature of the suspension to 25°C, followed by the addition of 2 mL of LB medium (Figure 6.1). After homogenization, the stirring velocity was decreased to 400 rpm and the bacteria suspension in PBS was added to the mixture, followed by intense stirring at 1000 rpm for 30 s. A 4 wt.% genipin stock solution was prepared by dissolving genipin (genipin from Challenge Bioproducts with product number: 6902-77-8) in absolute ethanol which was ultrasonicated for 5 min. Then, Millipore water was added to decrease the ethanol concentration to 20 vol.% and obtain the final genipin concentration of 4 wt.%. Then, the genipin solution was added to the feedstock to a final concentration of 0.44 wt.% relative to chitosan weight, resulting in a solution with a final concentration of 0.26 or 0.20 mM of genipin, for 0% and 30% alginate formulations, respectively. A summary of all concentrations used for material production can be observed in Table 6.1. It is important to note that the overall polymer concentration (chitosan + alginate) as well as the overall concentration of ceramic particles were maintained constant for comparison purposes. Furthermore, the concentration of genipin was maintained constant regarding the chitosan concentration, since genipin crosslinking just occurs with chitosan.

Table 6.1 - Final concentrations of the feedstock composition.

Sample	Chitosan (mg/mL)	Alumina (g/mL)	Alginate (mg/mL)	Genipin (mM)
0%	13.5	1.23	0	0.26
30%	9.45	1.23	4.05	0.20

After genipin addition, the feedstock was mixed at 1200 rpm for 30 s. Subsequently, the feedstock was shaped by two different processing routes: gel casting or 3D printing. For the gel-cast samples, the bioink was cast into small petri dishes (Ø 35 mm) at room temperature, which were partially covered with Parafilm to avoid significant drying. 3D printed samples were printed into lattice cubes (2 x 2 x 1 cm) using the printer Inkredible (Cellink, Gothenburg, Sweden) in a 6-well plate with a conical precision tip nozzle (Ø 940 µm) with an extrusion air pressure of 20 ± 5 kPa, a printing speed of 10 mm/s and a printing temperature of 30°C – similar as other publications using chitosan-based bioink [25, 26]. The numerical controlled programming language G-code with the printing commands was generated using the Cellink HeartWare 2.4.1 software, from Cellink, with a 67% infill density and 0.85 mm layer high. Afterward, each well was filled with PBS to avoid drying. Additionally, some wells were filled with a 6.6% LB solution. Then, the shaped samples

(gel-cast and 3D-printed samples) were stored in an incubator at 37°C for 24 h without shaking for crosslinking. Thereafter, gel-cast and 3D-printed samples were removed from the incubator and washed with PBS to remove any freely suspended bacteria in the supernatant before further characterization.

6.3 Results and discussion

6.3.1 Chitosan crosslinking

Bioinks must accomplish several requirements for processing with a 3D bioprinter. The main challenge here is to develop a feedstock that meets both printability and biocompatibility requirements and fulfills the criteria dictated by their application. In the case of bioprocessing, the main criteria would be a material that does not dissolve or lose its mechanical properties during extended periods of time in the processing environment. Here, a chitosan/alginate/alumina nanocomposite gel for bacteria immobilization was developed and demonstrated its suitability for 3D printing. The stability of this gel is reinforced by two different crosslinking methods: during bioink preparation, alginate electrostatically interacts with chitosan, and after shaping the gel is interconnected by covalent crosslinking of the chitosan chains with genipin. To this end, first, a viscous chitosan gel is prepared in which a high concentration of alumina nanoparticles is suspended. This highly filled nanocomposite gel is then further mixed with alginate leading to electrostatic crosslinking between the amine groups of the chitosan backbone and the carboxylic groups of the alginate molecules (Figure 6.2 - 1). Since electrostatic crosslinking cannot ensure stability of the gels in different media with varying salinity and pH, a second crosslinking method by the addition of genipin into the feedstock was used. Note that genipin is added to the feedstock directly before printing, but it only becomes effective several hours after printing due to the slow gelation time of this reaction. Genipin crosslinks the amine groups of the chitosan backbone by a covalent reaction in addition to the electrostatic interactions between alginate and chitosan (Figure 6.2 – 2).

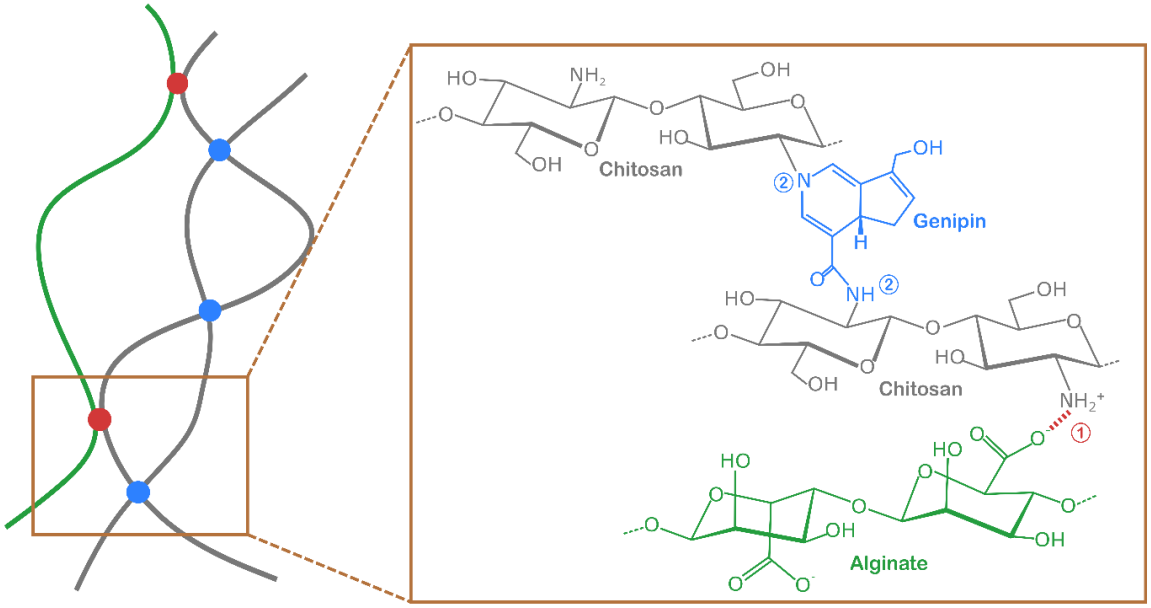

Figure 6.2 - Illustration of the dual-crosslink of chitosan: (1) electrostatic interaction between the carboxylic acid groups of alginate and amine groups of chitosan; (2) covalent bond formed between the amine groups of chitosan and genipin.

6.3.2 Rheological characterization

The rheological properties are crucial for controlling printability and shape fidelity of the bioink and the printed constructs. Therefore, the rheological properties of the feedstock were characterized by a variety of tests that provide information about its behavior before, during and after the printing process. Specifically, a shear rate ramp was performed to observe the material's yield stress for flow initiation, a shear rate test to observe the flow behavior, and a three-step thixotropy test to observe the recovery of the feedstock gel after printing. In these tests, the effect of the addition of alginate was compared to the chitosan/alumina mixture. Chitosan and alumina on their own show low viscosities with slight shear thinning and insignificant yield points which are unsuited for printing (data not shown). A shear rate ramp test was performed to analyze the stress necessary to initiate material flow (Figure 6.3 - a). Both feedstocks showed similar curves and a yield point at approx. 120 Pa. This high yield point assures that the material only starts to flow after a suitable stress is applied. The results of the shear rate tests are shown in Figure 6.3 - b. Both gels show shear thinning behavior as a decrease in viscosity with increasing shear rate is observed. A shear thinning behavior is a desirable characteristic for printing since it assures lower viscosity at high shear rate, which facilitates the extrusion process through the nozzle of the printing head. Furthermore, the samples with and without alginate both show similar flow behavior. In comparison, Hafezi et al. [21] printed chitosan-PEG-genipin

and obtained similar viscosity results after the initiation of genipin crosslinking, which resulted in a more precise shape of the printed constructs and better mechanical properties.

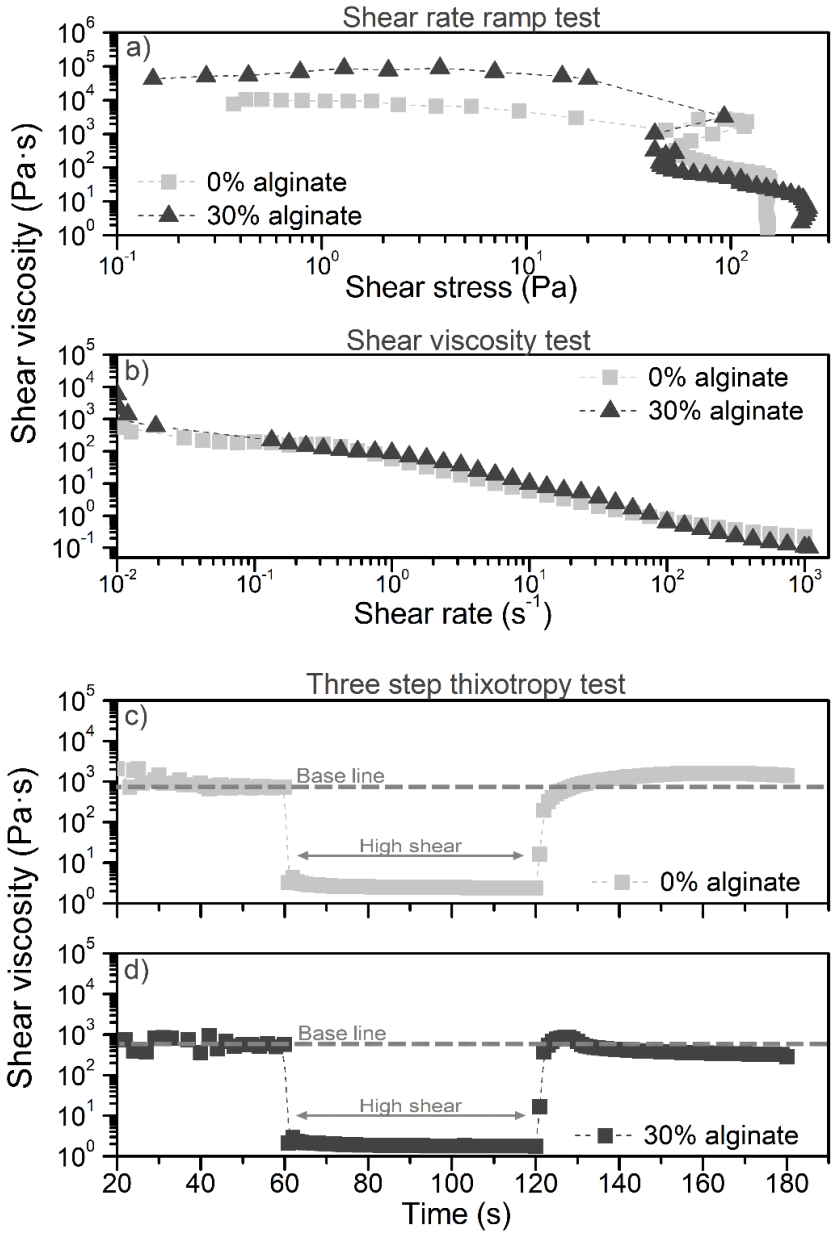

Figure 6.3 - Graph a) shows the results of a shear rate ramp test plotted to determine the yield point, b) a stepped shear rate test, and c) and d) a three-step thixotropy test of chitosan/alumina feedstock without (0%) and with alginate (30%).

Post-printing recovery was approximated by a three-step thixotropy test by applying low (0.05 s-1), high (50 s-1), and low (0.05 s-1) shear rates, each for a duration of 60 s (Figure 6.3 - c and d). Both feedstocks, with and without alginate, showed an initial viscosity of approx. 600 Pa·s at 0.05 s-1 (baseline). Thereafter, the shear rate is increased to 50 s-1 and the viscosity of both gels dropped to approx. 2 Pa·s. Subsequently, a shear rate of

0.05 s-1 is applied again and we observed the complete recovery of the initial viscosity. Feedstock without alginate took about 9 s for the viscosity to return to the initial value (baseline) while feedstocks with alginate recovered much faster after about 2 s. Additionally, the shape of the recovery curve of both feedstocks differs: without alginate, a progressive increase in viscosity is observed until it reaches a plateau slightly higher than the baseline, while the alginate-containing feedstock showed a short overshoot compared to the baseline viscosity, followed by a slight decrease starting with the baseline viscosity. Although both feedstocks, with and without alginate, showed a fast viscosity recovery period, the interactions between chitosan and alginate allowed an almost immediate recovery of the suspensions, which might be a critical factor in printability as discussed below.

6.3.3 Viscoelastic behavior

Oscillatory rheological tests are used to characterize viscoelastic materials by measuring the elastic (G') and the viscous (G'') modulus. First, oscillatory deformation amplitude (strain) sweeps were performed in both non-crosslinked (Figure 6.4 - a) and genipin-crosslinked (Figure 6.4b) gels with and without alginate. At low deformation amplitude, all samples showed solid-like behavior with G' higher than G''. This is already evident in the other gel-like properties discussed above, like high viscosity and a pronounced yield point. For samples without genipin or alginate, this solid-like behavior was observed up to 0.2% shear strain. Afterward, G'' is higher than G', which manifests in a fluid-like behavior. Adding alginate to the chitosan/alumina feedstock extended the solid-like behavior up to 4% shear strain. Apparently, the additional electrostatic interactions introduced with alginate enhance the polymer network flexibility from the feedstock without increasing the overall viscosity (compare Figure 6.3). Furthermore, both viscoelastic moduli of the feedstocks containing alginate are higher than without alginate over the whole deformation range confirming again the influence of alginate in the polymer network which was not visible in the rotational rheological tests.

Deformation amplitude tests with genipin were carried out after incubation with the gelling agent for 24 h at 37°C. Solid-like behavior was observed throughout the whole shear deformation range for genipin-crosslinked gels with and without alginate (Figure 6.4 - b). Furthermore, overall higher moduli were observed for gels containing alginate than without it. Additionally, genipin-crosslinked gels showed higher moduli overall shear strains than gels without genipin. Interestingly, with genipin two linear-viscoelastic (LVE) regions in the form of plateaus with parallel moduli from 0.01 to 0.07% (LVE 1) and from 5 to 45% (LVE 2) were observed (Figure 6.4), while only one initial plateau was observed without genipin.

This phenomenon is often related to shear-banding which might occur in complex fluids that support two different states of apparent viscosity for either the same shear rate or shear stress [26]. In this case, the occurrence of two LVE regions is most likely caused by the activation of the two different types of networks present in the material.

To further investigate this phenomenon, time tests with constant shear strains were performed within either of the LVE regions (0.05% for LVE 1 and 10% for LVE 2), in both genipin-crosslinked and non-crosslinked suspensions. Without genipin, time tests performed with and without alginate with 0.05% shear strain (Figure 6.4 - c) showed gel-like behavior over the whole duration of the measurement with a slight increase of G' and G'' over time. As before, the addition of alginate generally increases the moduli. Conversely, with a shear strain of 10% both gels show liquid-like behavior with G'' higher than G' and a decrease in both moduli observed (Figure 4 - e).

With genipin, the time tests were performed directly with the addition of the crosslinking agent (no 24 h waiting time as in the strain tests) to allow the observation of the gelation point. At 0.05% shear strain (Figure 6.4 - d), no gel-point could be observed and the gels behave almost exactly like the gels without genipin-crosslinking (Figure 6.4 - c). At 10% shear strain (Figure 6.4 - f), a liquid-like behavior is initially observed for both feedstock compositions due to deformation beyond the first LVE. However, after approx. 60 min, a sol-gel crossover point is observed for samples without alginate after which the sample regains gel-like behavior. Thereafter, the moduli continue to increase slightly during the observed time frame due to continued crosslinking. For samples containing alginate, a disruption of the curve is observed after around 80 min and after 100 min the sample regains a gel-like behavior. This reproducible disruption might be caused by slipping or the intermittent formation of shearing bands, originating from the high shear strain. Afterward, the network was reestablished due to further crosslinking and the moduli continuously increase reaching values similar to those without alginate. Accordingly, the presence of alginate seems to play a minor role after the sol-gel point, which is expected, since the network is now dominated by the covalent genipin crosslinking and the contributions from the electrostatic interactions between alginate and chitosan/alumina are broken up due to the high shear strain.

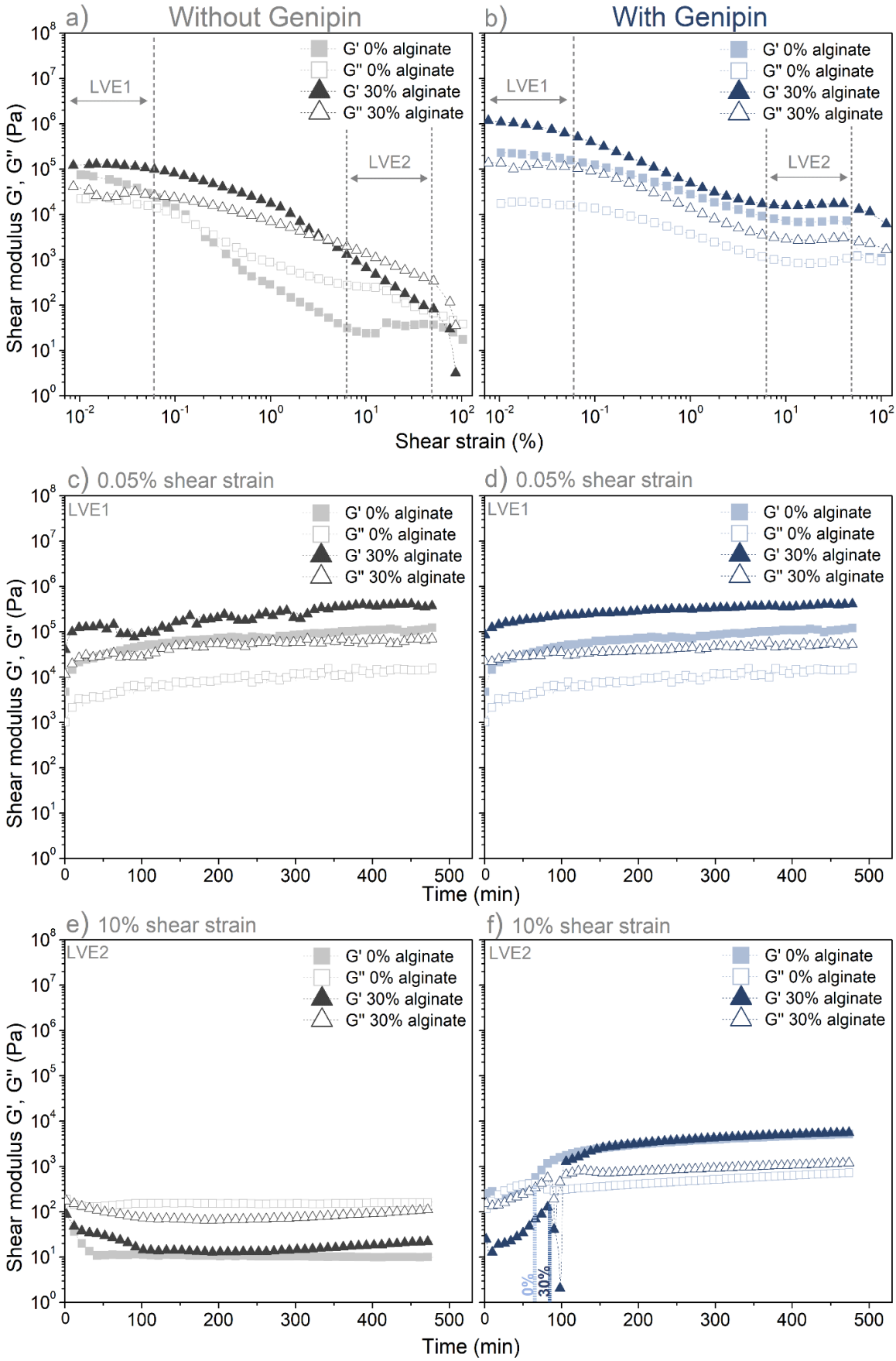

Figure 6.4 - Influence of genipin on the rheological properties of chitosan/alumina-based gels and analysis of the gelation point. The left column shows the graphs from feedstock

without genipin and the right column displays the effect of the addition of genipin. In the amplitude sweep of the crosslinked suspension (b) two LVE plateaus LVE 1 and LVE 2 were observed. Based on these two LVE regions, time tests were performed with the amplitude of LVE1 (c and e) and LVE2 (d and f) for suspension with and without genipin. All experiments were performed without (0% alginate) or with alginate (30% alginate).

Accordingly, these sets of rheological experiments unequivocally characterize both networking mechanisms: the fast and weak network formation in the particle-filled chitosan gel which is enhanced by electrostatic interactions between the negatively charged alginate and the positively charged chitosan and alumina which are apparent at LVE1 and the slower but stronger and more flexible covalent crosslinking between genipin and chitosan at LVE2. This also shows that only the chitosan/alginate/alumina gel determines the printability of the feedstock, while the genipin-crosslinking slowly reinforces the structures and ensures long-term stability.

6.3.4 Printability characterization

Next to the rheological behavior, several other parameters can influence shape fidelity and integrity of printed filaments, such as bioink homogeneity and crosslinking. Feedstock printability (Pr) was assessed by measuring the spacing between printed filaments of a grid structure. Ideal feedstocks for bioink (Pr = 1) should demonstrate a clear morphology with smooth surfaces and constant diameters of the extruded filament, which would result in regular grids and square holes in the fabricated constructs. If the feedstock shows overly solid-like behavior, an irregular spacing (Pr > 1) would be observed while a more liquid-like feedstock would result in a pronounced circular spacing (Pr < 1) due to filament merging [26].

Since genipin does not play a role in the immediate printability, chitosan gel-suspensions without covalent crosslinking with and without alginate were printed through a Ø 0.93 mm nozzle into a lattice cuboid (final size 2 x 2 x 1 cm) and the printability was analyzed after printing 3 and 8 layers (Figure 6.5). The printed chitosan/alumina constructs without alginate viewed horizontally from above or looking at a vertical cross-section showed a smooth surface of the printed filaments but no spacing could be observed after either 3 or 8 printed layers. Conversely, when the chitosan/alumina feedstock is printed with alginate, viewed horizontally, square shapes between the printed channels were observed after printing 3 and 8 layers, with Pr values of 1.07 ± 0.1 and 0.96 ± 0.04, respectively. Furthermore, although the layers merged to some degree, resulting in stacked filaments, the circular forms of the printed filaments with 796 ± 35 µm diameter could be observed

clearly in the vertical cross-sections. The differences between both feedstocks' printability correspond to their rheological behavior. As discussed above, the rheological behavior with and without alginate showed similar patterns of yield stress and shear rate behavior. However, the much faster recovery time and the overall higher viscoelastic moduli of alginate-containing feedstock contributed to a higher shape fidelity of the printed structures.

Comparing the results with the study by Heidenreich et al. [27], which analyzed rheological properties of collagen-chitosan bioinks without crosslinking, shows that our chitosan/alumina feedstock has a higher viscosity, and the viscoelastic behavior and printability of chitosan/alumina-containing alginate showed better results as well. Nevertheless, the printing tip used in Heidenreich et al. study was half the size of the one used in this study.

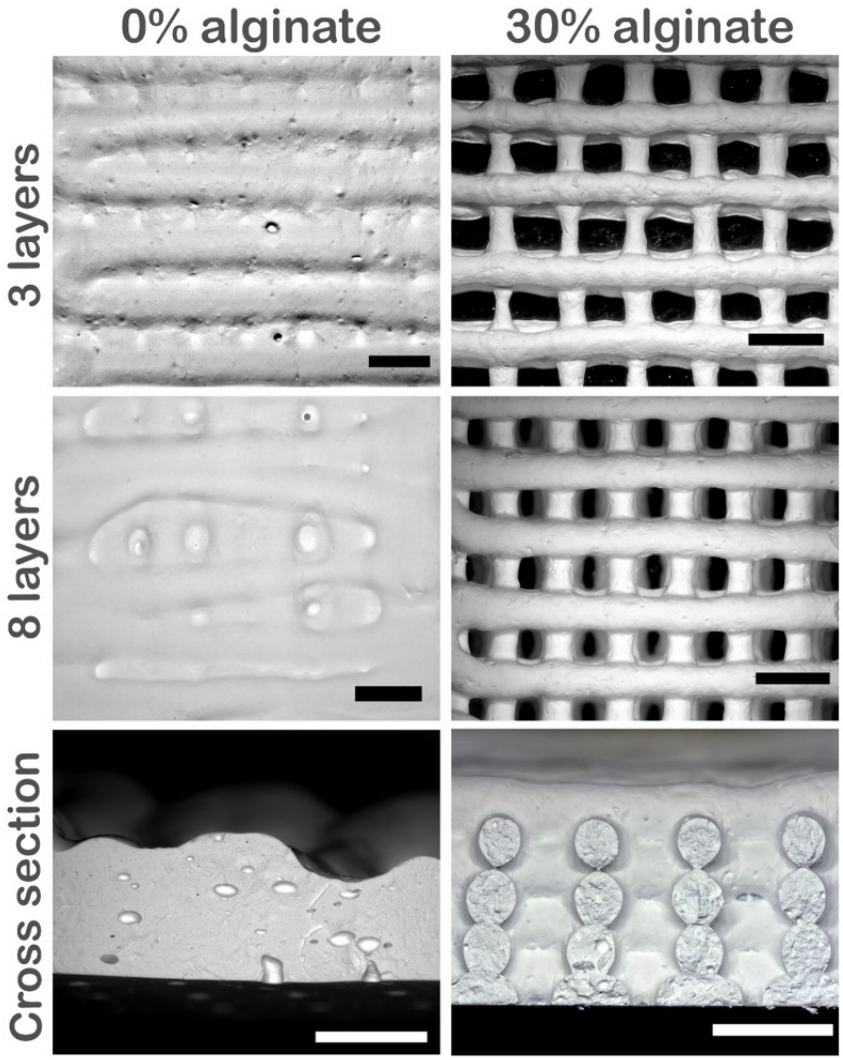

Figure 6.5 - 3D printed nanocomposite gels after 3 and 8 printed layers viewed horizontally from above as well as towards a vertical cross-section (8 layers) from samples without (0%) and with alginate (30%) (scale bar: 2 mm).

6.3.5 Material dissolution stability

To visualize the materials' behavior and their long-term dissolution stability in different media, chitosan/alumina nanocomposite gels with and without alginate and containing genipin were prepared and incubated for crosslinking for 24 h at 37°C. To visualize material behavior, the gel-cast (non-printed) samples were cut into rectangular pieces (3 x 1 x 0.3 cm) and deformed in different load directions (see Figure 6.6 which only shows samples with alginate). It was possible to reversibly deform the nanocomposite material in different directions showing the high elasticity of the material even with the high particle content. Furthermore, no differences were visually observed between samples with or without alginate.

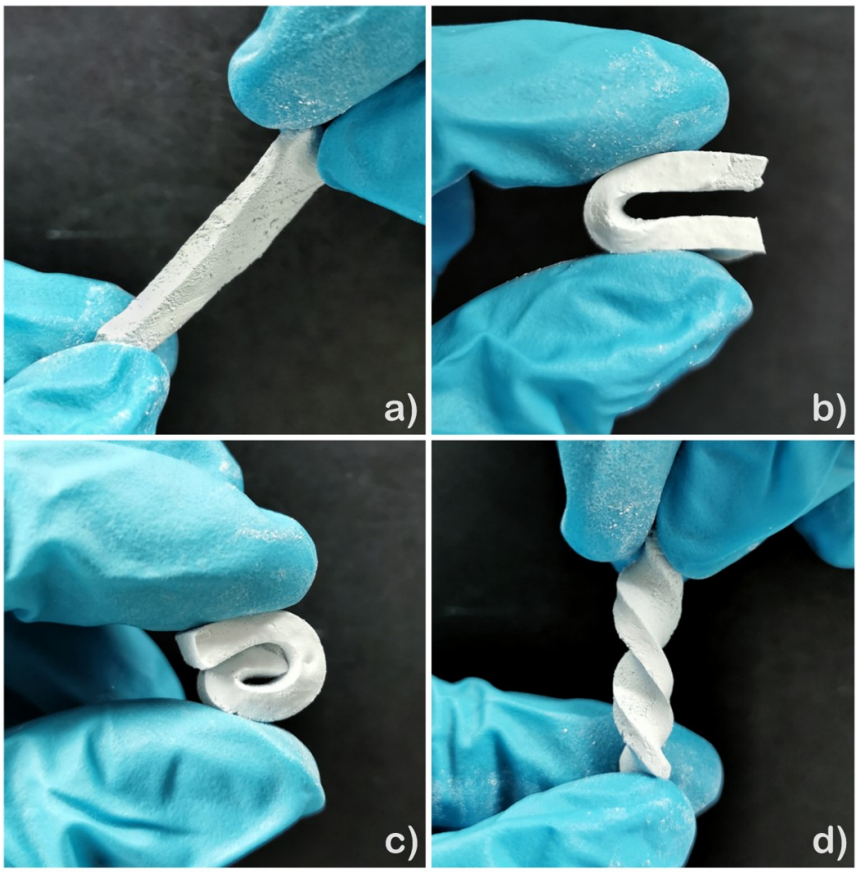

Figure 6.6 - Capacity of deformation of genipin-crosslinked chitosan/alginate/alumina nanocomposites.

Long-term stability of the non-crosslinked feedstocks and crosslinked materials against dissolution was assessed by submerging the samples in different media. For that, the crosslinked nanocomposite samples were removed from storage at 37°C and submerged in H2O, PBS, NaOH (1M), or HCl (1M) while non-crosslinked feedstocks were directly submerged in each solution and deviations in size or shape were visually analyzed after

60 days (Figure 6.7). After day 1, the samples were vigorously shaken for 15 s every four days and also just before imaging.

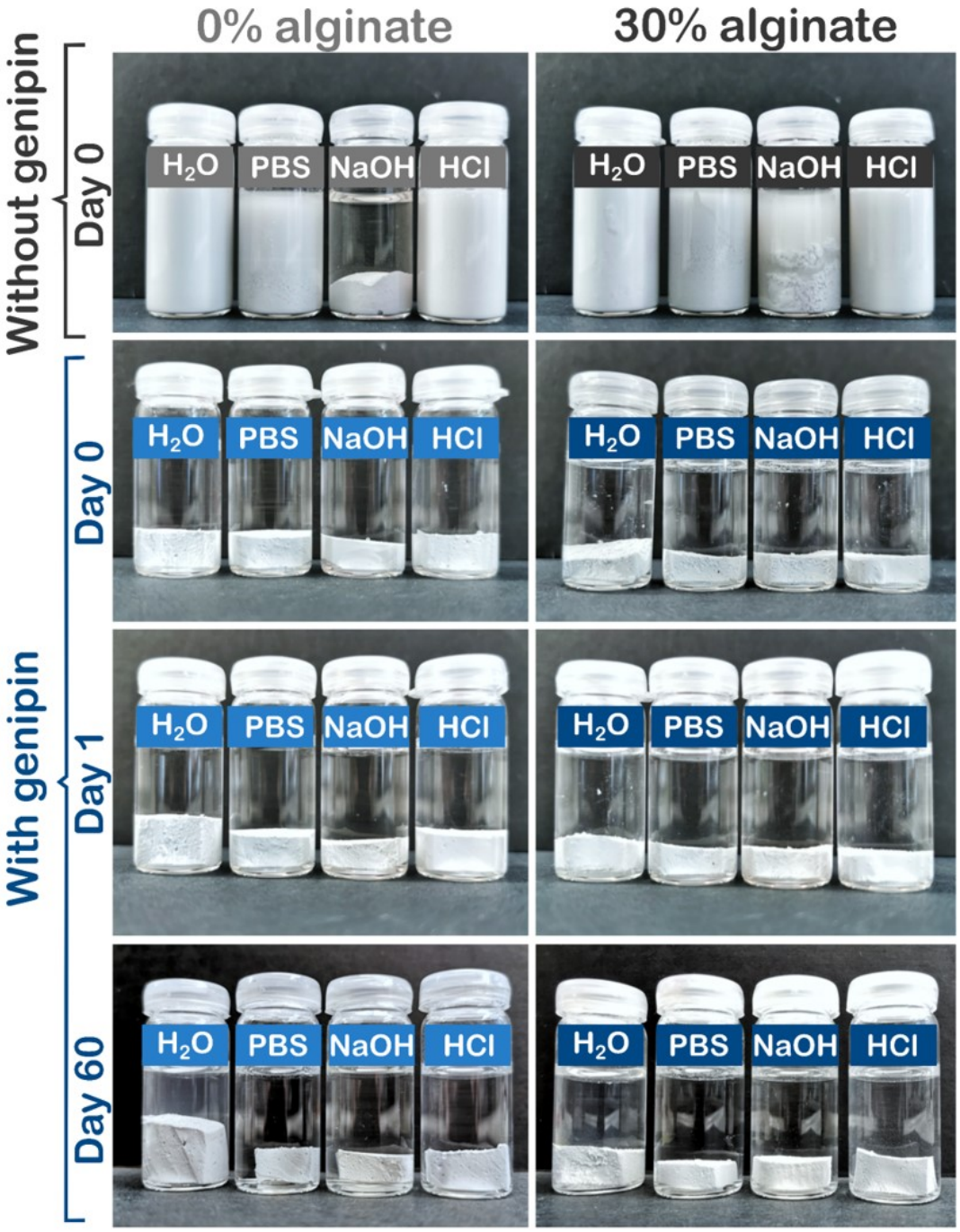

Figure 6.7 - Stability of (a) nanocomposite gels without genipin crosslinking after 24 h and (b, c) genipin-crosslinked chitosan composites without (0%) and with alginate (30%) in different media (water, PBS, 1M NaOH, and 1M HCl) after 24 h (b) and 60 days (c).

Dissolution of the polymer bonds can be qualitatively visually determined by observing a deviation in shape of the samples as well as an alteration in turbidity of the liquid medium.

Change in turbidity by sample dissolution is due to the release of alumina particles from the sample. Complete dissolution was observed after 24 h without genipin crosslinking when samples were submerged in water, PBS, and 1M HCl, while in 1M NaOH no dissolution was observed for samples without alginate and a partial dissolution for samples with 30% alginate was observed, suggesting insolubility of chitosan in basic pH. Moreover, neither dissolution, swelling nor shrinkage was observed for genipin-crosslinked gels with and without alginate when these samples were submerged in PBS, 1 M NaOH, or 1M HCl after 1 and 60 days. However, both crosslinked samples, with and without alginate, did swell in pure water after one day of incubation as a consequence of osmotic gradients, although to a lower degree for samples containing alginate. Most likely, the electrostatic crosslinking of the carboxylic groups of the alginate partially shields the cationic amine groups of the chitosan from contributing to the osmotically induced swelling of these hydrogels.

6.3.6 Bacterial viability

Lastly, the compatibility of embedded bacteria with the nanocomposite gels was exemplarily characterized for *E. coli* bacteria. Next to the chemical composition of the bioink material, the crosslinking method and the printing process could influence bacterial viability. Thus, to determine the influence of the genipin-crosslinked nanocomposite on bacterial viability, the viability of the immobilized bacteria was measured by cellular reduction of resazurin (blue color) into resorufin (pink and fluorescent color). A measurement of non-crosslinked nanocomposites was not performed due to complete dissolution of the material (Figure 6.7 - a). Genipin was incorporated into the chitosan/alumina gels with and without alginate with a final concentration of 0.20 and 0.26 mM of genipin, respectively, and the feedstock was either poured into a petri dish (gel-cast samples) or printed as described above. Additionally, some of the printed samples were submerged in LB medium instead of PBS during crosslinking. Bacteria viability was then quantified by the resazurin assay after 24 hours of genipin crosslinking (Figure 6.8 - a) and compared to the viability of the same quantity of freely suspended cells. It is important to note that the effective bacterial viability was obtained in these experiments which relate to the viability of the cells accessible by resazurin molecules and the corresponding resorufin metabolite which could release the sample.

Here, the non-printed samples showed almost no effective viability for both gels with and without alginate. Comparably, 3D-printed samples without alginate in PBS or with the addition of nutrients (LB medium) also showed no effective viability. Conversely, alginate-containing gels crosslinked in PBS showed approx. 30% effective viability while samples

crosslinked in 6.6% LB solution showed approx. 135% effective viability. The low viability of the bacteria in chitosan/alumina composites without alginate could be a result of the antimicrobial properties of chitosan or genipin [13] in combination with the poor accessibility of the bacteria inside the nanocomposite structure. Consequently, the influence of different genipin concentrations on bacterial viability after 5 and 24 h of incubation (Figure 6.8 - b) was analyzed. Here, genipin shows a low influence on bacterial viability after 5 h of incubation but a more pronounced influence can be observed after 24 h. Due to the lack of nutrients, bacterial viability is reduced to 50% after 24 h incubation in pure PBS but genipin-containing suspensions showed a more noticeable reduction of bacterial viability to 25% for 0.25 mM samples, and to 7% for 1 mM samples. Furthermore, a slight change of color from colorless to light blue could be observed when the genipin concentration was further increased. The blue color is a characteristic of the reaction of genipin with amino groups [13] and a color change of the bacterial solution might indicate that genipin reacted with amino acids of the cell membrane. This shows that genipin in the nanocomposite gels is moderately harmful to bacterial viability which is further substantiated by the absence of an effect of the LB medium which would only enhance proliferation and viability of living and accessible bacteria. Fessel et al. [20] prepared a collagen with tendon cells and incubated the material for 24, 72, and 144 hours with supplemented medium and different genipin concentrations up to 20 mM to measure the toxicity of the crosslinker. They also report a strong change of color to dark blue with increasing genipin concentration. Furthermore, genipin concentrations higher than 2.5 mM resulted in partial cell death, in which the effect increases with concentration and incubation time. Thus, by tailoring genipin concentration and incubation time the level of toxicity can be controlled.

Likewise, the addition of alginate to gel-cast samples had no effect on the bacterial viability and no viability could be observed. In contrast, for 3D printed samples crosslinked in PBS, 30% bacterial viability could be registered. This difference between printed and non-printed samples is most likely a result of the higher accessible surface area and especially the lower volume to be penetrated by the assay molecules in the printed structure. Furthermore, adding LB medium to the 3D printed samples during crosslinking further increased bacterial viability from 30% to 135%. This increase in viability over 100% indicates that the entrapped *E. coli* were protected by the alginate from genipin, and cells were able to proliferate inside the structure. Note that any free bacteria that proliferated outside of the structures were removed before testing by washing with PBS. Additional tests were performed with the WST-1 assay for validation and similar results were

obtained (Figure 6.8). These results show that tailoring material composition can also mitigate the toxicity of genipin and chitosan on bacteria.

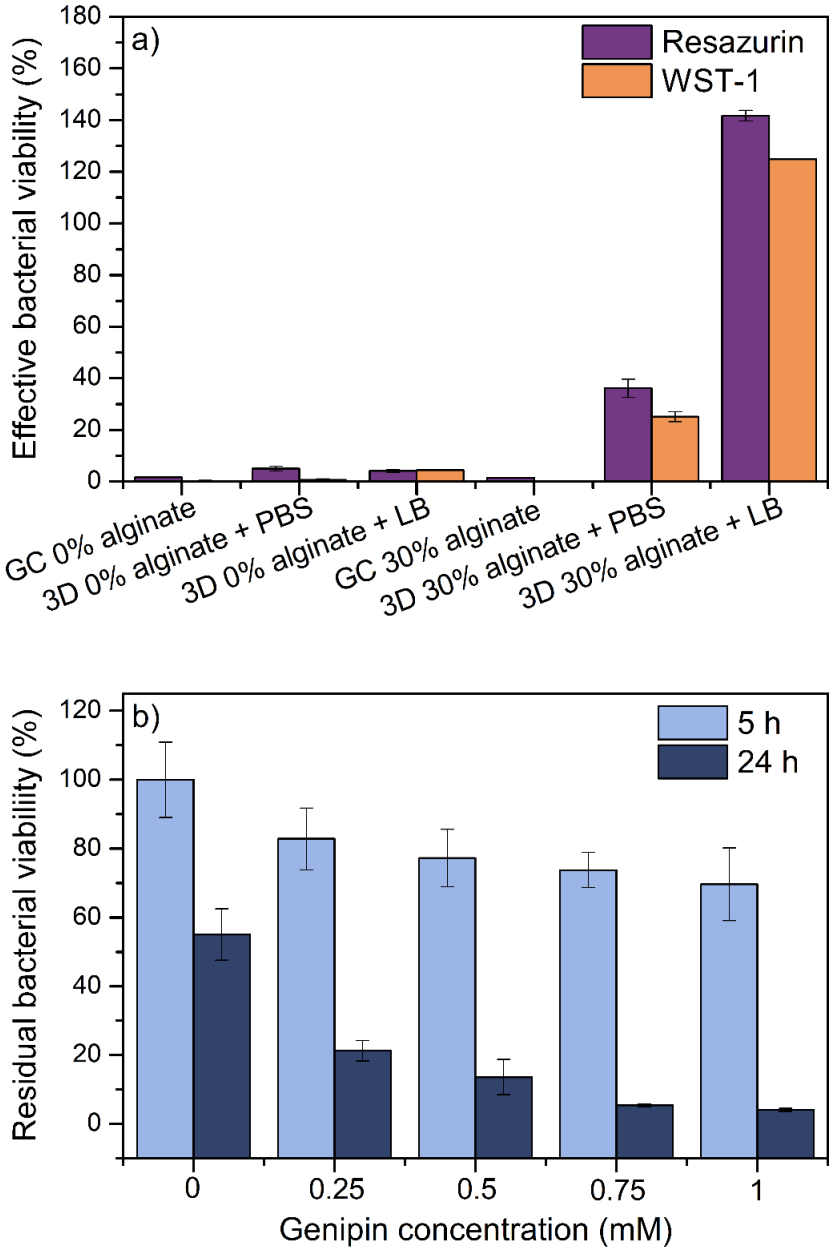

Figure 6.8 - Bacterial viability of embedded *E. coli* in genipin-crosslinked chitosan/alumina composites without (0%) and with alginate (30%) after 4 h (resazurin assay) and 1 h (WST-1 assay) incubation at 37°C (a). Bacterial viability was measured after two different processing routes: gel casting (GC) and 3D printing (3D), where 3D printed samples were either submerged in PBS or in LB medium during crosslinking to avoid drying. (b) Effect of different concentrations of genipin on the viability of freely suspended bacteria.

6.4 Conclusions

In conclusion, a new feedstock suitable for 3D bioprinting with embedded bacteria was developed. The feedstock is based on a highly filled chitosan/alginate/alumina nanocomposite with optimized rheological properties regarding shear thinning, high yield stress and fast recovery time. Electrostatic crosslinking of chitosan/alumina and alginate considerably increased shape fidelity after printing, allowing to further reinforce the material by covalent crosslinking between chitosan and genipin. Genipin-crosslinked gels showed two LVE regions which could be related to the different types of networks present in the nanocomposite gels. The first plateau corresponds to the alginate-reinforced chitosan/alumina network while the second plateau activates the covalently crosslinked chitosan connected by genipin. Genipin-crosslinked chitosan composites could withstand high deformation and showed excellent stability in PBS, NaOH and HCl solutions. Even though in water genipin-crosslinked composites without alginate showed swelling, this effect could be minimized with alginate-crosslinked chitosan. Additionally, the effective viability of *E. coli* embedded inside the nanocomposite materials was analyzed. Here, no bacterial viability of the samples without alginate in either printed or non-printed state was observed, which might be related to the moderate antibacterial activity of genipin, the reported antibacterial activity of chitosan and the poor accessibility of the bacteria inside the structures. However, 3D-printed alginate-containing composites showed 30% effective viability while non-printed materials showed again no viability. Accordingly, the printed sample geometry resulted in better accessibility of the embedded bacteria which allowed a higher turnover rate of the assay molecules. Furthermore, alginate seems to protect the bacteria from the antibacterial activity of genipin and chitosan. Once bacteria were alive and accessible, the effective viability could be further improved from 30% to 135% by incubating the printed samples with LB medium. These results demonstrate that we were able to create a feedstock material for 3D printing with long-term stability against dissolution and in which viable bacteria could be embedded.

6.5 References

1. Condi Mainardi, J., Rezwan, K. & Maas, M. *Genipin-crosslinked chitosan/alginate/alumina nanocomposite gels for 3D bioprinting*. Bioprocess Biosyst Eng 45, 171–185 (2022).

2. Matai I, Kaur G, Seyedsalehi A, McClinton A, Laurencin CT. *Progress in 3D bioprinting technology for tissue/organ regenerative engineering*. Biomaterials. 2020;226:119536.

3. Chimene D, Kaunas R, Gaharwar AK. Hydrogel Bioink Reinforcement for Additive Manufacturing: *A Focused Review of Emerging Strategies*. Advanced Materials. 2020;32(1):1902026.

4. Meka VS, Sing MKG, Pichika MR, Nali SR, Kolapalli VRM, Kesharwani P. *A comprehensive review on polyelectrolyte complexes*. Drug Discovery Today. 2017;22(11):1697-706.

5. Lawrie G, Keen I, Drew B, Chandler-Temple A, Rintoul L, Fredericks P, et al. *Interactions between Alginate and Chitosan Biopolymers Characterized Using FTIR and XPS*. Biomacromolecules. 2007;8(8):2533-41.

6. Sæther HV, Holme HK, Maurstad G, Smidsrød O, Stokke BT. *Polyelectrolyte complex formation using alginate and chitosan*. Carbohydrate Polymers. 2008;74(4):813-21.

7. Xu Y, Zhan C, Fan L, Wang L, Zheng H. *Preparation of dual crosslinked alginate–chitosan blend gel beads and in vitro controlled release in oral site-specific drug delivery system*. International Journal of Pharmaceutics. 2007;336(2):329-37.

8. Baysal K, Aroguz AZ, Adiguzel Z, Baysal BM. *Chitosan/alginate crosslinked hydrogels: Preparation, characterization and application for cell growth purposes*. International Journal of Biological Macromolecules. 2013;59:342-8.

9. Wang G, Wang X, Huang L. *Feasibility of chitosan-alginate (Chi-Alg) hydrogel used as scaffold for neural tissue engineering: a pilot study in vitro*. Biotechnology & Biotechnological Equipment. 2017;31(4):766-73.

10. Banerjee A, Ganguly S. *Alginate–chitosan composite hydrogel film with macrovoids in the inner layer for biomedical applications*. Journal of Applied Polymer Science. 2019;136(22):47599.

11. Hussain A, Kangwa M, Yumnam N, Fernandez-Lahore M. *Operational parameters and their influence on particle-side mass transfer resistance in a packed bed bioreactor*. AMB Express. 2015;5(1):51.

12. Colosi C, Costantini M, Latini R, Ciccarelli S, Stampella A, Barbetta A, et al. *Rapid prototyping of chitosan-coated alginate scaffolds through the use of a 3D fiber deposition technique*. Journal of Materials Chemistry B. 2014;2(39):6779-91.

13. Liu B-S, Huang T-B. *Nanocomposites of Genipin-Crosslinked Chitosan/Silver Nanoparticles - Structural Reinforcement and Antimicrobial Properties*. Macromolecular Bioscience. 2008;8(10):932-41.

14. Kean T.J., Thanou M. *Utility of Chitosan for 3D Printing and Bioprinting*. In: Crini G., Lichtfouse E. (eds) Sustainable Agriculture Reviews 35. Sustainable Agriculture Reviews, 2019; 35; 271-292. Springer, Cham.

15. Croisier F, Jérôme C. *Chitosan-based biomaterials for tissue engineering*. European Polymer Journal. 2013;49(4):780-92.

16. Mallakpour S., Sirousa F. and Mustansar Hussain C. *Current achievements in 3D bioprinting technology of chitosan and its hybrids*. New J. Chem., 2021,45, 10565-10576.

17. Vukajlovic D, Parker J, Bretcanu O, Novakovic K. *Chitosan based polymer/bioglass composites for tissue engineering applications*. Materials Science and Engineering: C. 2019;96:955-67.

18. Gao L, Gan H, Meng Z, Gu R, Wu Z, Zhang L, et al*. Effects of genipin cross-linking of chitosan hydrogels on cellular adhesion and viability*. Colloids and Surfaces B: Biointerfaces. 2014;117:398-405.

19. Delmar K, Bianco-Peled H. *The dramatic effect of small pH changes on the properties of chitosan hydrogels crosslinked with genipin*. Carbohydrate Polymers. 2015;127:28-37.

20. Fessel G, Cadby J, Wunderli S, van Weeren R, Snedeker JG. *Dose- and time-dependent effects of genipin crosslinking on cell viability and tissue mechanics – Toward clinical application for tendon repair*. Acta Biomaterialia. 2014;10(5):1897-906.

21. Hafezi F, Shorter S, Tabriz AG, Hurt A, Elmes V, Boateng J, Douroumis D. *Bioprinting and Preliminary Testing of Highly Reproducible Novel Bioink for Potential Skin Regeneration*. Pharmaceutics. 2020; 12(6):550.

22. Ahmed J, Mulla M, Maniruzzaman M. *Rheological and Dielectric Behavior of 3D-Printable Chitosan/Graphene Oxide Hydrogels*. ACS Biomaterials Science & Engineering. 2020;6(1):88-99.

23. Hafezi F, Scoutaris N, Douroumis D, Boateng J. *3D printed chitosan dressing crosslinked with genipin for potential healing of chronic wounds*. International Journal of Pharmaceutics. 2019;560:406-15.

24. Pandey AR, Singh US, Momin M, Bhavsar C. *Chitosan: Application in tissue engineering and skin grafting*. Journal of Polymer Research. 2017;24(8):125.

25. Maturavongsadit P., Karthik Narayanan L., Chansoria P., Shirwaiker R., and Benhabbour S R. *Cell-Laden Nanocellulose/Chitosan-Based Bioinks for 3D Bioprinting and Enhanced Osteogenic Cell Differentiation*. ACS Applied Bio Materials 2021 4 (3), 2342-2353 DOI: 10.1021/acsabm.0c01108

26. Ouyang L, Yao R, Zhao Y, Sun W. *Effect of bioink properties on printability and cell viability for 3D bioplotting of embryonic stem cells*. Biofabrication. 2016;8(3):035020.

27. Heidenreich A. C., Pérez-Recalde M., Wusener A. G., Hermida E. B.. *Collagen and chitosan blends for 3D bioprinting: A rheological and printability approach*. Polymer testing 2020; 82 106297.

7 Conclusions

The main purpose of this thesis was to contribute to the process engineering field by developing new processing strategies for microorganism immobilization into rigid porous materials for bioprocessing applications using only biocompatible materials.

Initially, a formulation of a biocompatible feedstock for rigid bionanocomposite was developed. For this purpose, a suspension of alginate highly filled with alumina nanoparticles was produced to immobilize *Escherichia coli* and *Bacillus subtilis* into cylindrical-shaped samples. Crosslinking was based on electrostatic interactions of the negatively charged alginate and the positively charged alumina nanoparticles in combination with internal/external crosslinking resulting in increased compression strength. The chemicals used to prepare the suspension as well as the processing route and crosslinking lead to an effective and straightforward method for microorganism immobilization. Moreover, the suspension can be adapted according to the cell type to turn the medium more suitable for cell physiology and growth, as shown by the addition of LB growth medium, which resulted in five times increment in *E. coli* cell viability. In this regard, the alginate/alumina nanocomposite showed promising results of long-term performance by means of cyclic tests, as well as long-term stability with minimal reduction of cell performance after 60 days of storage. Still, accessibility of the cells was hindered due to the size of the sample while sample dissolution was a major issue that restricts its application.

The previous research on rigid materials enabled tailoring the materials' porosity by foaming and 3D printing in order to overcome restricted accessibility of the cells. For that purpose, the suspensions composition, as well as the processing route, were altered to increase sample porosity and so decrease diffusion pathways through the sample. The 3D printing method was used to print highly particle-filled alginate hydrogel feedstocks containing living cells and so increased sample porosity. To further increase porosity, the protein albumin was incorporated into an alginate/alumina suspension with the bacteria *E. coli*. The protein stabilized the bubbles created by air incorporation, creating stable foams with micrometer-sized pores. The increased porosity of the foam resulted in higher water content in the samples which could be assessed by measuring the averaged effective water diffusion coefficient of the samples. The higher water content in combination with the printed structures considerably increased cell effective viability while the albumin itself did not just stabilize the foam but also could be consumed by the cells and resulted in cell growth. The increase in cell viability over time also showed that the materials' properties

allowed cell growth inside the sample. This shows promising results of increased diffusion as well as the capability of cell growth inside the bionanocomposite structures.

To further enhance material stability and avoid sample dissolution during application, the feedstock was altered to enable covalent bonding of the hydrogel instead of the weaker Van Der Waals bonding of the ionotropic gelation. A chitosan-based solution was prepared and reinforced with alumina particles and alginate to form a percolated gel and tune the optimal rheological properties for 3D printing. The amine groups of the chitosan were covalently crosslinked by the plant-based genipin, stabilizing the material and avoiding its dissolution in PBS, acidic or basic solution even after 60 days. The addition of alginate did not just increase feedstock stability by electrostatic complexation of alginate/chitosan but also decreased the antibacterial properties of chitosan/genipin. Furthermore, alginate increased feedstock printability while swelling in water was decreased. Incubating printed alginate-containing samples during crosslinking in LB growth medium improved the effective viability from 30% to 135%. These results demonstrate the success of producing a feedstock material for 3D printing with long-term stability against dissolution and in which viable bacteria could be immobilized and grow. Such materials pave the way towards innovation in bioprocessing with customized carrier geometries tailored for various microorganisms in a wide range of bioreactor environments.

To summarize, this work focused primarily on the development of feedstocks and crosslinking strategies suitable for gel casting and 3D printing to assure material form and pore stability, non-dissolution in reaction medium, enhanced nutrient diffusion and biocompatibility. Materials with hierarchical structures were produced by 3D printing foams resulting in increased porosity which facilitated reaction and allowed cellular growth. Dissolution issues could be solved by covalently crosslinking the feedstock using the plant-based molecule genipin, which resulted in high cell viability and allowed cellular growth inside the material. In consequence, the results of this thesis helped to understand the influence of porosity and alumina particles as reinforcement of hydrogels on shear forces and viscosity, mechanical properties, water diffusion, and cell viability. This work significantly contributes to the field of biotechnology and process engineering of porous ceramic support materials with special emphasis on the application areas of bioprocessing.

8 Outlook

New scientific questions and theories have emerged during the design of rigid porous hydrogel-based feedstocks, which could further deepen the understanding of the relationship between support material properties and cell viability for bioprocessing applications. Three main categories of future work can be defined, which are explained in this chapter. First, further research on different foaming agents is suggested. Second, the combination of hierarchical porosity and covalent crosslinking the material to create a more stable bonding is recommended. Third, the use of 3D methodology to create different concepts of bioreactors is presented.

First, concerning the further investigation of foam formation and 3D printing, albumin is a widely used protein in our daily life to form egg foams. In Chapter 5 the stabilization of bubbles to form hydrogel/ceramic foams was successfully demonstrated while bacterial viability was maintained. These proteins could be consumed by the cells and induced bacterial growth. However, uncontrolled cell growth might result in pore clogging while the consumption of the protein by the cells can be detrimental to the mechanical properties of the material and can decrease its long-term utilization. To understand if cell feeding would consume the material, an experiment was described in Chapter 5 about the incubation of *E. coli* bacteria in different concentrations of either albumin or alginate solutions. Bacteria incubated with proteins resulted in 4-fold higher viability after 48 h, while no difference was observed with bacteria incubated in different concentrations of alginate solutions, which means bacteria would not consume the alginate structure but would consume the albumin. Different proteins could be used for foam stabilization, such as casein, but bacteria might consume these proteins as well and result in uncontrolled cell growth and a decrease in mechanical properties. Alternatively, nanoparticles can also be used for foam stabilization. The hydrogel is highly filled with ceramic nanoparticles and these particles could be surface modified to stabilize bubbles as well. Minas et al. [1] and Muth et. al. [2] printed alumina wet foams and stabilized the bubbles with partially hydrophobized alumina particles, obtained by surface modification with the surfactants valeric acid and butyric acid, respectively. Still, the presence of surfactant molecules and the low processing pH in these approaches are not ideal conditions for cell cultivation. Therefore, alternatives for particle surface modification would need to be researched to increase its biocompatibility and allow 3D printing as well.

Second, the combination of the hierarchical porosity formation using foaming agents and covalent crosslinking with genipin is also one important step for further investigation. It might seem like a straightforward approach, but the chitosan-based feedstock is very sensitive to any extra component with different electrostatic surface charging and alteration of pH. Preliminary tests combining the protein albumin into the chitosan solution were performed but the feedstock was not stable, and crosslinking was not efficient. Similar tests were performed using silica (negatively charged) instead of alumina (positively charged) and the feedstock slightly foamed but no crosslinking took place. Thus, a closer look into the interactions between the polymer chains, particles, genipin crosslinking, pH and bubble stabilization is necessary.

Third, 3D printing is a suitable method for customization, especially into shapes that were difficult to produce by simpler processing methods such as gel casting. The possibility to print materials containing immobilized cells for bioprocessing into a desired shape could be the next innovation step to change bioreactor concepts. In the chemical reactor field, Soleto and Gil [3] produced in 2016 a robust, efficient, and reusable alumina/copper catalyst to promote Ullman reactions (Figure 7.1 - a). The resulting catalyst showed high catalytic efficacy and good recyclability and did not produce leaching of copper to the reaction medium after different Ullmann reactions. In the bioreactor field, Edgar Peris et al. [4] printed a nylon reactor by filament deposition modeling (FDM) and immobilized enzyme on its surface using glutaraldehyde (Figure 7.1 - b). A total of 105 catalytic cycles were performed with the immobilized ω-transaminase enzyme and it showed comparable activity to free enzymes with the advantage of recyclability of the enzymes. Moreover, Schmieg et al. [5] printed hydrogel-based enzyme reactors (Figure 7.1 - c). Three different enzymes were tested: alcohol dehydrogenase, benzoylformate decarboxylase or β-galactosidase and in all cases enzyme activity was measured lower than freely suspended enzymes due to mass transfer limitations.

Fluid flow dynamics must be carefully analyzed and optimized for chemical and biochemical reactions. The shape of the reactor has a high influence on the fluid flow dynamics and therefore the reaction. Even though chemical reactors and bioreactors are established processes in the industry, continuous research and optimization to increase production rate and efficiency of the reactors are still necessary. Nieves-Remacha et al. [6] used computational fluid dynamics (CFD) to analyze and optimize fluid flow in a different shapes of continuous flow reactors (Figure 7.1 - d). The flow regime can be controlled by different variables such as the shape of the channel, surface properties of the internal walls, the mixer structure, and conditions (flow velocities, temperature, etc.)

and this reactor geometry allowed higher recirculation zones, which benefits must be analyzed for each individual reaction. Thus, the architecture of 3D-printed reactors can be tailored to specific applications using different printing approaches to create an optimal environment for bioreactions. Tank bioreactors with microorganisms necessitate optimal stirring velocity, nutrient flow, pH and oxygenation. These reactors consist of a reservoir with the microorganism-containing solution and a stirrer located in the middle (Figure 7.2), in which stirring velocity and stirrer geometry influence the fluid flow in the reactor.

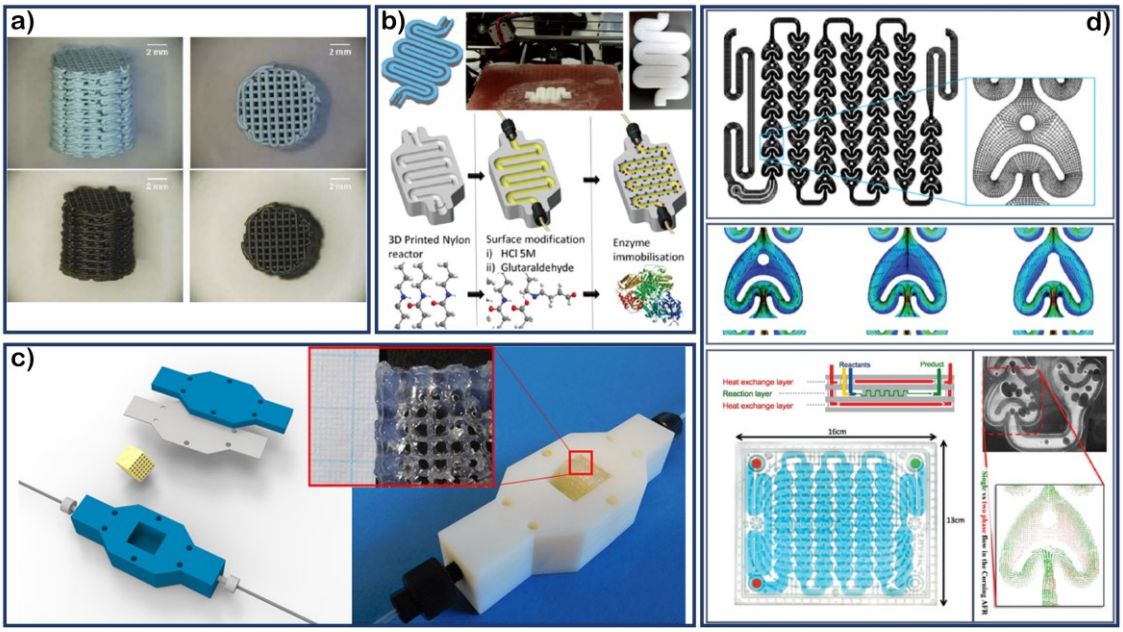

Figure 7.1 – Overview of different reactors produced by 3D printing: a) alumina/copper catalyst to promote Ullman reactions from Soleto and Gil [3], b) 3D printed a nylon reactor with immobilized ω-Transaminase enzyme from Edgar Peris et al. [4], c) 3D printed hydrogel-base feedstock containing entrapped enzyme from Schmieg et al. [5], and d) the new flow reactor geometry model used for computational fluid dynamics from Nieves-Remacha et al. [6]. Images with permission from Elsevier, Royal Society of Chemistry, Frontier, and American Chemical Society, respectively.

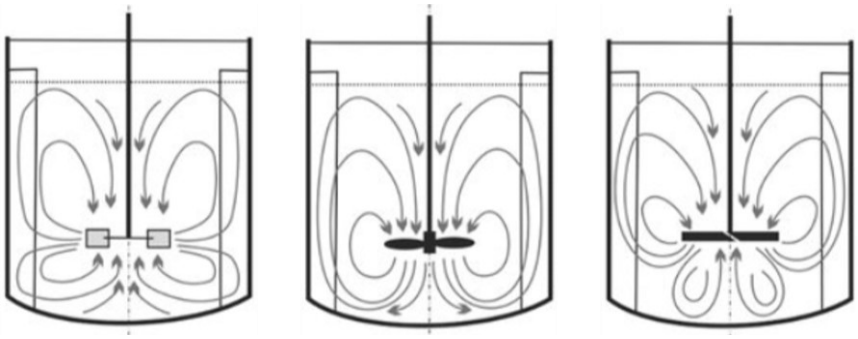

Figure 7.2 – Illustration of a tank reactor and the influence of the stirrer geometry on fluid flow dynamics in the reactor. Adapted from [7] with permission from MDPI.

One alternative would be to combine the stirrer with the embedded cells by means of 3D bioprinting. Figure 7.3 illustrates a 3D bioprinted stirrer that contains the cells in its filaments and is connected to the reactor axle. The total porosity, pore size, pore orientation, and stirring velocity could be adjusted to assure the optimal diffusion of nutrients and oxygenation for each specific microorganism and its reaction time. Furthermore, the cell density could be higher in the printed structure which could allow smaller reactor size. Alternatively, magnetic particles could be integrated into the printed stirrer and stirrer velocity could be controlled by a magnetic field. New reactor concepts can remarkedly enhance the functionality and efficiency of reactors and support the process engineering field.

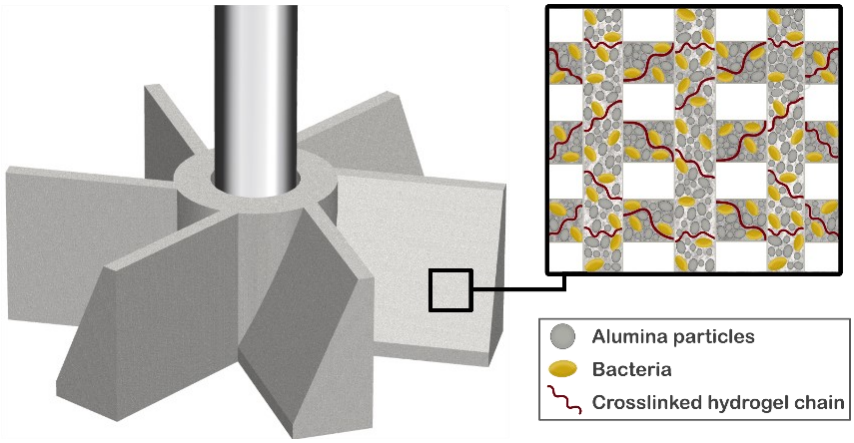

Figure 7.3 – Schema of a different bioreactor concept using a 3D printed stirrer with embedded microorganisms for bioreactions.

References:

1. Minas, C., et al., *3D Printing of Emulsions and Foams into Hierarchical Porous Ceramics.* Advanced Materials, 2016. 28(45): p. 9993-9999.
2. Muth, J.T., et al., *Architected cellular ceramics with tailored stiffness via direct foam writing.* Proceedings of the National Academy of Sciences, 2017. 114(8): p. 1832.
3. Tubío, C.R., et al., *3D printing of a heterogeneous copper-based catalyst.* Journal of Catalysis, 2016. 334: p. 110-115.
4. Peris, E., et al., *Tuneable 3D printed bioreactors for transaminations under continuous-flow.* Green Chemistry, 2017. 19(22): p. 5345-5349.
5. Schmieg, B., et al., *Advantages of Hydrogel-Based 3D-Printed Enzyme Reactors and Their Limitations for Biocatalysis.* Frontiers in Bioengineering and Biotechnology, 2019. 6.

6. Nieves-Remacha, M.J., A.A. Kulkarni, and K.F. Jensen, *OpenFOAM Computational Fluid Dynamic Simulations of Single-Phase Flows in an Advanced-Flow Reactor.* Industrial & Engineering Chemistry Research, 2015. 54(30): p. 7543-7553.
7. Jaszczur, M. and A. Młynarczykowska, *A General Review of the Current Development of Mechanically Agitated Vessels.* Processes, 2020. 8(8): p. 982.

Curriculum Vitae

Name	Jéssica Condi Mainardi
Nationality	Brazilian

Education

10.2016 - 2022	PhD student Advanced ceramics group, Universität Bremen - Bremen, Germany Topic: Porous ceramic nanocomposite with embedded biofunctionality
05.2010 - 09.2016	Diploma in materials engineering Universidade Federal de Santa Catarina (UFSC) - Florianópolis, Brazil
08.2013 - 08.2014	Exchange student in materials engineering Rheinisch-Westfälische Technische Hochschule Aachen (RWTH) Scholarship from Coordenação de Aperfeiçoamento de Pessoal de Nível Superior - CAPES, Brazil

Professional/Research experience

01.03.2021 - today	Scientist Procter and Gamble (P&G) – Kronberg, Germany Topic: material development and analysis of shavers, epilators, and oral-care products.
10.2016 - 03.2020	Member of research training group Micro-, meso- and macroporous nonmetallic Materials: Fundamentals and Applications (MIMENIMA), Universität Bremen - Bremen, Germany.
10.2015 - 05.2016	Diploma thesis Advanced ceramics group, Universität Bremen - Bremen, Germany Topic: Thermal degradation of oxide fibers during minicomposite processing
05.2015 - 08.2015	Internship Laboratory of materials (LabMat - UFSC) - Florianópolis, Brazil Topic: Analysis of the corrosion behavior of plasma-enriched metal samples
09.2014 - 02.2015	Internship MAN Diesel & Turbo - Augsburg, Germany Topic: material investigation of the turbocharger housing

02.2012 - 07.2013	Research student Laboratory for Design and Manufacturing of Injected Plastic Components (Cimject - UFSC) - Florianópolis, Brazil Topic: project of bioabsorbable polymer pieces and mold, like anchor and stent.
02.2012 - 07.2013	Research student Group of studies in Lean (Glean - UFSC) - Florianópolis, Brazil Topic: study about lean manufacturing, theory and practice. Theory in 5S, TPM, Kaizen, A3, Value stream mapping (VSM). Practice: 1 - Lean Consulting at Mormaii (in Florianópolis – Brazil) with the implementation of Value Stream Mapping (VSM), current and future state, of the area of customer service. 2 - Internship (one moth) at WEG S.A. (in Jaraguá do Sul – Brazil) with the Kaizen implementation in the automaker of electronic circuits.
05.2012 - 09.2012	Internship Bosch Rexroth - Pomerode, Brazil Topic: Quality control of heat treated and thermochemically treated pieces and failure analysis of damaged pieces.
09.2011 - 12.2011	Internship Electro Aço Altona S.A - Blumenau, Brazil Topic: improvement of mold parameters to enhance cast steel quality.

Training

10.2017 - 08.2018	“navigare” – career coaching for women in science 7 days Workshop with Seminars and group coaching

Additional qualifications

Portuguese	Mother tongue
English	Fluent
German	Fluent
IT knowledge	OriginLab, Microsoft office, Solid Works, Inkscape,

List of Publications and Conference Contributions

List of Publications (peer-reviewed):

Condi Mainardi, J., Rezwan, K. & Maas, M. – *"Embedding live bacteria in porous hydrogel/ceramic nanocomposites for bioprocessing applications"*. Bioprocess Biosystem Engineering 42, 1215–1224 (2019). https://doi.org/10.1007/s00449-019-02119-4

Condi Mainardi, J., Catarina Bonini Demarchi, Mojtaba Mirdrikvand, Md Nurul Karim, Rezwan, K. & Maas, M. – "*3D bioprinting of hydrogel/ceramic composites with hierarchical porosity".* J Mater Sci 57, 3662–3677 (2022). https://doi.org/10.1007/s10853-021-06829-7

Condi Mainardi, J., Rezwan, K. & Maas, M. – *"Genipin-crosslinked chitosan/alginate/ alumina nanocomposite gels for 3D bioprinting".* Bioprocess Biosystem Engineering 45, 171–185 (2022). https://doi.org/10.1007/s00449-021-02650-3

Conference contributions:

J. Condi Mainardi, K. Rezwan, M Maas – *"Embedding live bacteria in hydrogel/ceramic nanocomposites by ionotropic gelation"*, Poster presentation, Biointerfaces 2018, Zürich - Switzerland

J. Condi Mainardi, K. Rezwan, M Maas – *"Embedding live bacteria in porous hydrogel/ceramic nanocomposites for bioprocessing applications"*, Oral presentation, European congress and exhibition on advanced materials and processes (EUROMAT) 2019, Stockholm – Sweden.

J. Condi Mainardi, K. Rezwan, M Maas – *"3D printing of microorganisms embedded in ceramic nanocomposites with future perspectives in space"*, Oral presentation, 2nd Sino-German Workshop on 3D printing in Space, 2019, Berlin - Germany

Author Contributions for the Publications presented in this Work

Condi Mainardi, J., Rezwan, K. & Maas, M. – *"Embedding live bacteria in porous hydrogel/ceramic nanocomposites for bioprocessing applications"*. Bioprocess Biosystem Engineering 42, 1215–1224 (2019). https://doi.org/10.1007/s00449-019-02119-4

Contents of this publication have been used in the Abstract and Chapters 1, 2, 3, 4 and 7.

Author	Contribution
Jessica Condi Mainardi	Experimental concept, planning and execution of experiments, data interpretation, manuscript preparation
Kurosch Rezwan	Conceptual advice, advice on data interpretation, manuscript editing
Michael Maas	Conceptual advice, advice on data interpretation, co-wrote the manuscript, manuscript editing

Condi Mainardi, J., Catarina Bonini Demarchi, Mojtaba Mirdrikvand, Md Nurul Karim, Rezwan, K. & Maas, M. – "*3D bioprinting of hydrogel/ceramic composites with hierarchical porosity".* J Mater Sci 57, 3662–3677 (2022). https://doi.org/10.1007/s10853-021-06829-7

Contents of this publication have been used in the Abstract and Chapters 1, 2, 3, 5 and 7.

Author	Contribution
Jessica Condi Mainardi	Experimental concept, planning and execution of experiments, data interpretation, manuscript preparation
Catarina Bonini Demarchi	Execution of experiments
Mojtaba Mirdrikvand	Execution and data interpretation of NMR experiments
Md Nurul Karim	Execution and data interpretation of porosity measurements by CT scans
Kurosch Rezwan	Conceptual advice, advice on data interpretation, manuscript editing
Michael Maas	Conceptual advice, advice on data interpretation, co-wrote the manuscript, manuscript editing

Condi Mainardi, J., Rezwan, K. & Maas, M. – *"Genipin-crosslinked chitosan/alginate/ alumina nanocomposite gels for 3D bioprinting".* Bioprocess Biosystem Engineering 45, 171–185 (2022). https://doi.org/10.1007/s00449-021-02650-3

Contents of this publication have been used in the Abstract and Chapters 1, 2, 3, 6 and 7.

Author	Contribution
Jessica Condi Mainardi	Experimental concept, planning and execution of experiments, data interpretation, manuscript preparation
Kurosch Rezwan	Conceptual advice, advice on data interpretation, manuscript editing
Michael Maas	Conceptual advice, advice on data interpretation, co-wrote the manuscript, manuscript editing

List of Student Projects

This work could not have been accomplished without the help of several motivated and hard-working students. Therefore, the following students are gratefully acknowledged and in the dissertation the results from the supervision of the following students' works are included:

Demarchi, C. B.	"3D bioprinting of porous gel-ceramic composites with embedded bacteria using the protein ovalbumin as a foaming agent" Diploma thesis, 2020
Reineke, L. Riemann, J. Weißhorn, L.	"3D Druck von keramischen Biotinten - Mit dem Schwerpunkt auf Prozesstechnik" *Masterprojekt*, 2019
Kamtchueng, A. B. Vielhauer, D.	"3D Druck von keramischen Biotinten - Mit dem Schwerpunkt auf *der Untersuchung der immobilisierten Mikroorganismen nach der Prozessierung"* *Masterprojekt*, 2019
Travers, P. K.	"A biocompatible freeze casting route of alginate based bionanocomposites" Diploma thesis, 2018